AD A086970

LEVEL II
SC

Edward L. Ginzton Laboratory

OF THE

W. W. HANSEN LABORATORIES OF PHYSICS

STANFORD UNIVERSITY · STANFORD, CALIFORNIA 94305

DDC
REPRODUCED
FEB 20 1980
RECEIVED

This document has been approved for public release and sale; its distribution is unlimited.

UNCLASSIFIED

SECURITY CLASSIFICATION OF THIS PAGE (When Data Entered)

REPORT DOCUMENTATION PAGE

READ INSTRUCTIONS BEFORE COMPLETING FORM

1. REPORT NUMBER

2. GOVT ACCESSION NO.

3. RECIPIENT'S CATALOG NUMBER

(9) Doctoral Thesis

4. TITLE (and Subtitle)

(6) TRANSDUCER ARRAYS SUITABLE FOR ACOUSTIC IMAGING

5. TYPE OF REPORT & PERIOD COVERED

Interim Memorandum

6. PERFORMING ORG. REPORT NUMBER

G.L. Report No. 2833

7. AUTHOR(s)

(10) Charles S. DeSilets

8. CONTRACT OR GRANT NUMBER(s)

(15) N00014-75-C-0632
RISC-RI74-20773

9. PERFORMING ORGANIZATION NAME AND ADDRESS

Edward L. Ginzton Laboratory
W.W. Hansen Laboratories of Physics
Stanford University, Stanford, CA 94305

10. PROGRAM ELEMENT, PROJECT, TASK AREA & WORK UNIT NUMBERS

11. CONTROLLING OFFICE NAME AND ADDRESS

Office of Naval Research
800 N. Quincy Street
Arlington, VA 22217

12. REPORT DATE

(11) Jun[illegible]78

13. NUMBER OF PAGES

187

14. MONITORING AGENCY NAME & ADDRESS (if different from Controlling Office)

(14) GL-2833 (12) 191

15. SECURITY CLASS. (of this report)

15a. DECLASSIFICATION/DOWNGRADING SCHEDULE

16. DISTRIBUTION STATEMENT (of this Report)

Approved for public release; distribution unlimited

17. DISTRIBUTION STATEMENT (of the abstract entered in Block 20, if different from Report)

18. SUPPLEMENTARY NOTES

19. KEY WORDS (Continue on reverse side if necessary and identify by block number)

Transducer Arrays
Acoustic Imaging
Linear Arrays
Transduction Efficiency
Angular Beamwidths
Quarter-Wave Matching Layers
Fourier Transform
Low Acoustic Impedance Material

20. ABSTRACT (Continue on reverse side if necessary and identify by block number)

The design and development of piezoelectric transducer arrays suitable for use in electronically scanned and focused acoustic imaging systems is described. These arrays are desitned to operate in the frequency range 2-5 MHz within 45 to 80% fractional bandwidths. Linear arrays of up to 180 elements have been built and used extensively in acoustic imaging systems. Particular attention is placed on achieving high transduction efficiency and angular beamwidths of at least ± 15°.

(continued)

DD FORM 1 JAN 73 1473 EDITION OF 1 NOV 65 IS OBSOLETE
S/N 0102-LF-014-6601

UNCLASSIFIED 409640 slt

SECURITY CLASSIFICATION OF THIS PAGE (When Data Entered)

Design techniques based on the the transmission line model of the transducer of Krimholtz, Leedom, and Matthaei are formulated for achieving efficient, broadband operation. These techniques involve the use of quarter-wave matching layers between a high impedance ceramic and a low impedance load. Broadband matching criteria are generated, and a novel technique for selecting the quarter-wave matching layer impedances is described. The theoretical transient response of the transducer is obtained by taking the Fourier transform of the transfer function of the transducer. An experimental transducer built using the formulated design techniques is described and its characteristics compared to theory.

Slotted transducer arrays employing tall, narrow elements are described. A one-dimensional model of this kind of element is formulated, and the effects of coupling between element resonant modes are examined. A variational theory for the effective radiation impedance of a narrow element is formulated and the effect of this impedance on the transducer characteristics is described. Experimental results with simple, highly backed arrays of 100 to 120 elements as well as an 180 element double quarter-wave matched array are compared with the theoretical predictions. A brief description of the effects of array cross-coupling on the element spatial frequency response is included.

The theory of unslotted, monolithic transducer arrays is presented along with experimental results with simple, highly backed monolithic arrays. Problems with achieving a uniform spatial frequency response for an array of high acoustic impedance elements radiating into a low impedance load are detailed. An application of this type of array using low acoustic impedance material, PVF_2, is shown. The broad and uniform angular response of a ceramic monolithic array radiating into metal is demonstrated.

(2)

TRANSDUCER ARRAYS SUITABLE FOR ACOUSTIC IMAGING

by

Charles S. DeSilets

G.L. Report No. 2833

June 1978

DDC
FEB 20 1980
RECEIVED

Internal Memorandum

Contracts:

N00014-75-C-0632

and

RISC RI74-20773

Edward L. Ginzton Laboratory
W. W. Hansen Laboratories of Physics
Stanford University
Stanford, California

This document has been approved for public release and sale; its distribution is unlimited.

© Copyright 1978

by

Charles S. DeSilets

I certify that I have read this thesis and that in my opinion it is fully adequate, in scope and quality, as a dissertation for the degree of Doctor of Philosophy.

(Principal Adviser)

I certify that I have read this thesis and that in my opinion it is fully adequate, in scope and quality, as a dissertation for the degree of Doctor of Philosophy.

I certify that I have read this thesis and that in my opinion it is fully adequate, in scope and quality, as a dissertation for the degree of Doctor of Philosophy.

Approved for the University Committee on Graduate Studies

Dean of Graduate Studies

Accession For	
NTIS GRA&I	☑
DTIC TAB	☐
Unannounced	☐
Justification	
By	
Distribution/	
Availability Codes	
Dist	Avail and/or special
A	

ABSTRACT

The design and development of piezoelectric transducer arrays suitable for use in electronically scanned and focused acoustic imaging systems is described. These arrays are designed to operate in the frequency range 2 - 5 MHz within 45% to 80% fractional bandwidths. Linear arrays of up to 180 elements have been built and used extensively in acoustic imaging systems. Particular attention is placed on achieving high transduction efficiency and angular beamwidths of at least ±15°.

Design techniques based on the transmission line model of the transducer of Krimholtz, Leedom, and Matthaei are formulated for achieving efficient, broadband operation. These techniques involve the use of quarter-wave matching layers between a high impedance ceramic and a low impedance load. Broadband matching criteria are generated, and a novel technique for selecting the quarter-wave matching layer impedances is described. The theoretical transient response of the transducer is obtained by taking the Fourier transform of the transfer function of the transducer. An experimental transducer built using the formulated design techniques is described and its characteristics compared to theory.

Slotted transducer arrays employing tall, narrow elements are described. A one-dimensional model of this kind of element is formulated, and the effects of coupling between element resonant modes are examined. A variational theory for the effective radiation impedance

of a narrow element is formulated, and the effect of this impedance on the transducer characteristics is described. Experimental results with simple, highly backed arrays of 100 to 120 elements as well as an 180 element double quarter-wave [illegible] array are compared with the theoretical predictions. A brief d[illegible]ction of the effects of array cross-coupling on the element spatial frequency response is included.

The theory of unslotted, monolithic transducer arrays is presented along with experimental results with simple, highly backed monolithic arrays. Problems with achieving a uniform spatial frequency response for an array of high acoustic impedance elements radiating into a low impedance load are detailed. An application of this type of array using low acoustic impedance material, PVF_2, is shown. The broad and uniform angular response of a ceramic monolithic array radiating into metal is demonstrated.

ACKNOWLEDGEMENTS

Of the many people who have contributed to the successful completion of this dissertation, I want to acknowledge first of all, my wife Trudy. Her love, support, patience, and encouragement were instrumental in achieving this goal.

I especially thank Professor G. S. Kino, my research advisor, for his guidance, insight, and unbounded enthusiasm which contributed so much to the success of this project. I also must thank Dr. B. A. Auld for his helpful suggestions and interest in this work.

I owe a great debt of gratitude to my close friend and co-worker, Dr. J. D. Fraser, whose ideas and knowledge of practical science contributed so much to this work.

I am also grateful to Mr. T. Waugh, Dr. J. Havlice, and Professor P. Grant for their assistance with interfacing the transducer arrays to the imaging systems.

To the technical staff of the Ginzton Laboratory, I want to acknowledge their part in the fabrication of the transducers and transducer arrays. Mr. D. Walsh contributed much to the overall transducer array design and the many special fabrication techniques as well as doing much of the manufacturing itself. Messrs. G. Kotler and J. Vrhel did most of the preparation of the acoustic materials before assembly into the final transducer structures. Messrs. L. Goddard and F. Futtere deposited the electrode films. Mr. P. Galle built several test fixtures and molds. Messrs. P. Constantinidis and E. Johnson provided

much help in the machine shop. Mr. W. Hipkiss provided helpful suggestions concerning electrical components.

Special thanks must be given to Ms. I. Williams for her expert preparation of this document and to Mr. N. Bettini and his staff for the preparation of the figures.

Most of all, I want to express my gratitude to my parents for their unwavering faith in me and my aspirations. They probably have less understanding but more pride in this document than anyone.

TABLE OF CONTENTS

		Page
ABSTRACT		iv
ACKNOWLEDGEMENTS		vi
LIST OF FIGURES		x
I.	INTRODUCTION: GENERAL DESIGN CONSIDERATIONS	1
II.	DESIGN OF EFFICIENT, BROADBAND PIEZOELECTRIC TRANSDUCERS	11
	A. Introduction	11
	B. Transducer Model	15
	C. Broadband Matching Criteria	16
	D. Front Acoustic Load Line	22
	E. Effect of Backing	28
	F. Electrical Port	35
	G. Transient Response	39
	H. Experimental Results	42
III.	SLOTTED TRANSDUCER ARRAY DESIGN	48
	A. Introduction	48
	B. Model of a Narrow Slotted Element	51
	C. Coupling to Lateral Mode	60
	D. Effective Acoustic Load Impedance of a Narrow Element	68

TABLE OF CONTENTS (Cont'd)

		Page
III.	SLOTTED TRANSDUCER ARRAY DESIGN (continued)	
	E. Experimental Results with Simple Backed Arrays. . .	85
	F. Quarter-Wave Matched Arrays	98
	G. Cross-Coupling Between Array Elements	118
IV.	MONOLITHIC TRANSDUCER ARRAYS.	129
	A. Introduction.	129
	B. Theory of Angular Dependence of Monolithic Transducer.	132
	C. Experimental Results with Backed Monolithic Arrays.	135
	D. Elimination of Angular Response Beyond Longitudinal Critical Angle.	142
	E. PVF_2 Monolithic Arrays.	149
	F. Ceramic on Metal Monolithic Arrays.	151
APPENDIX A	. . . . .	156
APPENDIX B	. . . . .	158
APPENDIX C	. . . . .	162
REFERENCES	. . . . .	167

LIST OF FIGURES

Figure		Page
1-1	Schematic of an electronically scanned and focused acoustic imaging system using a linear transducer array.	4
1-2	Schematic of a transmission mode C-scan electronically focused imaging system	5
2-1	Transmission line model of a piezoelectric transducer.	14
2-2	Lumped element representation of the reactance of a transmission line.	18
2-3	Lumped element representation of the acoustic transmission line of a piezoelectric transducer	19
2-4	Power loss ratio of the front acoustic load line of a lead metaniobate transducer.	26
2-5	Comparison of the electrical impedance of two quarter-wave matched transducers	27
2-6	Effect of shorted back load line on acoustic impedance of a maximally flat front load line.	30
2-7	Equivalent electrical lumped circuit of transducer terminated by air and optimum load at the acoustic ports.	31
2-8	Effect of resistively loaded back load line on acoustic impedance of maximally flat front load line.	33

LIST OF FIGURES (Cont'd)

Figure		Page
2-9	Characteristics of a highly backed, water loaded PVF_2 transducer	36
2-10	Effects of increasing quarter-wave plate thickness 4% on single matched lead metaniobate transducer	38
2-11	Comparison of transient responses of linear filters with square and Gaussian bandshapes	41
2-12	Comparison of experimental results with theory of electrical impedance of single matched lead metaniobate transducer	44
2-13	Comparison of experimental and theoretical insertion loss of transducer in Fig. 2-12	45
2-14	Comparison of experimental and theoretical impulse response of transducer in Fig. 2-12	47
3-1	Schematic drawing of transducer array elements	49
3-2	Schematic drawing of tall, narrow array element	52
3-3	Generalized coupled mode dispersion curves for a small array element	62
3-4	Lower branches of coupled mode dispersion relation for isotropic rectangular resonators	64
3-5	Experimental and theoretical dispersion curves for slotted array elements	67
3-6	Real part of electrical impedance of lead-backed array elements with varying configuration ratio	69

LIST OF FIGURES (Cont'd)

Figure		Page
3-7	Schematic drawing of radiated wave from slotted array element.	71
3-8	Schematic drawing of waveguide model of transducer element used to calculate variational form of radiation impedance.	73
3-9	Normalized effective load impedance seen by a finite width radiator	81
3-10	Effective impedance of a water load seen by a finite width radiator	84
3-11	Comparison of effective load impedances of finite width radiator for Poisson's ratio of 0.4, 0.49, 0.50. .	86
3-12	Comparison of theoretical and experimental electrical impedance of lead-backed transducer elements	89
3-13	Comparison of theoretical and experimental impedance of tungsten-epoxy backed transducer elements.	94
3-14	Effect of calculated radiation impedance on the electrical impedance of a slotted array element.	96
3-15	Comparison of experimental and theoretical two-way insertion loss of tungsten-epoxy backed array element. .	97
3-16	Theoretical characteristics of single quarter-wave matched slotted array element.	101
3-17	Theoretical characteristics of double quarter-wave matched slotted array element.	102

LIST OF FIGURES (Cont'd)

Figure		Page
3-18	Dispersion curves for the two lowest order dilatational Lamb waves of isotropic waveguide.	106
3-19	Photograph of 180-element double quarter-wave matched array.	109
3-20	Experimental electrical impedance of one element of array in Fig. 3-19	110
3-21	Effect of adding epoxy face plate on experimental electrical impedance of array in Fig. 3-19	112
3-22	Comparison of theoretical and experimental two-way insertion loss of array in Fig. 3-19	114
3-23	Experimental impulse response of 14 elements of array in Fig. 3-19	116
3-24	Experimental impulse of one element of array in Fig. 3-19 reflected off wire target	117
3-25	Comparison of theoretical and experimental angular acceptance of a double quarter-wave matched array element.	119
3-26	Effect of cross-coupling on angular response of an array element.	122
3-27	Effect of phase shift in the cross-coupling on the angular response of an array element	123
3-28	Experimental angular response of an array with a large amount of cross-coupling	125

Figure		Page
3-29	Comparison of theoretical and experimental angular response of tungsten-epoxy backed array element.	126
3-30	Comparison of theoretical and experimental angular acceptance of tungsten-epoxy backed array element with face plate of plastic tape.	127
4-1	Schematic drawing of a backed monolithic transducer element.	130
4-2	Comparison of theoretical angular responses of a monolithic array element	136
4-3	Theoretical angular response of a tungsten-epoxy backed monolithic array element.	137
4-4	Comparison of theoretical and experimental angular response of a lead-backed monolithic array element . . .	139
4-5	Effect of grounding adjacent material to monolithic array element on angular response.	140
4-6	Experimental angular response of tungsten-epoxy backed monolithic array element.	141
4-7	Experimental electrical impedance of monolithic array element.	143
4-8	Theoretical angular response of highly backed monolithic array element.	145
4-9	Theoretical angular response of highly backed PZT-5A monolithic array element with MgO angular filter	147

LIST OF FIGURES (Cont'd)

Figure		Page
4-10	Theoretical angular response of three-layer quarter-wave matched and angular filtered monolithic array element. .	148
4-11	Theoretical angular response of monolithic PVF_2 array element backed with brass.	150
4-12	Comparison of theoretical and experimental angular response of air-backed PZT-5A array element radiating into aluminum at $f = f_o$	154
4-13	Comparison of theoretical and experimental angular response of air-backed PZT-5A array element radiating into aluminum at $f = 0.8\ f_o$	155
C-1	Schematic drawing of path of integration used to calculate the integral in Eq. (3-65)	163

CHAPTER I

INTRODUCTION: GENERAL DESIGN CONSIDERATIONS

The use of high frequency sound waves, or ultrasound, to visualize the internal structure of biological tissue and to detect flaws and defects in engineering materials has gained impetus in recent years. More widespread acceptance of the use of ultrasound in medical diagnosis, and the increased search for improved methods of detecting and characterizing flaws in engineering materials such as nuclear reactor vessels, gas pipelines, and airplane structures have stimulated the development of more effective ultrasonic equipment. This development has been directed towards increasing the scanning rate, the resolution and the sensitivity of acoustic imaging systems used in these applications.

Heretofore most acoustic imaging systems have employed a single acoustic transducer which is mechanically scanned to form an image which is displayed on a cathode ray tube. The image is not formed in real time, it usually has limited resolution because the aperture of a single focused transducer is typically small, and the transducers themselves have not been optimized for maximum bandwidth and efficiency. The non-real time aspect of acoustic imaging in medical diagnostic applications is a severe problem in visualizing moving anatomical structures such as the heart. Furthermore, because of the variability of slow mechanical scanning, a large burden is placed on the operator to create and interpret the images. In the nondestructive testing field, the use of single

mechanically scanned transducer systems is costly and time-consuming, especially when large structures are being examined.

One obvious method of increasing the scan rate and increasing the aperture of the system is to use a number of separate transducers excited one or several at a time which are electronically switched to increase the scan rate. A number of systems are being developed using multiple transducers. Most of these attempt to achieve real time operation at image frame rates greater than 15 frames per second. With arrays of elements of large enough dimensions, diffraction limited resolution can be obtained. The transducers in these systems can be arranged in one-dimensional linear arrays,[1-6] two-dimensional square arrays,[7-10] planar ring arrays,[11,12] and combinations of linear and ring arrays.[13] These systems are usually operated in the pulse-echo mode, with variable electronic time delays to each transducer providing beam steering and focusing if desired.

Although the transducer arrays reported here were designed for use in a particular type of imaging system being developed in this laboratory, most of the design considerations are applicable to any imaging system. The imaging system for which these arrays were built is extensively described elsewhere,[6,14,15] so only a brief description of the system will be included emphasizing those aspects which influence the design of transducer arrays.

The imaging system for which the arrays described here have been designed is based on the synthesis of an electronic lens which can be focused at different depths and rapidly scanned across the field of

view (Fig. 1-1). In this imaging system, gated continuous wave signals are applied to the individual elements of a section of a linear array of acoustic transducers. The signal at each transducer element is delayed in phase in such a manner so that the acoustic energy emitted by the transducer elements has a quadratic variation in phase across the excited elements. This phase variation is constructed to cancel the spatial phase variation in the paraxial approximation so that the acoustic beam is caused to come to a focus in the exact analogue to a normal lens.

The reference phase delays necessary to focus the acoustic beam are provided by a tapped surface acoustic wave delay line. A surface acoustic wave is launched down the delay line with a linear variation in frequency with time. This yields a quadratic phase variation in space at the individual taps on the delay line. Mixing these signals with a reference signal at each element of the array provides a beam with the desired center frequency and a spatial quadratic phase variation. The focal point of this lens is then scanned across the field by the moving surface wave on the delay line, scanning at near the surface wave velocity.

A fixed focus C-scan imaging system (Fig. 1-2) can be built with a two-dimensional field being produced by mechanically scanning the object (or, alternatively, the array) in a plane perpendicular to the front of the array. A most interesting feature of this type of imaging system is the use of two linear arrays of N transducer elements to produce a two-dimensional image of approximately N^2 resolvable spots. This provides potentially large savings in the cost of electronics over

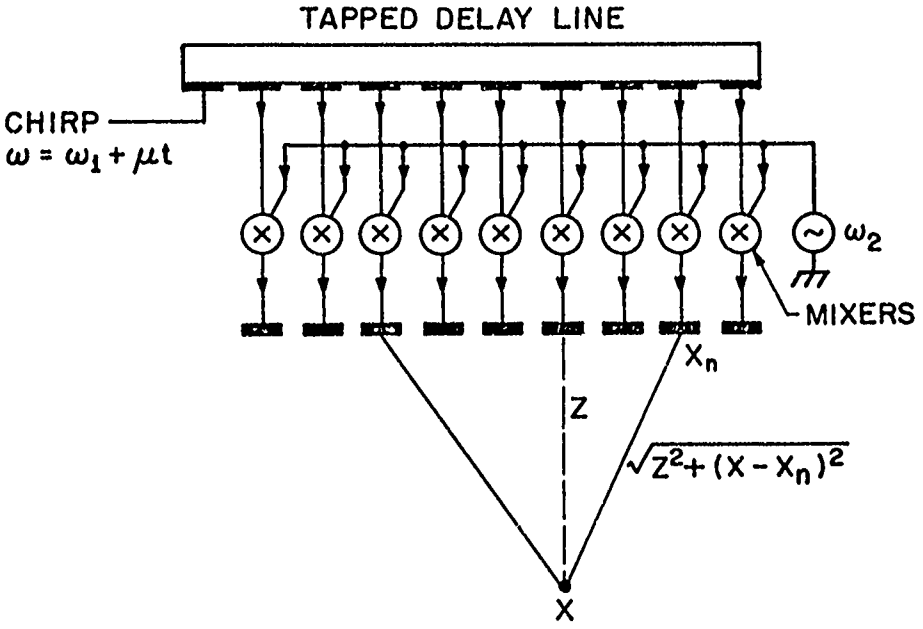

FIG. 1-1. Schematic of an electronically scanned and focused acoustic imaging system using a linear transducer array.

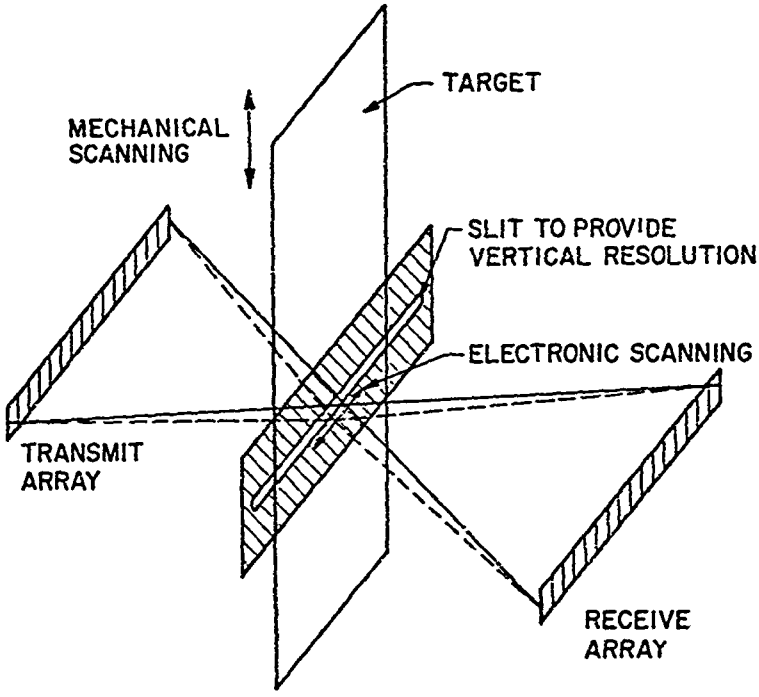

FIG. 1-2. Schematic of a transmission mode C-scan electronically focused imaging system.

systems using two-dimensional arrays with N^2 elements.

The optimum design of the imaging system just described requires: (1) Each element of the transducer array must respond as uniformly as possible over an operating bandwidth of at least 50%. Even higher bandwidths would be desirable in order to change the center frequency of the imaging system for different applications. (2) The efficiency of the transducer consistent with the bandwidth considerations should be as high as possible in order to maximize the sensitivity and the dynamic range of the imaging system. (3) The individual elements should have uniform responses so that array artifacts are not introduced in the acoustic image. (4) The elements of the array should be ideally placed at intervals of half the acoustic wavelength (the Nyquist sampling rate). If the interval is increased, aliasing of the image will be produced from grating sidelobes, in the same manner that grating lobes are produced from a diffraction grating. (5) In order for the electronic lens to present as large a field of view with as wide an aperture as possible, the angular response of the individual elements should be uniform and broad over a 3 dB halfwidth of 15° to 30°. (6) The cross coupling between the individual elements should be as small as possible to reduce array artifacts in the image.

All of these system considerations are important to the performance of pulse-mode imaging systems as well as the system previously described. A few differences should be noted, however. Some pulse-mode systems use a sector scanning technique where the acoustic beam is steered in space like a phased array radar. In this situation, even larger beam halfwidths, typically 45°, are necessary to obtain a large field of view.

In addition, in pulse-mode applications, a broadband electrical signal is applied to the transducer which can then excite any spurious modes in the element which lie near the mode of interest, resulting in array artifacts and loss of signal power. This is not such a severe problem in the variable frequency imaging system previously described where the frequency range of the electrical driving source can be limited to the mode of interest.

Considering these systems requirements, an array design must be formulated which attempts to meet all these requirements or finds the best performance trade-off if the requirements are contradictory. The transducer arrays described in this report are built to operate in frequency ranges between 2 to 5 MHz. This range was originally chosen for demonstration purposes for the variable frequency imaging system. It has general applicability in medical diagnosis because the body tissue attenuation and restrictions on signal power limit the usable frequencies to this range. It is also useful in nondestructive testing applications for the same basic reasons. The techniques described in Chapter III for constructing slotted arrays are limited to less than 10 MHz. Higher frequency arrays can be constructed using the type of array described in Chapter IV or etching techniques similar to those used in integrated circuit technology could be developed for slotted arrays.

The spacing of elements in a linear array is determined by the acoustic wavelength in the load medium; that is, by the center frequency and the acoustic velocity in the load medium. If a 3 MHz center frequency signal is to be generated or received into a water load, the wavelength is then 0.5 mm. The ideal transducer element spacing of

one-half wavelength is then 0.25 mm. The experimental arrays described in this paper were built with 0.5 or 0.64 mm spacing to reduce the number of electronic channels in the system for a given field of view and hence the system cost. Smaller spacings could have been achieved with the techniques used.

The requirement for broad angular beam widths generally determines the maximum width of the transducer element. If the width of the element is several times the acoustic wavelength of the load medium, usually water, the angular beam width will be small. This is easily demonstrated by considering a plane wave incident upon a transducer of finite width L at an angle θ to the surface normal. The phase variation across the face of the element varies as $\exp\{-ikx \sin\theta\}$. Integration over the width of the element yields the normalized output of the transducer, $F(\theta)$, as a function of angle:

$$F(\theta) = 1/L \int_{-L/2}^{L/2} e^{-ikx \sin\theta} \, dx \quad , \quad k = 2\pi/\lambda$$

$$F(\theta) = \frac{\sin(\pi L/\lambda \sin\theta)}{[\pi L/\lambda \sin\theta]} \tag{1-1}$$

where $F(\theta) = 1$ at $\theta = 0$. If one defines the acceptance angle, θ_a, as the angle at which the output has fallen 3 dB, then

$$\theta_a = \sin^{-1}\left(\frac{1.39\ \lambda}{\pi L}\right) \quad . \tag{1-2}$$

If an acceptance angle of 30° is desired at 3 MHz ($\lambda = 0.5$ mm in water), then L must be less than 0.44 mm. As can be seen, if the element

spacing is close enough, this requirement is automatically satisfied. Broader acceptance angles can be achieved with narrower elements. More detailed discussion of this point will be given in Chapters III and IV.

General piezoelectric design considerations, involving improved techniques for achieving broad bandwidth with high efficiency, will be discussed in Chapter II. These considerations are based on the use of multiple quarter-wave matching layers. A new method for choosing the acoustic properties of these layers will be described and the integration of the matching layers into the overall design of a transducer including backing and electrical matching to achieve high efficiency, broad bandwidth, and good impulse response will be discussed in detail. This design approach is a distinct advance in the state-of-the-art since transducer design has been almost totally empirical in the past except in some of the simplest cases.[16,17] In Chapter II these considerations will be limited to simple thin disc transducers which are easier to build and understand theoretically. Also included in this chapter will be a discussion of practical techniques for implementing broadband transducer designs. A single quarter-wave matched transducer was built to illustrate the design principles, and the properties of this transducer will be compared to the theoretical predictions. In addition, a brief description of the measurement techniques used to characterize experimental transducers will be included.

A description of slotted linear transducer arrays will be given in Chapter III. Included in this description will be rationale for our employment of tall, thin transducer elements in the array. These types

of elements offer distinct advantages over the standard short, wide elements employed in most arrays or square cross-section elements including stronger piezoelectric coupling by a factor of two and weaker excitation of spurious modes of the resonator. The characteristics of the resonant mode of these elements as well as other spurious modes which must be considered are discussed. The design of quarter-wave matching layers for these elements will be included as well as that of simple backed transducers. The effective load and backing impedance seen by a small element radiating into an infinite half space has been calculated by variational theory and will be shown. This has not been considered before in the design of elements. Design of practical electrical matching networks to optimize the power radiated into the load will then be described. Finally, aspects of the cross-coupling problem between array elements will be developed from both practical and theoretical considerations. Experimental multi-element arrays either backed or backed and quarter-wave matched, will be described as illustration of the techniques described.

Finally, in Chapter IV, the theory of monolithic arrays, first suggested by Auld,[18,19] will be described and problems and design considerations for this new type of array will be outlined. Experimental results with simple broadband backed monolithic arrays will be described, illustrating the problems involved with the design of such arrays using piezoelectric ceramics such as the lead zirconate titanates and the lead metaniobates. Finally applications of such arrays using materials like PVF_2 and air-backed ferroelectric ceramics radiating into metals will be described.

CHAPTER II

DESIGN OF EFFICIENT, BROADBAND PIEZOELECTRIC TRANSDUCERS

A. INTRODUCTION

The techniques for designing broadband, highly efficient acoustic transducers are common to both array elements and simple thin disc transducers. Since the thickness resonance of thin disc transducers is well understood, new design schemes are more easily checked out with these relatively simple structures than on small array elements. Therefore, this chapter will be concerned with basic mechanical and electrical broadband matching techniques as applied to thin disc transducers. These ideas will then be adapted to the design of array elements in the next chapter.

A design method for achieving nearly 100% transduction efficiency over large bandwidths is presented. The concept is employed that one or more quarter-wavelength acoustic matching sections must be used for efficient broadband operation when a high impedance piezoelectric ceramic is loaded with a low impedance medium, typically water. The fact that the transducer material itself can be regarded as a finite length transmission line is taken into account in the matching procedures. This fact significantly affects the choice of impedances for the quarter-wave matching sections to be employed. In addition, in order to design

transducers with good impulse response, the bandshape of the transducer passband should be Gaussian in form. This criterion is necessary since the impulse response is simply the Fourier transform of the frequency response, and the transform of a Gaussian shaped passband is an RF pulse whose frequency is the center frequency of the passband with a Gaussian shaped envelope. Transducer designs will be formulated with this need in mind.

The electrical input impedance of an acoustic transducer and consequently the insertion loss and other parameters of interest can be determined from the well-known one-dimensional Mason model.[20] In addition, the effects of complex acoustic load and backing impedance on the overall response at the transducer can easily be taken into account with this model. In several papers, notably those of Kossoff,[16] Goll and Auld,[21] and Goll,[22] the effect of various acoustic matching layers at the two acoustic ports of the transducer on the transducer characteristics have been analyzed. These approaches have included the use of high loss backing materials and quarter-wave matching sections. However, the design of transducers with high sensitivity (low insertion loss), broad bandwidth with low ripple, and short-duration impulse response has remained largely a trial and error process. This is because the Mason model is a lumped circuit model. Thus, it does not lend itself easily to physical interpretation of the effects of various acoustic matching layers whose thickness are the order of a quarter wavelength. The optimization of the transducer characteristics, such as the bandwidth, bandshape, and impulse response is, in turn, hampered.

A design procedure is presented here based on the transmission line model of the transducer of Krimholtz, Leedom, and Matthaei,[23,24] shown in Fig. 2-1. This model has the advantage that it retains the intuitively satisfying transmission line nature of the transducer, but replaces the real distributed coupling due to the piezoelectric effect with a single coupling point at the center of the transducer. The differences between distributed and single point couplings are included through a frequency dependent turns ratio in the coupling transformer and a series reactance. Both physical intuition and computation are facilitated, since acoustic matching techniques typically use transmission line formalism in theory and transmission line matching sections in practice. Electrical matching techniques in the frequency range of interest typically use lumped components. The matching techniques have been analyzed and synthesized on a series of computer programs. The electrical input impedance, conversion loss, and impulse response of a transducer can then be easily determined. The accuracy of such techniques is sufficient so that the effects of finite bond thicknesses between matching layers, of stray capacitances and inductances, and of excess electrical resistance show up strongly, and make it possible to determine the nature of errors in the construction.

One transducer has been built to illustrate this design approach and shows characteristics in excellent agreement with the theory. This transducer was constructed using lead metaniobate (Keramos K-81) as the active material, matched into water with a single epoxy matching section, air backed, series inductively tuned, and matched into 50 ohms. This transducer shows the desired flat response over the 40%, 3 dB passband, 6.5 dB round-trip insertion loss at band center, and the predicted impulse response.

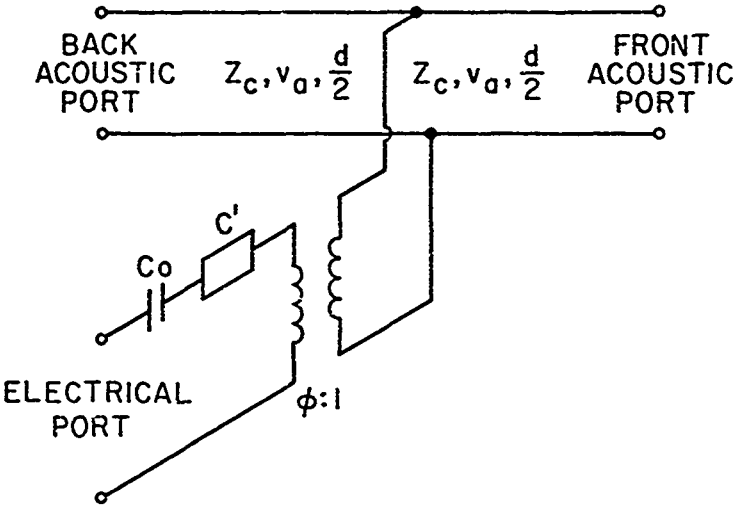

FIG. 2-1. Transmission line model of piezoelectric transducer (after Krimholtz, Leedom, Matthaei).

A double quarter-wave matched transducer was built by Fraser[25] using epoxy and a light borosilicate glass as the quarter-wave plates. This transducer showed 3.2 dB insertion loss and a 70% passband. The author concentrated on applying the matching techniques to array elements.

B. TRANSDUCER MODEL

The transmission line model of Krimholtz, Leedom, and Matthaei,[23,24] hereafter called the KLM model, will be the basis of the transducer designs in this paper. In this model the piezoelectric element of the transducer (the term transducer will be used to describe the overall device consisting of the piezoelectric element, backing, mechanical transformers, and electrical matching components) is described in the following manner: (1) a center-tapped acoustic transmission line with a half-wave resonant frequency ω_o and terminated by front and back acoustic loads; (2) a frequency dependent acoustoelectric transformer connected at the center node; and (3) two series lumped elements, one a capacitance representing the clamped (zero-strain) capacitance of the piezoelectric material, and the other, a purely reactive impedance arising from the distributed nature of electroacoustic coupling.

The transformer has a turns ratio ϕ:1 where

$$\phi = k_T(\pi/\omega_0 C_0 Z_C)^{1/2} \operatorname{sinc}(\pi\omega/2\omega_0) \quad , \qquad (2\text{-}1)$$

and the parameters are defined as:

d = thickness of the piezoelectric element

A = area of the piezoelectric element

ρ = mass density

ϵ^S = clamped dielectric constant

c^D = stiffened elastic constant

v_a = stiffened acoustic velocity

$Z_a = \rho v_a$ = stiffened acoustic impedance

e = electromechanical coupling constant

$k_T^2 = e^2/c^D\epsilon^S$ = effective piezoelectric coupling coefficient

$Z_c = Z_a A$

$\omega_0 = \pi v_a/d$ = half-wave resonant frequency

$C_0 = \epsilon^S A/d$ = clamped capacitance

$\text{sinc}(x) = \sin(x)/x$.

The additional reactance in series with the transformer can be modeled as a variable capacitance of a value

$$C' = -(C_0/k_T^2)\ \text{sinc}(\pi\omega/\omega_0) \ . \qquad (2\text{-}2)$$

As $|C'| >> |C_0|$, it has only minor influence on the operation of the transducer. This model has retained close ties with the actual physical processes in an acoustic transducer, with the advantage of a single central coupling point between electrical and acoustic quantities.

C. BROADBAND MATCHING CRITERIA

The optimum conditions for obtaining maximum bandwidth with minimum insertion loss, where the acoustic parts of a transducer are terminated with pure resistive loads, is calculated. The KLM equivalent circuit for this case is a half-wave transmission line terminated by a load Z_L at one end and a load Z_R at the other. When $Z_L, Z_R < Z_C$, the approximate acoustic Q (Q_a) of this resonator can be determined roughly from a simple lumped circuit representation of the line.[26] The impedances Z_L

and Z_R are transformed to the center tap where their values become Z_C^2/Z_L and Z_C^2/Z_R respectively. The total resistance at the center tap is then $Z_C^2/(Z_R+Z_L)$. The resultant two short-circuited quarter-wave transmission line sections are modeled by expanding the reactance of each line,

$$X_{in}(\omega) = Z_C \tan\left(\frac{\pi\omega}{2\omega_0}\right) \tag{2-3}$$

in a power series representation where the formula

$$\tan x = \sum_{n=0}^{\infty} \frac{2x}{[(2n+1)\frac{\pi}{2}]^2 - x^2} \tag{2-4}$$

is used. Thus the line reactance can be represented in the form

$$X_{in}(\omega) = \sum_{n=1}^{\infty} \frac{2\omega a_n}{\omega^2 - \omega_n^2} + \frac{a_0}{\omega} + \omega L_\infty \quad . \tag{2-5}$$

From this formula a lumped element model can be determined which has the form shown in Fig. 2-2, where the lumped constant element values are $C_0 = -1/a_0$, $C_n = -1/(2a_n)$, and $L_n = (-2a_n)/\omega_n^2$. Combining Eqs. (2-3) and (2-4), the element values for the zeroth and first-order modes for each short-circuited quarter-wave line are $C_0 = \infty$, $L_\infty = 0$, $\omega_1 = \omega_0$, $C_1 = \pi/(4\omega_0 Z_C)$, and $L_1 = (4Z_C)/(\pi\omega_0)$. Since the two lines are connected in parallel, the two equivalent circuits are added in parallel; and the total equivalent circuit representing the resonance near $\omega = \omega_0$ can be represented as shown in Fig. 2-3. The acoustic Q of the transducer can now be found from $Q_a = \omega_0$(stored energy)/(average power loss) or

$$Q_a = \omega_0 RC = \frac{\pi}{2}\frac{Z_C}{Z_R + Z_L} \tag{2-6}$$

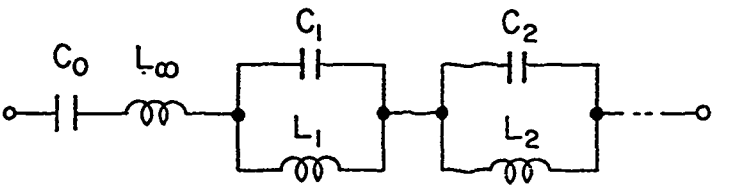

FIG. 2-2. Lumped element representation of reactance of a transmission line.

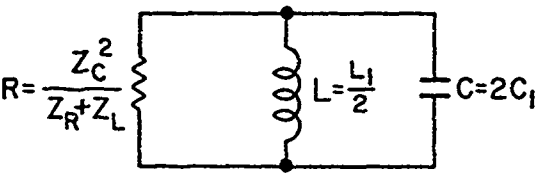

FIG. 2-3. Lumped element representation of the acoustic transmission line of a piezoelectric transducer.

for the parallel RLC circuit shown in Fig. 2-3. On the other hand, the electrical input resistance of the transducer at $\omega = \omega_0$ is

$$R_{a0} = \frac{4k_T^2}{\pi\omega_0 C_0}\left(\frac{Z_C}{Z_R + Z_L}\right) \quad . \tag{2-7}$$

Thus, if the transducer is operated in a simple series tuned circuit such that the tuning inductance L is chosen so that $\omega_0 L = 1/\omega_0 C_0$, and if a constant voltage source is used, the electrical Q, Q_e, of the circuit is simply

$$Q_e = \frac{1}{\omega_0 R_{a0} C_0} = \frac{\pi}{4k_T^2}\left(\frac{Z_R + Z_L}{Z_C}\right) \quad . \tag{2-8}$$

It is apparent from (2-6) and (2-8) that Q_a decreases as $(Z_R + Z_L)$ increases but Q_e increases. For optimum bandwidth is obtained with $Q_e = Q_a$, so that the following condition is reached for the optimum acoustic load impedance:

$$\frac{Z_R + Z_L}{Z_C} = k_T\sqrt{2} \quad . \tag{2-9}$$

Therefore, for widest bandwidth and highest efficiency, one should choose a material with as large a k_T as possible. This lowers Q_e of the circuit and from (2-9), changes the optimum choice of terminating impedances.

An approximate derivation of the parameters of the complete equivalent circuit of the transducer shows that the impedance presented at the transformer terminal, correct to first order in $\Omega = (\omega - \omega_c)/\omega_0$

is

$$Z_{IN} = \frac{Z_C^2}{Z_R + Z_L} - j\Omega\left[\frac{Z_C^3}{(Z_R + Z_L)^2}\right] \quad . \tag{2-10}$$

The reactive part of this impedance is like that of a negative inductance. The reactance seen at the generator, including a series tuning inductance L chosen so that $\omega_0 L = 1/\omega_0 C_0$, is

$$X = \frac{\Omega}{\omega_0 C_0}\left[2 - k_T^2 - 4k_T^2\left(\frac{Z_C}{(Z_R + Z_L)}\right)^2\right] \quad . \tag{2-11}$$

This expression is correct to first order in Ω. The first term in Eq. (2-11) is due to L and C_0 in series; the second term is due to the capacitance C' in the equivalent circuit, and the third term is due to the acoustic loading. It can be seen that the first-order variation of the reactance X with frequency is minimized if $Z_R + Z_L$ is chosen to satisfy Eq. (2-9). Therefore, this choice of terminating impedance satisfies the requirement for optimum matching from a constant voltage source, as well as the requirement for an approximate cancellation of the reactance variation.

If the impedance of the generator is chosen to equal R_{a0}, the efficiency of power transfer to the transducer is

$$\eta = \frac{4R_a R_{a0}}{(R_a + R_{a0})^2 + X^2} \quad . \tag{2-12}$$

Since $R_a = R_{a0}$ at the center frequency, and since the first-order variations of the reactance with frequency are essentially eliminated, the efficiency η will have only fourth-order variations with frequency

due to the variation of X with frequency. First-order variations of R_a with frequency only give rise to second-order variations of η.

These results can be applied to air-backed transducers using high k_T piezoelectric ceramics. In the case of a lead metaniobate transducer ($k_T = 0.32$, $Z_a = 20.6$), the optimal choice of the load impedance transformed to the center tap for a series tuned 100% efficient transducer is 44.4. For PZT-5A ($k_T = 0.5$, $Z_a = 34$), this impedance is 48.2. It will be shown in the next section that transformed load impedances close to these estimates can be achieved with one quarter-wave plate for water-loaded lead metaniobate and two quarter-wave plates for water-loaded PZT-5A if the transducer ceramic is taken into account in the matching scheme.

D. FRONT ACOUSTIC LOAD LINE

The acoustic matching problem for a piezoelectric ceramic used to excite an acoustic wave in water is now considered. The impedance of the transducer material is typically 20 to 35 and that of the water is 1.5. Thus, in the KLM model, the impedance looking into the right hand acoustic load line is like that of a transmission line with essentially a short circuit termination. The impedance is very high at the center frequency, but drops quickly to low values. Consequently, the bandwidth of the transducer is very small, unless the impedance at the center is kept low by using a backing termination.

Quarter-wave impedance transformers between the load and the piezoelectric ceramic will broaden out the response characteristics, giving higher efficiency than transducers damped by a matched backing

and broader acoustic bandwidth than undamped transducers. In the past, such transformers have been designed to match the load impedance to the characteristic impedance of the transducer material at the center frequency. A better procedure, which is adopted here, is to design the transformers to give a desirable impedance at the center terminal of the KLM model. Thus, following the earlier discussion, the front half of the transducer is itself treated as a quarter-wave matching layer, in addition to the quarter-wave matching layers bonded to it. As opposed to the usual design procedure, Z_1, the impedance of the first matching section is chosen to be the transducer material, so $Z_1 = Z_C$. The value of Z_{IN}, the input impedance to this section, is then determined. Thus a broadband match is obtained because use is made of the extra matching layer which already exists in the device.

The design of quarter-wave transmission line matching sections has been formulated by Collins,[27] Riblet,[28] and Young,[29] and others. Their designs call for the transmission line reflection coefficient magnitude $|\Gamma|$, or, alternatively, the power loss ratio $P_{LR} = [1/(1-|\Gamma|^2)]$ to exhibit either a maximally flat or Tchebycheff response over the desired frequency passband. Larger passbands are achieved by the addition of more transformer sections.

A similar approach can be used in the design of the acoustic load line, although the acoustic impedance mismatches are typically much larger than the microwave ones, so higher order terms are much bigger and should be included in the calculation of the reflection coefficient. Nevertheless, the design formulae developed for two and three-layer transmission line sections can be applied to the acoustic case, and reasonably good results are obtained in exact numerical solutions.

As an illustration, the impedance formulae for the binomial transformer are given which gives close agreement to the maximally flat case for a small number of matching sections:

$$\ln \frac{Z_{n+1}}{Z_n} = 2^{-N} C_n^N \ln \frac{Z_T}{Z_{IN}} \qquad (2\text{-}13)$$

where

Z_T = terminating load impedance

Z_{IN} = input impedance of the transmission line system

Z_n = n^{th} quarter-wave matching section impedance

C_n^N = binomial coefficient = $\frac{N!}{(N-n)!\, n!}$

Z_R = transformed load impedance at the right hand end of the transducer transmission line.

The results shown in Table 2-1 are used as the starting basis for the transducer designs reported in this paper. In each case, Z_1 is the impedance Z_C of the transducer material.

As an example, consider the design of a transducer to be built using lead metaniobate with a water acoustic load. One bonded matching section is to be employed, and a maximally flat passband is desired for the front load line. Using Table 2-1 for the two-layer transformer, and taking $Z_T = 1.5$ and $Z_C = 20.0$, the input impedance of the acoustic load line (Z_{IN}) is found to be 47.4, over twice the material impedance. This is very close to the optimum value of 44.4 calculated in Section II.C.

TABLE 2-1

Matching Formulae

	Z_{IN}	Z_2	Z_3	Z_R
One Section	Z_C^2/Z_T			Z_T
Two Sections	$Z_C^{4/3}/Z_T^{1/3}$	$Z_T^{2/3}\ Z_C^{1/3}$		Z_C^2/Z_T
Three Sections	$Z_C^{8/7}/Z_T^{1/7}$	$Z_T^{3/7}\ Z_C^{4/7}$	$Z_T^{6/7}\ Z_C^{1/7}$	$Z_2^2/Z_3^2\ Z_T$

The impedance of the matching layer (Z_2) is found to be 3.56, which differs markedly from the value of 5.48, the value calculated if the ceramic were assumed to be an infinite acoustic transmission line.

The power loss ratio (P_{LR}) through the matching layers is plotted as a function of frequency for both cases in Fig. 2-4. As can be seen, the ideally maximally flat response is obtained for the case when the matching layer impedance is 3.56. In Fig. 2-5, a comparison of the acoustic load line input impedances for both cases is shown, and rapidly varying input acoustic impedance for the case $Z_2 = 5.48$ is demonstrated.

This system tends to give a broader acoustic bandwidth, because two matching layers have been taken into account and a broader electrical bandwidth with better efficiency, because it presents a higher electrical impedance at band center.

A similar calculation for a PZT-5A transducer matched into water ($Z_C = 34$) yields a value of Z_{IN} for two matching sections of 96.2;

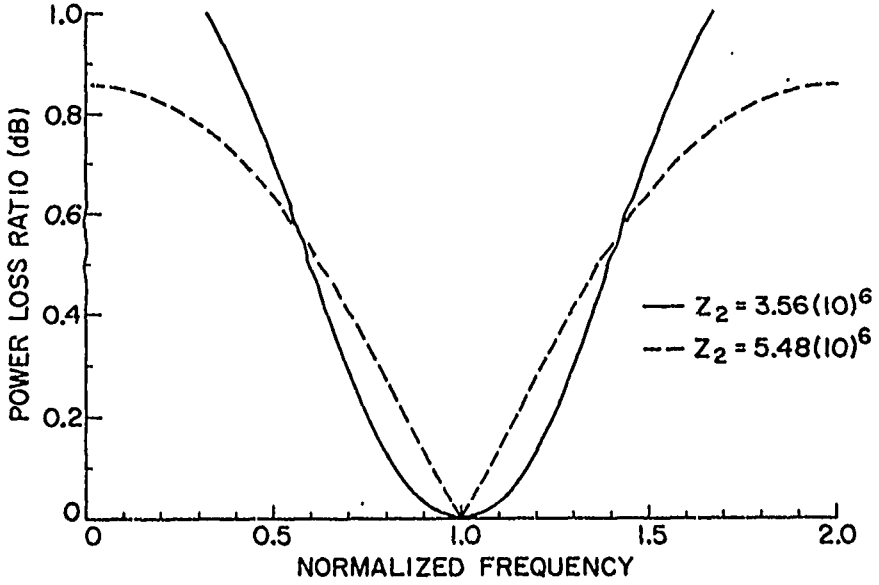

FIG. 2.4. Power loss ration of front acoustic load line of lead metaniobate transducer matched with single quarter-wave plate.

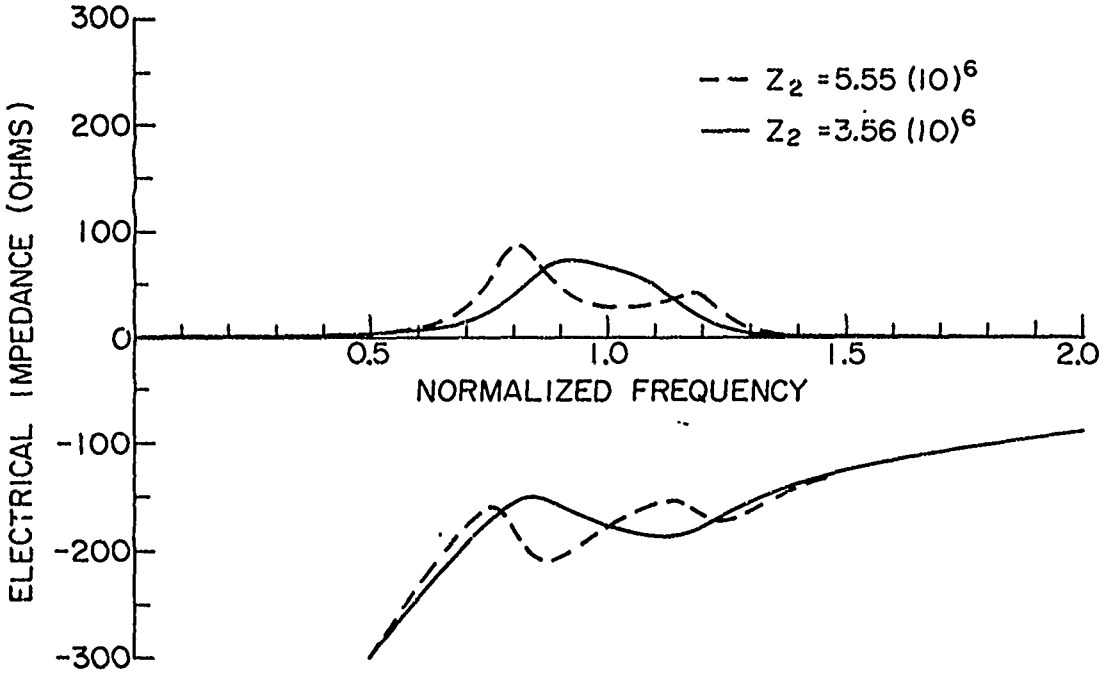

FIG. 2-5. Electrical impedance of lead meta..iobate transducer matched with single quarter-wave plate.

with three sections, $Z_{IN} = 53$, $Z_2 = 8.9$, $Z_3 = 2.34$. The value of Z_{IN} for the three section matched system is slightly larger than the optimum value of $Z_{IN} = 48.2$ estimated in Section II.C.

Therefore, it is concluded that the optimum lead metaniobate transducer matched to water requires one extra matching layer with an impedance of 3.56, while the PZT-5A transducer requires two matching layers of impedances 8.92 and 2.34, respectively.

Wider passbands can be obtained for a given number of matching sections with Tchebycheff response if passband ripple can be tolerated. As will be shown in the next section, the acoustic backing line, in general, limits the usable bandwidth of the transducer, so that this filter response is not as useful as it might be. Moreover, the Tchebycheff filter response yields steep "skirts" on the frequency response, which is undesirable in pulse-mode applications.

E. EFFECT OF BACKING

In the transmission line model, the acoustic impedance seen at the center node is the parallel combination of the input impedances of the front acoustic load line and the back acoustic load line. Ideally, the back load line should be designed to absorb as little power as possible and to maintain or enhance the passband characteristics. In the simplest case, where the transducer is air-backed, the backing line consists virtually of a shorted quarter-wave section of piezoelectric ceramic. The back load line input impedance is then

$$Z_{IN}^{L} = j Z_C \tan\left(\frac{\pi}{2}\frac{\omega}{\omega_0}\right) \qquad (2\text{-}14)$$

At the center frequency, Z_{IN}^{L} is infinite and has no effect on the acoustic impedance. However, Z_{IN}^{L} decreases rapidly to zero at $\omega/\omega_0 = 2$ and $\omega = 0$, and limits the useful bandwidth of an air-backed single quarter-wave matched transducer to about 45%.

The effect of the shorted back load line on the input acoustic impedance is shown in Fig. 2-6, for the lead metaniobate transducer previously discussed. As can be seen, the bandwidth of the passband is considerably reduced and the band shape is considerably altered. The combination of the front load line with a low impedance shunted back load line is an optimum for high efficiency, broadband designs. This is because the imaginary part of Z_{IN} varies linearly with frequency over the passband, so it tends to cancel out some of the errors introduced by the electroacoustic transformer and a simple series tuned electrical tuning network.

The efficiency and bandwidth of an air-backed transducer can be estimated for the case where Eq. (2-9) is satisfied. At band center, the KLM equivalent circuit is shown in Fig. 2-7 for the untuned case and a generator impedance of $Z_0 = \sqrt{R_{a0}^2 + 1/\omega_0^2 C_0^2}$. Since $C_1 = \infty$ at center frequency, its impedance can be ignored, and the efficiency of power transfer from generator to load is

$$\eta = \frac{2}{1 + \sqrt{1 + (\pi/2\sqrt{2}k_t)^2}} \quad . \qquad (2\text{-}15)$$

For PZT-5A ($k_t^2 = 0.25$), η is 58% while for lead metaniobate ($k_t^2 = 0.10$), η is 43%. These efficiencies correspond to minimum round-trip insertion losses of 4.7 dB and 7.3 dB, respectively. It is clear that the higher the value of k_t^2, the greater the untuned efficiency.

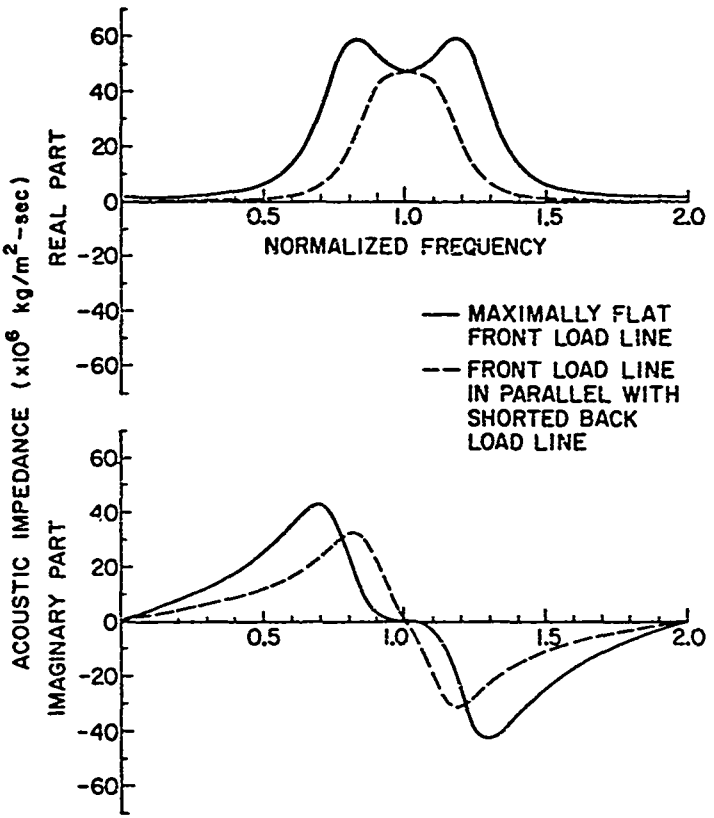

FIG. 2-6. Effect of shorted back load line on acoustic impedance of maximally flat front load line. Lead metaniobate transducer (1.27 cm diameter).

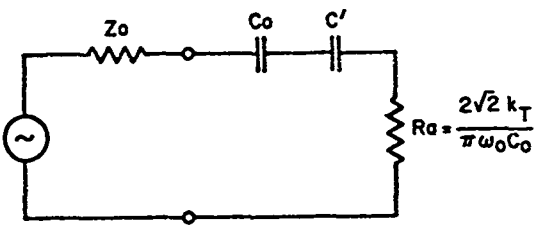

FIG. 2.7. Equivalent electrical lumped circuit of transducer terminated by air and optimum load at the acoustic ports.

The addition of series inductive tuning would lower the minimum loss to 0 dB at band center. The bandwidth can be estimated from the electrical Q where $R_0 = R_{a0}$ and for optimum power transfer and condition (2-9) is satisfied. Therefore,

$$Q_e = \frac{1}{\omega_0(R_0 + R_{a0})C_0} = \frac{1}{2\omega_0 R_{a0} C_0} = \frac{\pi}{4\sqrt{2}\, k_T} \qquad (2\text{-}16)$$

For $k_T^2 = 0.25$ and 0.10, $\frac{(\Delta\omega)3dB}{\omega_0} = \frac{1}{Q_e}$ would be 90% and 51%, respectively.

The next simplest back load line design would be the addition of a resistive load of impedance Z_L to the ceramic quarter-wave section. This is accomplished in practice by bonding a high loss material to the back of the piezoelectric ceramic to simulate an infinite transmission line, so that no power is reflected back into the transducer from the back. The effect of resistive loads of varying impedance on Z_{IN} of the lead metaniobate transducer previously described is shown in Fig. 2-8. In general, as would be expected, the midband impedance is considerably reduced as the backing impedance is increased. When the backing impedance approaches Z_C, Z_{IN}^L becomes entirely resistive and equal to Z_C. It should be noted that most of the available power in this case is radiated into the back load line, since its impedance would be only about 40% of that of the front load line. With a large number of quarter-wave plates on the front load line, Z_{IN}^R would approach Z_C, and the round-trip insertion loss would approach 6 dB at best. In this case the Z_{IN} drops in value so broadband electrical matching becomes more difficult. Thus, this type of transducer would be optimized by using several quarter-wave plates with a more complicated

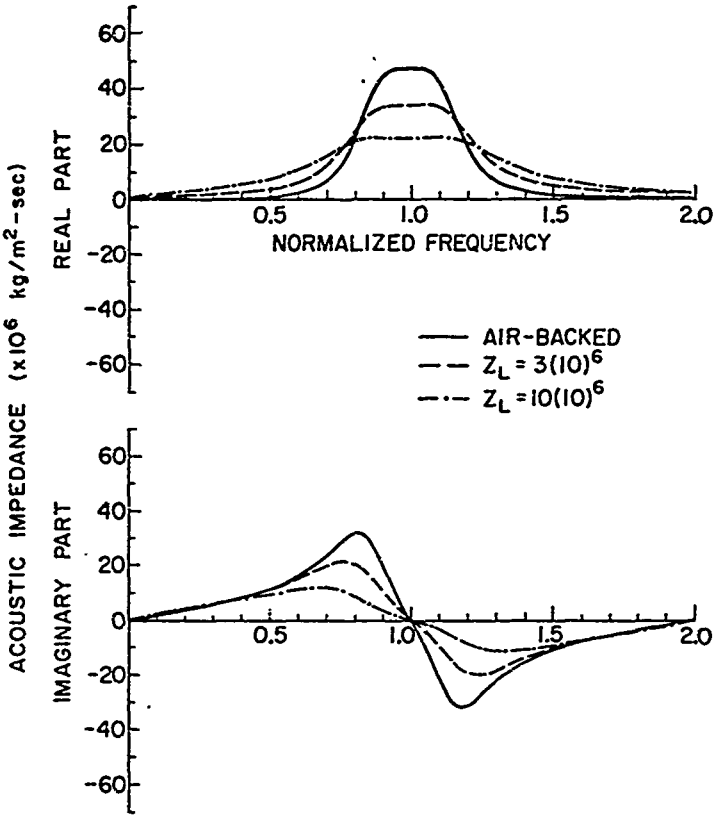

FIG. 2-8. Effect of resistively loaded back load line on acoustic impedance of maximally flat front load line. Lead metaniobate transducer (1.27 cm diameter).

matching network than just a simple inductance. Alternatively the matching network could be omitted at the expense of a decrease in efficiency.

It is worthwhile to consider here the important case where a transducer is terminated by a matched backing ($Z_L = Z_C$) and no quarter-wave matching is used. In this case, most of the power is radiated into the matched backing. If the voltage at the center node in the KLM model is V, the power emitted at the center frequency into the left and right hand sides is $V^2 Z_L / 2Z_C^2$ and $V^2 Z_R / 2Z_C^2$, respectively. Following previous arguments, since the total radiation resistance is $R_{a0} = 4k_t^2 Z_C / [\pi \omega_0 C_0 (Z_R + Z_L)]$ the maximum efficiency of an untuned transducer is

$$\eta = \frac{2Z_R}{(Z_L + Z_R)\left(1 + \sqrt{1 + \pi(Z_R + Z_L)/4k_t^2 Z_C}\right)^2} \quad . \qquad (2\text{-}17)$$

The maximum efficiencies for PZT-5A and lead metaniobate are 0.9% and 1.6%, respectively. This corresponds to round-trip insertion losses of 41 dB and 36 dB, respectively. Note that in this case, the lead metaniobate transducer has greater efficiency than the PZT-5A one because its lower acoustic impedance matches water better.

The use of a lossy backing of relatively low impedance is useful in the design of a quarter-wave matched transducer, however. The band shape of Z_{IN} for a backed transducer rounds off as Z_L is increased, and becomes Gaussian shaped. The impulse response of the transducer is therefore improved, as will be described. The problem for the designer, then, becomes compromising band shape versus insertion loss for this particular transducer configuration. A very low impedance backing of about 3 appears to be adequate for the single quarter-wave matched lead metaniobate transducer described above.

If the backing impedance were to be made large with respect to Z_C, Z_{IN}^L would approach a short circuit at the center frequency and increase to some peak value at approximately $f/f_o = 0.5$ and $f/f_o = 1.5$. The transducer could then be operated on a quarter-wave or three-quarter-wave resonance. Since, in this case the electroacoustic transformer has a better response at low frequencies, a transducer built on this principle could be successfully operated as a quarter-wave transducer with only slight effects from the higher resonance. This design has been used by Bui, Shaw, and Zitelli[30] for a very broad bandwidth transducer which uses low impedance ($Z_C = 3.8$) PVF_2 as the piezoelectric element, mounted on a high impedance ($Z = 31$) brass backing. In this case, the electrical coupling is weak ($k_T^2 \approx 0.012$), but the acoustic matching to water is very good. Therefore, a large bandwidth untuned transducer can be constructed with excellent impulse response, as can be seen in Figs. 2-9(b) and 2-9(c). This design would be difficult to use for immersion transducers employing ferroelectric ceramics, since no backing material exists whose impedance is considerably higher than theirs.

F. ELECTRICAL PORT

In order to minimize the insertion loss, the electrical input impedance (Z_{IN}) of a transducer should be entirely real over the passband, and the radiation resistance (R_a) should equal the electrical source resistance Z_0. For a lossless air backed transducer, the radiation resistance of the acoustic load is R_a. If the transducer has a resistive load on the back load line, the component of interest must be separated out from R_a. In addition, the frequency dependence of R_a should be tailored to fit some bandshape criteria, such as a Gaussian form, for

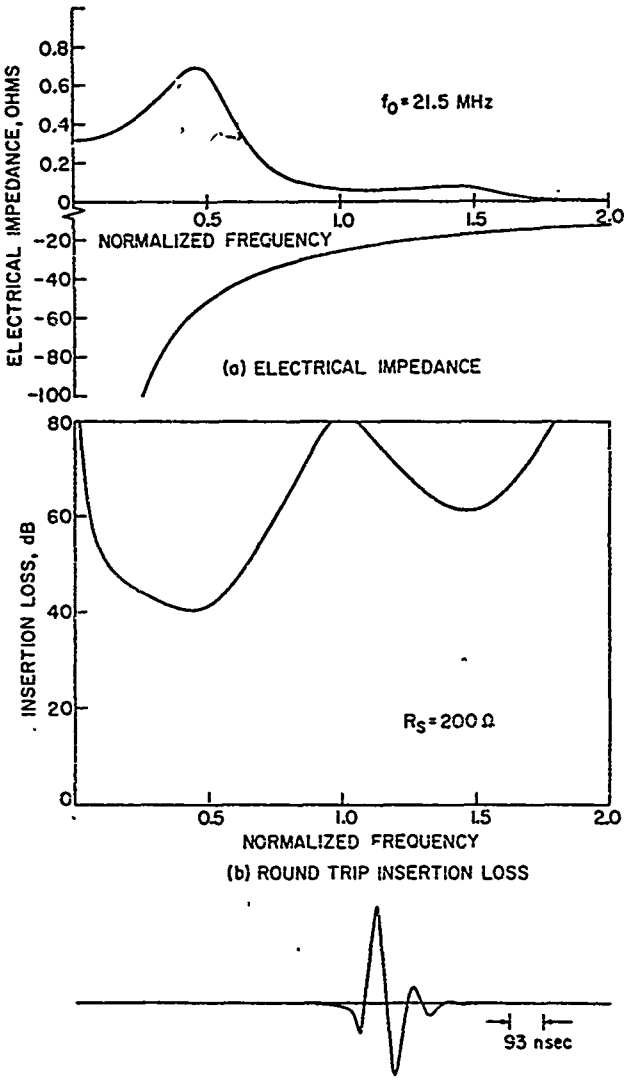

FIG. 2-9. Characteristics of a highly backed, water loaded PVF_2 transducer.

optimum impulse response. As we have seen, the design of a low loss, broadband matching network is considerably eased if the electrical Q of the transducer is low to begin with, which means using materials with large electroacoustic coupling constants (k_t^2).

The electroacoustic transformer in the transmission line model is frequency dependent, unlike the transformer in the Mason model. The dependence varies as $\text{sinc}(\pi\omega/\omega_0)$. This function decreases with ω near $\omega = \omega_0$, so the radiation resistance tends to be higher at the low frequency side of resonance. In the range $0.5 < \omega/\omega_0 < 1.5$ the variation of ϕ with frequency is almost linear with frequency. This effect is detrimental to the response of the transducer and should be compensated, either by an electrical tuning network or by weighting the high frequency side of the passband by suitable acoustic matching. The latter approach, suggested first by Goll,[21] is easily accomplished by increasing the thickness of quarter-wave plates by a small amount, usually between 4 and 10%. The amount of this "skewing" has been determined empirically by trial and error computer simulation of the input impedance and insertion loss of the transducer in question. The effect of the quarter-wave plates operating at a slightly lower frequency than the ceramic compensates the frequency dependence of the transformer turns ratio, as can be seen in Fig. 2-10. The result is an approximately symmetrical bandshape, about a center frequency 90 to 96% of the half-wave resonant frequency of the ceramic.

The series reactance lumped element has a frequency dependence which varies as $(\sin \pi\omega/\omega_0)/\omega^2$. This reactance is always small compared to that of the capacitive reactance $1/\omega C_0$ of the transducer and can essentially be neglected in the design of octave bandwidth transducers.

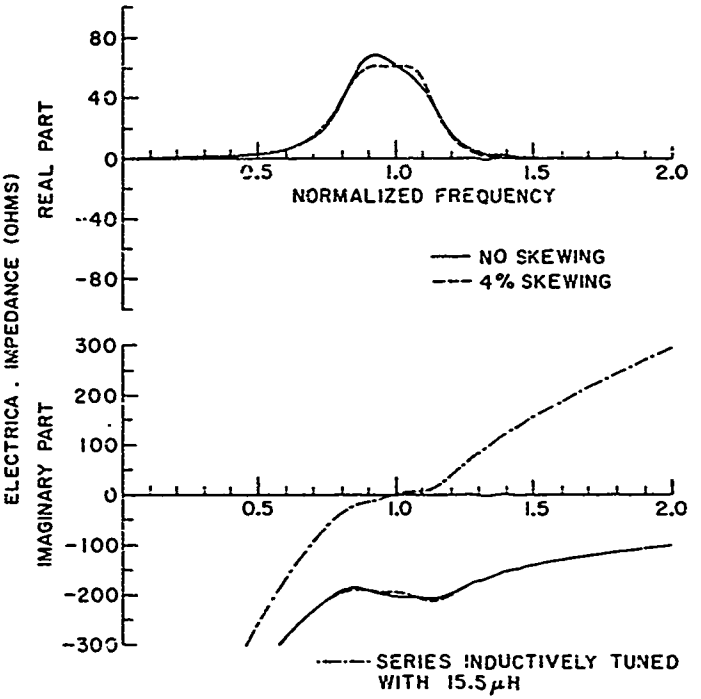

FIG. 2-10. Effects of increasing the thickness of single quarter-wave plate 4% and series inductive tuning on electrical input impedance. Lead metaniobate transducer (1.27 cm diameter).

Wider bandwidth transducers would probably require an iterative numerical electrical filter design program to compensate for this term.

The final intrinsic electrical element in the transmission line model is a capacitor representing the zero-strain (clamped) capacitance of the piezoelectric material. As we have seen, for minimum insertion loss, this capacitance must be tuned out. This is most easily accomplished with a series inductance tuned for zero reactance at the center frequency, a procedure which is adequate for materials with large k_t . Generally, a more sophisticated tuning network would be desirable for broadband operation.

In all cases, the design of an electrical matching network is highly dependent on the acoustic termination of the transducer. For the particular arrangement where the front matching plates are chosen to be maximally flat, the total imaginary part of the electrical input impedance is negative but varies like a negative inductance over the passband; therefore, a series inductance just cancels the imaginary part of the impedance over the entire passband, as is discussed in Section C, and as can be seen in Fig. 2-10. Thus, the input impedance becomes entirely real over the passband as desired. An electrical transformer then can be employed to scale R_a up (or down) to the source impedance Z_0 . This is the design technique employed for all the experimental transducers, including array elements, described in this paper.

G. TRANSIENT RESPONSE

The transient response of a transducer excited by a delta function input can be obtained simply by taking the Fourier transform of the frequency response.[31] The cleanest response is obtained when the envelope

of the output pulse is Gaussian so that the wave packet amplitude decreases monotonically to zero from its maximum amplitude. This requires that the bandshape of the frequency response be Gaussian shaped as well. This fact can be clearly seen in Fig. 2-11 where a comparison of two impulse responses is shown, one of Gaussian bandshape, the other of square bandshape of equal 3 dB bandwidth. The time response corresponding to these two bandshapes, neglecting nonlinear phase variations, are given in Eqs. (2-18) and (2-19), respectively:

$$F(t) = A \cos \omega_0 t \; e^{-a\Omega t^2} \qquad (2\text{-}18)$$

$$F(t) = B \cos \omega_0 t \; \text{sinc} \; (b\Omega t) \quad , \qquad (2\text{-}19)$$

where ω_0 is the center frequency of the passband and Ω is the 3 dB bandwidth, and the amplitude is taken to be maximum at $t = 0$.

As described earlier, air-backed transducers with maximally flat front load lines yield square bandshapes. The addition of a relatively low impedance backing causes the bandshape to be more Gaussian, thus yielding a better impulse response. This is obtained at the expense of some loss in bandwidth and sensitivity. Another possibility for obtaining better impulse response for air-backed transducers is to choose a set of quarter-wave matching layers which satisfies a filter response other than the maximally flat set. This point has not been explored further by the author at this time.

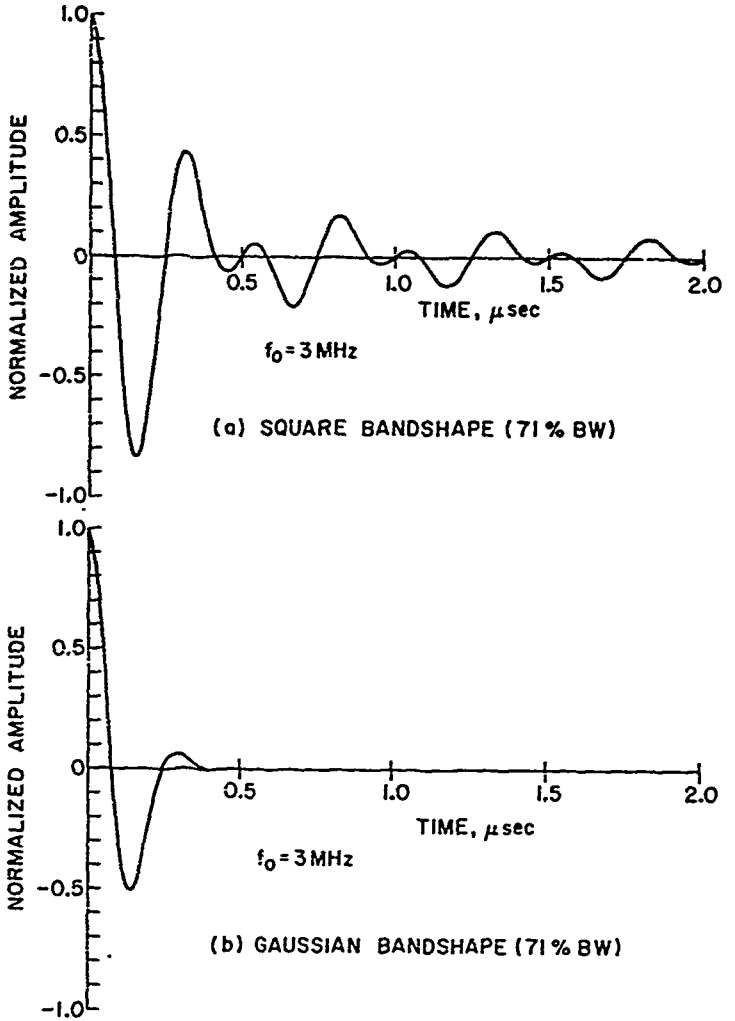

FIG. 2-11. Comparison of transient responses of linear filters with square and Gaussian bandshapes.

A set of computer programs, written by J. Fraser, has been used to analyze the KLM model for theoretical studies on transducers. The impulse response is calculated by taking the fast Fourier transform of the theoretical bandshape, including all the nonlinear phase variations. Other quantities such as the electrical impedance and insertion loss can be easily obtained with these programs.

H. EXPERIMENTAL RESULTS

A 12.7 mm diameter, air-backed, single quarter-wave matched transducer was built using lead metaniobate as the active material. The parameters for the ceramic, supplied by Keramos Corporation and designated K-81, were measured using the technique of Bui, et al.,[32] and determined to be as follows: $k_t^2 = 0.10$; mechanical Q, $Q_M = 24$; $\omega_0/2\pi = 2.06$ MHz ; $\varepsilon_{33}^S = 266\ \varepsilon_0$; $Z_c = 20.0$. A matching plate was fabricated by lapping a piece of Dow Epoxy Resin 332, hardened with metaphenylene-diamine to a thickness equal to a quarter wavelength at $1.01\ \omega_0$. The epoxy had a characteristic impedance of 3.38, slightly less than the optimal maximally flat value of 3.56.

The ceramic and epoxy plates were cleaned in organic solvents, heated for several hours to remove any absorbed solvents, and assembled in a dust-free laminar flow hood. The plates were bonded with epoxy under a nonuniform pressure device, as suggested by Papadakis,[33] in order to remove trapped air bubbles and to insure a negligibly thin bond. The resulting assembly was mounted into a plastic housing. This transducer was measured, and later a 13.9 μH series tuning inductor and BNC connector were added.

The input electrical impedance of the untuned transducer is shown in Fig. 2-12. Excellent agreement with the theoretical calculation, which includes the finite loss of the ceramic, can be seen. The experimental electrical impedance was obtained using a Hewlett-Packard Vector Impedance Meter. It can be seen that the impedance is very flat over the passband and slightly tilted because of the frequency dependence of the electroacoustic transformer. No quarter-wave plate "skewing" was used in this experiment. The imaginary part of the impedance shows a slight divergence from the theory at low frequencies. This effect has not been satisfactorily explained yet, but could be due to two-dimensional effects not taken into account in the one-dimensional model.

An inductor was made by wrapping eleven turns of wire about a ferrite core, yielding 13.9 μH of inductance. This is slightly less than the 15.9 μH desired. The two-way insertion loss of this transducer was measured by transmitting an acoustic wave from the transducer, excited by a 50 ohm internal impedance tone-burst generator. The amplitude of the output of this generator into a 50 ohm load was measured at each frequency, so as to determine the available power. The transmitted energy was reflected off of a perfectly reflecting air-water interface and received by the transducer loaded by the same 50 ohm generator. A high impedance probe was used to measure both the transmitted and received electrical voltages. The two-way insertion loss was measured by comparing the available transmitted voltages and the received voltages as a function of frequency and was compared to the theory, as shown in Fig. 2-13. The insertion loss of the transducer was 6.5 dB at midband, compared to the theoretical value of 1 dB. The 3 dB bandwidth is 40%, as predicted, and the bandshape is flat over the passband, as

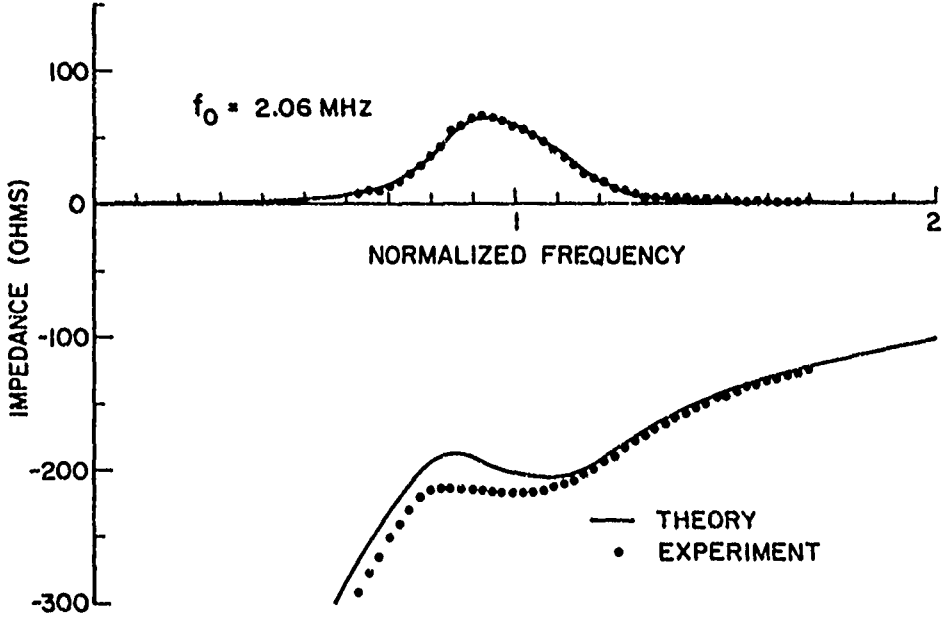

FIG. 2-12. Comparison of experimental results with theory for single quarter matched lead metaniobate transducer: Electrical impedance.

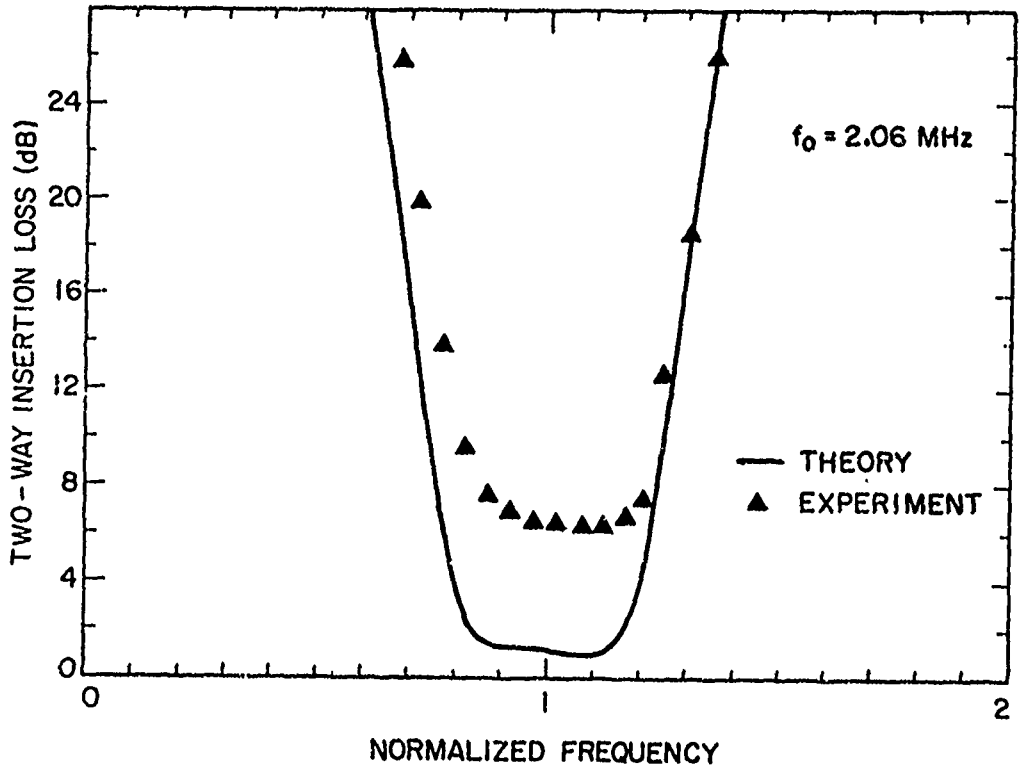

FIG. 2-13--Comparison of experimental results with theory for single quarter matched lead metaniobate transducer: Two-way insertion loss.

designed. The additional 5.5 dB loss of the transducer over what was predicted is thought to be due to internal losses in the inductor and to phase cancellation, since the epoxy quarter-wave plate was slightly wedge shaped.

A comparison of the experimental and theoretical impulse response of the untuned transducer is shown in Fig. 2-14. The theoretical impulse response was calculated by taking a fast Fourier transform of the transducer transfer function, as previously described. The experimental results were obtained by shock exciting the transducer with a Panametrics Pulser (Model 5050PR), using a 50 ohm damping resistor in the circuit and digitizing the reflected echo off an air-water interface with a Biomation 8100 transient recorder sampled at a rate of 100 MHz. As can be seen, the agreement between theory and experiment is excellent.

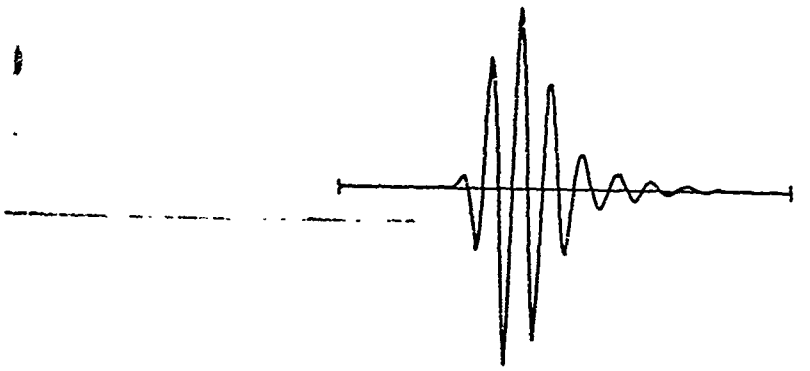

THEORETICAL

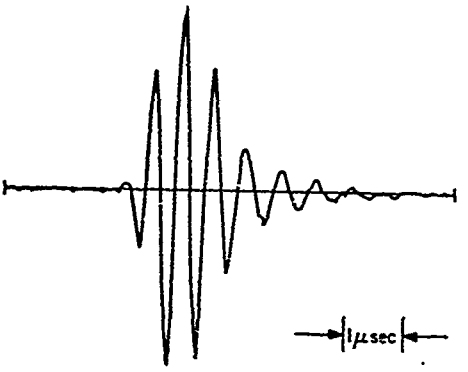

EXPERIMENTAL

FIG. 2-14. Comparison of experimental results with theory for single quarter matched lead metaniobate transducer: Impulse response.

CHAPTER III

SLOTTED TRANSDUCER ARRAY DESIGN

A. INTRODUCTION

The design of linear transducer arrays constructed of tall thin elements is described in this chapter. Experimental results with simple backed and double quarter-wave matched and backed arrays are also discussed. The basic structure of these arrays, illustrated in Fig. 3-1, involves mounting each piezoelectric element on a lossy backing medium, and radiating into a load medium through several matching layers. A face plate, acoustically similar to water, is used to keep water from getting between the elements and introducing acoustic and dielectric cross-coupling. The choices of matching layers and backing materials are based on the concepts described in the previous chapter. In addition, there are several problems, both theoretical and technological, which are unique to the design of small element arrays. These problems are summarized in Table 3-1 and will be addressed in this chapter. These include description of the extensional mode of an element of near square cross-section, description of the effective load impedance seen by an element, design of acoustic matching layers, and effects of cross-coupling between elements of the array.

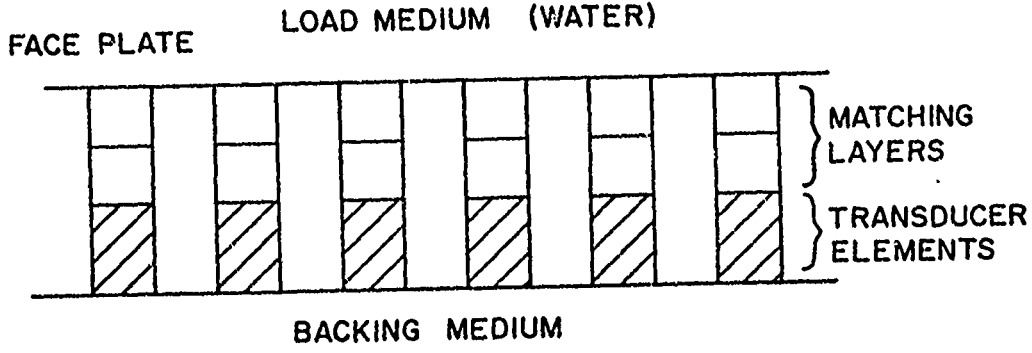

FIG. 3-1. Schematic drawing of transducer array elements.

TABLE 3-1

ACOUSTIC TRANSDUCER ARRAY DESIGN

Theoretical Problems	Technological Problems
Description of extensional mode of transducer element of near square cross-section	Design of transducer element with desired center frequency and bandwidth
Description of effective backing impedance seen by slotted element	Fabrication of high loss, high impedance acoustic backing
Effect of finite bond thickness on response of element	Fabrication of acoustic bonds on the order of 1 μm or less
Design of acoustic matching schemes into load medium	(a) Selection of λ/4 matching materials (b) Slotting composite material structure to create acoustically matched elements
(a) Description of cross-coupling between array elements (b) Effect of cross-coupling between elements on element response	Fabrication of strong, thin face plate with low acoustic cross-coupling

B. MODEL OF A NARROW SLOTTED ELEMENT

It is desirable in focused imaging systems like the one described in Chapter I to space array elements one-half wavelength apart to avoid grating sidelobes in the image in direct analogy to the grating lobes in a diffraction grating. In this instance, the elements would have a width (L) comparable to the height (H) as shown in Fig. 3-2. It is assumed in all future discussions that the length of the element in the y-direction is large compared to the other dimensions so that the structure is basically two-dimensional. That L and H are comparable is easily demonstrated by noting that at 3 MHz the acoustic wavelength (λ_w) in water is 0.5 mm so that the maximum width of an element spaced at $\lambda_w/2$ is 0.25 mm. In the experimental arrays reported in this work, L is always in the range 0.25 to 0.30 mm and the element spacing is about 0.5 to 0.64 mm. With elements constructed of PZT-5A piezoelectric ceramic, the stiffened extensional velocity in the z-direction is about 3.8 $(10)^5$ cm/sec. Therefore, to operate the transducer element on the fundamental half wavelength resonance at 3 MHz, the height of the element must be on the order of 0.63 mm. In this case, then, it can be seen that $H \approx 2L$, a configuration dictated by system design considerations. The boundary conditions for a piezoelectric resonator of these dimensions are obviously much different from the thin disc resonator discussed in Chapter II where $L >> H$. Consequently, the simple theory of the thin disc resonator cannot be applied to this structure without modification.

When both lateral dimensions of a transducer are comparable to the height, the longitudinal strains $S_1(S_{xx})$ and $S_2(S_{yy})$ cannot be taken as zero. Therefore, a one-dimensional model cannot in general be used to

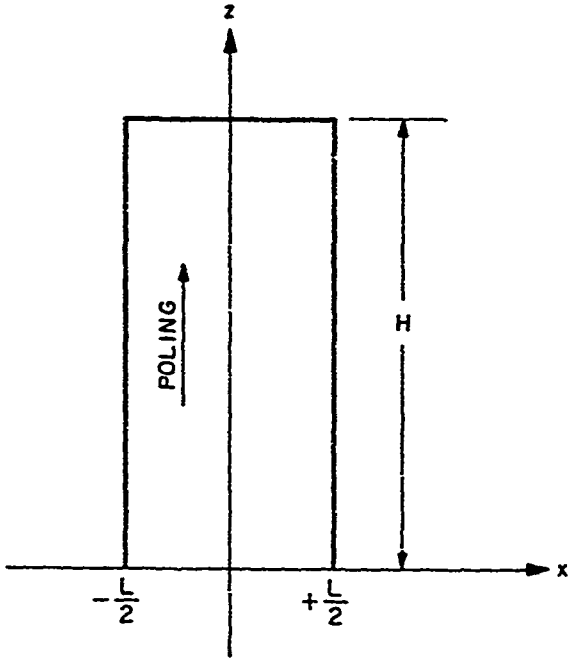

FIG. 3-2. Schematic drawing of piezoelectric ceramic element sho..ng poling direction and coordinate system.

describe the response of the transducer. In a linear array where the transducer element is essentially a two-dimensional structure as shown in Fig. 3-2, there is strong coupling between the desired zeroth-order extensional resonance (z-direction) and the zeroth-order lateral extensional resonance (x-direction) when the element has near square cross-section.[34] In this case, the frequency of the desired lower branch of the coupled modes is significantly down shifted. In addition, the undamped upper branch of the coupled modes is very close to the frequency of the lower branch and will be excited in any broadband system, yielding a peaky transducer bandshape. For these reasons, transducer elements of near square cross-section should be avoided in broad bandwidth systems.

Some unfocused acoustic imaging systems have been designed in which several elements are excited simultaneously and the echoes processed into an image.* These systems work with elements spaced many wavelengths apart and so the elements have lateral dimensions much greater than the thickness. These elements would be operated in a mode similar to the thin disc mode and the acoustic response will include lateral resonances and harmonics. Little discussion of this type of element will be included in this work, however, since the emphasis was placed on tall, thin elements suitable for the electronically scanned and focused system. Some of the discussion of tall, thin elements could be easily extended to wide elements.

*Several commercial systems are presently designed this way including ones built by Acoustic Diagnostic Research, Panasonics, Unirad, and Rohe.

If the height of the element is greater than about twice the width, the lateral resonance is not strongly coupled to the extensional resonance and can be ignored in calculation of the transducer response as will be shown. A simple one-dimensional theory can be derived and used directly in the transducer transmission line model with good success. Using the notation of Auld,[35] the piezoelectric constitutive relations can be written in the form

$$T = -\tilde{e} \cdot E + c^E : S \tag{3-1}$$

$$D = \varepsilon^S \cdot E + e : S \tag{3-2}$$

where the bars denoting vector and tensor quantities have been dropped for brevity. The stress is denoted by T_I in reduced coordinates, the strain by S_I, the electric field by E_I, and the electric displacement by D_I. The piezoelectric stress matrix is denoted by e_{IJ} in reduced coordinates, and $\tilde{e}_{IJ} = e_{IJ}$ is the transpose of this matrix. The stiffness matrix at constant E is denoted by C^E_{IJ}, and the permittivity at constant stress by ε^S_{IJ}. For a uniaxial piezoelectric ceramic like PZT-5A, which is isotropic in the plane transverse to the poling axis, the stiffness, piezoelectric stress constant, and permittivity matrices are given as follows:

$$(C^E_{IJ}) = \begin{pmatrix} C^E_{11} & C^E_{13} & C^E_{13} & 0 & 0 & 0 \\ C^E_{13} & C^E_{11} & C^E_{13} & 0 & 0 & 0 \\ C^E_{13} & C^E_{13} & C^E_{33} & 0 & 0 & 0 \\ 0 & 0 & 0 & C^E_{44} & 0 & 0 \\ 0 & 0 & 0 & 0 & C^E_{44} & 0 \\ 0 & 0 & 0 & 0 & 0 & C^E_{66} \end{pmatrix} \tag{3-3}$$

$$(e_{iJ}) = \begin{pmatrix} 0 & 0 & 0 & 0 & e_{x5} & 0 \\ 0 & 0 & 0 & e_{x5} & & \\ e_{z1} & e_{z1} & e_{z3} & 0 & 0 & 0 \end{pmatrix} \quad (3\text{-}4)$$

$$(\varepsilon^S_{ij}) = \begin{pmatrix} \varepsilon^S_{xx} & 0 & 0 \\ 0 & \varepsilon^S_{xx} & 0 \\ 0 & 0 & \varepsilon^S_{zz} \end{pmatrix} \quad (3\text{-}5)$$

In the nonpiezoelectric case, $e_{iJ} \equiv 0$, and if $S_2(x,z) \equiv 0$ for a long slotted element, and there are no shear strains, the relevant stress-strain relations are simply

$$\begin{aligned} T_1 &= C^E_{11}S_1 + C^E_{13}S_3 \\ T_3 &= C^E_{13}S_1 + C^E_{33}S_3 \end{aligned} \quad (3\text{-}6)$$

Now if the width (L) is small compared to the height (H), it can be assumed that there is no longitudinal stress in the x-direction, or $T_1(x,z) \equiv 0$. Therefore,

$$S_1 = -\frac{C^E_{13}}{C^E_{11}} S_3 \quad (3\text{-}7)$$

and

$$T_3 = C^E_{33}S_3 \quad (3\text{-}8)$$

where

$$C'^{E}_{33} = C^{E}_{33}\left(1 - \frac{(C^{E}_{13})^2}{C^{E}_{11}C^{E}_{33}}\right) \tag{3-9}$$

The same boundary condition can be applied in the piezoelectric case where open circuit conditions are also assumed so that $D_z(x,z) \equiv 0$. From Eqs. (3-1) and (3-2), the relevant relations are

$$T_1 = C^{E}_{11}S_1 + C^{E}_{13}S_3 - e_{z1}E_z \tag{3-10}$$

$$T_3 = C^{E}_{13}S_1 + C^{E}_{33}S_3 - e_{z3}E_z \tag{3-11}$$

$$D_z = \epsilon^{S}_{zz}E_z + e_{z1}S_1 + e_{z3}S_3 \quad . \tag{3-12}$$

Letting $T_1(x,z) \equiv 0$ in Eq. (3-10), S_1 can be expressed in terms of S_3 and E_z and substituted into Eqs. (3-11) and (3-12) as follows:

$$T_3 = C'^{E}_{33}S_3 - e'_{z3}E_z \tag{3-13}$$

$$D_z = \epsilon'^{S}_{zz}E_z + e'_{z3}S_3 \tag{3-14}$$

where

$$e'_{z3} = e_{z3} - \frac{e_{z1}C^{E}_{13}}{C^{E}_{11}} \tag{3-15}$$

and

$$\epsilon'^{S}_{zz} = \epsilon^{S}_{zz} + \frac{e^2_{z1}}{C^{E}_{11}} \quad . \tag{3-16}$$

Equations (3-13) and (3-14) are identical in form to those of a thin disc transducer with the modified constants defined in (3-9), (3-15), and (3-16). Therefore, all the results for the thin disc transducer[36] can be applied to the case of the narrow slotted transducer including quarter-wave matching and backing schemes using these modified constants, with other considerations to be discussed in detail later.

Other parameters of interest are derived below. The modified parameters are derived as follows, taking open circuit conditions or $D_z(x,z) = 0$ in Eq. (3-14):

$$E_z = -\frac{e'_{z3}}{\epsilon'^{S}_{zz}} S_3 \tag{3-17}$$

$$T_3 = C'^{E}_{33}\left[1 + \frac{e'^{2}_{z3}}{C'^{E}_{33}\,\epsilon'^{S}_{zz}}\right] S_3 \tag{3-18}$$

Therefore, the stiffened elastic constant is

$$C'^{D}_{33} = C'^{E}_{33}\,(1 + K'^{2}) \tag{3-19}$$

where

$$K'^{2} = \frac{e'^{2}_{z3}}{C'^{E}_{33}\,\epsilon'^{S}_{zz}} \tag{3-20}$$

Since the constant K'^{2} appears in the functional form of the one-dimensional transducer input impedance in the form $K'^{2}/(1+K'^{2})$,[36] it is convenient to introduce a simplified constant k'^{2}_{33}, where

$$k'^{2}_{33} = \frac{K'^{2}}{1 + K'^{2}} \quad . \tag{3-21}$$

This coupling constant is labeled k'^2_{33} instead of k'^2_t since it is more closely related to the length extensional resonance of a thin rod than to the thickness extensional resonance of a thin plate. The stiffened velocity and acoustic impedance of the transducer can be defined then as follows:

$$\bar{v}'_D = \left(\frac{c'^D_{33}}{\rho}\right)^{1/2} \tag{3-22}$$

$$\bar{Z}'_D = \bar{v}'_D \rho \quad . \tag{3-23}$$

Various parameters for PZT-5A and PZT-5H are tabulated in Table 3-2 using the data published by Jaffe and Berlincourt.[37] These materials have been chosen since they have high coupling coefficients and high dielectric constants.

The high coupling coefficient is desired for the same reasons as discussed in Chapter II; that is, broad bandwidth with high efficiency. The high dielectric constant is most important for small transducer elements in order to keep the electrical impedance as low as possible and so making electrical matching simpler. All the arrays reported in this work were constructed of PZT-5A or its equivalent, depending on the manufacturer. PZT-5A has a smaller aging coefficient than PZT-5H and a much higher Curie temperature, making it easier to work with than PZT-5H.

The most significant aspect of the changes in the transducer parameters produced by slotting is the approximate doubling of the electromechanical coupling coefficient, k'^2_t. The coupling constant for the narrow, long element, k'^2_{33}, is close in value to k^2_{33}, the length extensional coupling constant of a thin rod, as seen in Table 3-2. This doubling occurs mostly since c'^E_{33} is decreased to about one-half the unslotted value.

TABLE 3-2

PARAMETER	PZT-5A		PZT-5H	
	Thin disc	Slotted	Thin disc	Slotted
c_{11}^E	$11.1(10)^{10}$	---	$12.6(10)^{10}$	---
c_{13}^E	$8.0(10)^{10}$	---	$8.4(10)^{10}$	---
c_{33}^E (N/m^2)	$11.1(10)^{10}$	$5.84(10)^{10}$	$11.7(10)^{10}$	$6.09(10)^{10}$
c_{33}^D (N/m^2)	$14.7(10)^{10}$	$10.8(10)^{10}$	$15.7(10)^{10}$	$11.8(10)^{10}$
$\bar{v}_a$ (m/s)	$4.35(10)^3$	$3.78(10)^3$	$4.56(10)^3$	$3.97(10)^3$
ρ(kg/m^3)	7.75	7.75	7.5	7.5
$\bar{Z}_a$ (kg/m^2-s)	33.7	29.3	34.2	29.7
e_{z3} (C/m^2)	15.8	19.4	23.3	27.6
$\epsilon_{zz}^S/\epsilon_0$	830	857	1470	1508
$k_T^2, k_{33}'^2$	0.240	0.47	0.255	0.48
k_{33}^2 (rod)	---	0.50	---	0.56

Doubling k_T^2 effectively halves the electrical Q of a series tuned transducer, making the design of low-loss broad-bandwidth elements a simpler task.

In addition to the large increase in k_T^2, it can be seen that there is about a 14% decrease in the velocity and impedance of the PZT materials and a slight increase in the effective dielectric constant. These changes have little overall effect in the design of transducers except that the thickness of the material must be reduced by 14% over that of an unslotted material with the same center frequency. The effect of this thickness change on the configuration ratio G(= L/H) should not be overlooked, however, for reasons shown in the next section. These effective parameters are used in the transducer model with good results to predict the response of slotted transducer elements reported later in this chapter.

C. COUPLING TO LATERAL MODE

A simple theory describing the coupling between the two dilatational modes of a piezoelectric resonator as illustrated in Fig. 3-1 has been carried out by Onoe and Tiersten[34] for the short-circuited case. This approach is easily adapted to the open-circuited case which then can be applied to the simple one-dimensional transducer model. This theory models the element as two one degree-of-freedom systems coupled through a single mechanism. This coupling theory was originally applied to elastic vibration theory by Gliebe and Blechschmidt,[38] where the infinite number of degrees of freedom of a continuous body can be well approximated by suitably choosing a finite number coupled together. For

two degrees of freedom coupled through a single constant mechanism, a biquadratic frequency equation is easily obtained,

$$(f_a^2 - f^2)(f_b^2 - f^2) = \Gamma^2 f_a^2 f_b^2 \quad , \tag{3-24}$$

where f_a and f_b are the eigenfrequencies of the uncoupled system and Γ is a dimensionless constant coupling coefficient. This equation is plotted on Fig. 3-3 on a log (fH) versus log G(G=L/H) coordinate system. The dashed lines give the uncoupled resonant frequencies, and the solid line the coupled frequencies. Following the arguments of Once and Tiersten, a simple way of determining the coupling coefficient Γ consists of selecting Γ to yield the known frequencies at the endpoints of the frequency curves for large and small values of G. In the nonpiezoelectric case,

$$f_a = \frac{1}{2L}\sqrt{c_{11}/\rho} \tag{3-25}$$

$$f_b = \frac{1}{2H}\sqrt{c_{33}/\rho} \tag{3-26}$$

These frequencies correspond to dilatational modes of large area plates. Therefore, $f_a/f_b = 1/G(C_{11}/C_{33})^{1/2}$. Substituting this result into Eq. (3-24) and taking the limits as G approaches 0 and ∞, one finds that $f_d = f_a\sqrt{(1 - \Gamma^2)}$ and $f_c = f_a\sqrt{(1 - \Gamma^2)}$. For internal consistency then, this coupling theory can only be applied if

$$f_c/f_a = f_d/f_b \tag{3-27}$$

The regions near f_c and f_d correspond to length longitudinal modes of a long thin plate. These frequencies are easily obtained, from Eq. (3-9) for f_d, and from a similar calculation for f_c. These frequencies are

$$f_c = \frac{1}{2L}\sqrt{\left[\frac{C_{11}}{\rho}\left(1 - \frac{C_{13}^2}{C_{11}C_{33}}\right)\right]} \tag{3-28}$$

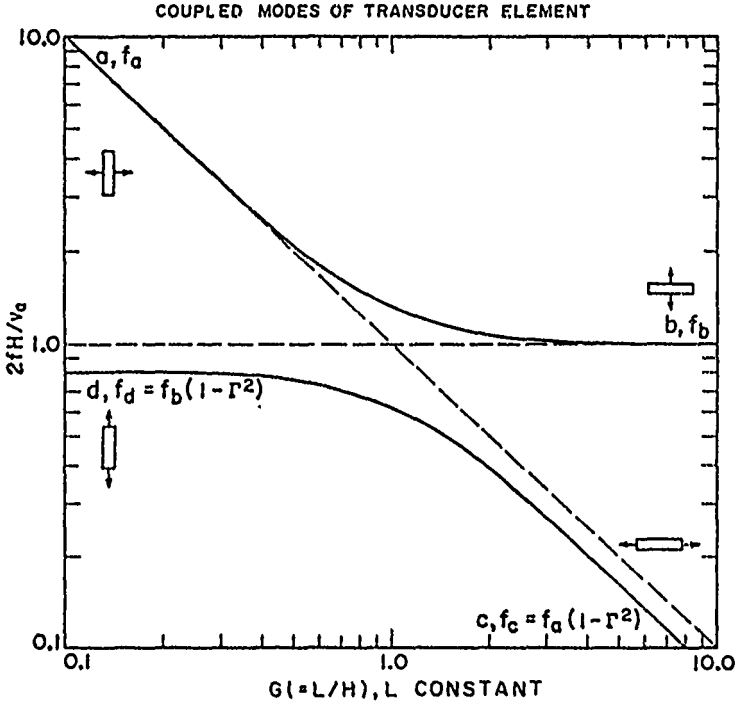

FIG. 3-3. Generalized coupled mode dispersion curves showing limiting cases.

and

$$f_d = \frac{1}{2H}\sqrt{\left[\frac{C_{33}}{\rho}\left(1 - \frac{C_{13}^2}{C_{11}C_{33}}\right)\right]} \quad . \tag{3-29}$$

Therefore,

$$\frac{f_c}{f_a} = \frac{f_d}{f_b} = \sqrt{\left[1 - (C_{13}^2/C_{11}C_{33})\right]}, \tag{3-30}$$

and

$$\Gamma^2 = C_{13}^2/C_{11}C_{33} \quad . \tag{3-31}$$

For isotropic materials, $C_{11} = C_{33}$, and $\Gamma = C_{12}/C_{11}$ or

$$\Gamma = \frac{\sigma}{1-\sigma} \tag{3-32}$$

where σ is Poisson's ratio. As is pointed out in reference 34, the lower branch gives excellent agreement with experiment, but the upper branch gives much poorer agreement because of coupling to additional independent modes which exist in this frequency range. The frequency variation of the lower mode with $G = L/H$ for isotropic materials is shown in Fig. 3-4 for various values of σ.

The open circuited limiting frequencies for a piezoelectric resonator are now derived. In region b, the limiting frequency is the well-known thickness dilatational mode of a thin disc resonator, so

$$f_b = \frac{1}{2H}\sqrt{\frac{C_{33}^D}{\rho}} \tag{3-33}$$

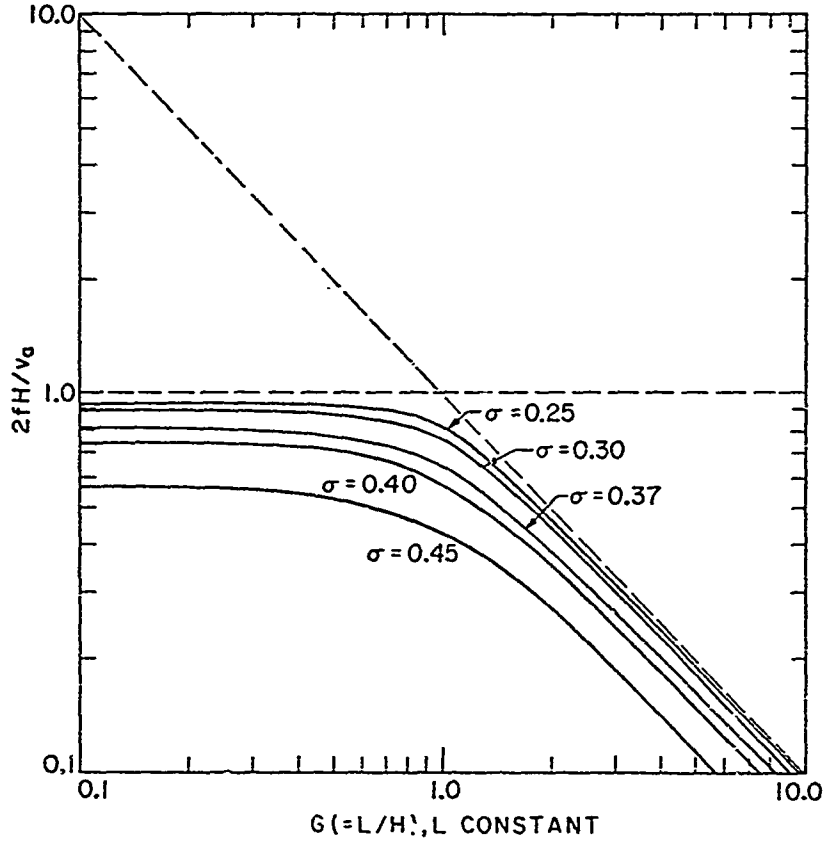

FIG. 3-4. Lower branches of coupled mode dispersion relation for isotropic rectangular resonators for varying values of Poisson's ratio.

where

$$C_{33}^{D} = C_{33}^{E}\left[1 + (e_{z3}^{2}/\epsilon_{zz}^{S}C_{33}^{E})\right] \tag{3-34}$$

In region d , the limiting frequency is that of the extensional mode calculated in the previous section where

$$f_d = \frac{1}{2H}\sqrt{\frac{C_{33}'^{D}}{\rho}} \tag{3-35}$$

and $C_{33}'^{D}$ is defined in Eq. (3-19).

In region a , the limiting frequency is that of the lateral thickness dilatational mode. With a similar derivation that led to Eq. (3-33), the frequency is easily obtained from Eqs. (3-10) through (3-12), assuming $S_3 = 0$. Therefore

$$f_a = \frac{1}{2L}\sqrt{\frac{C_1^{D}}{\rho}} \tag{3-36}$$

where

$$C_{11}^{D} = C_{11}^{E}\left[1 + (e_{z1}^{2}/\epsilon_{zz}^{S}C_{11}^{E})\right] \quad . \tag{3-37}$$

In region C , the limiting frequency is that of a lateral extensional mode analogous to f_d where

$$f_C = \frac{1}{2L}\sqrt{\frac{C_{11}'^{D}}{\rho}} \tag{3-38}$$

where

$$C_{11}'^{D} = C_{11}'^{E}\left(1 + \frac{e_{z1}'^{2}}{\epsilon_{zz}'^{S}C_{11}'^{E}}\right) \quad , \tag{3-39}$$

$$e_{z1}' = e_{z1} - (e_{z3}C_{13}^{E}/C_{33}^{E}) \quad , \tag{3-40}$$

$$c'^{E}_{11} = c^{E}_{11} - (c^{E2}_{13}/c^{E}_{33}) \quad . \tag{3-41}$$

and

$$c'^{S}_{zz} = \epsilon^{S}_{zz} + e^{2}_{z3}/c^{E}_{33} \quad . \tag{3-42}$$

For internal consistency, the relation $f_a/f_c = f_b/f_d$ should be satisfied. It follows directly from (3-33), (3-35), (3-36), and (3-38) that f_a/f_c is algebraically identical to f_b/f_d so that internal consistency is satisfied. Substituting the parameters for PZT-5A and PZT-5H, $f_a/f_c = 1.16$ in both cases.

To determine the coupling constant k^2, the ratio f_d/f_b must be cast into the form

$$f_d/f_b = (1 - k^2)^{1/2} \quad . \tag{3-43}$$

From (3-33) and (3-35), it is easily shown that

$$f_d/f_b = \left[\left(1 - \frac{c^{E2}_{13}}{c^{E}_{11} c^{E}_{33}}\right)\left(\frac{1 - k_t^2}{1 - k_{33}^2}\right)\right]^{1/2} \tag{3-44}$$

Substituting the parameters for PZT-5A, k^2 is found to be 0.257 for the open circuited case. A plot of both branches of the frequency spectrum for both the open-circuited and short-circuited[34] cases is shown in Fig. 3-5. From the figure, it can be seen that there is only a 9.3% frequency shift from the open-circuited extensional mode for a configuration ratio $G = 0.7$ and a 5% shift for $G = 0.5$. Note that the theoretical curves are for the case of the resonator with free boundaries.

An important problem in designing elements where G is close to one is the emergence of the undamped mode close to the desired passband

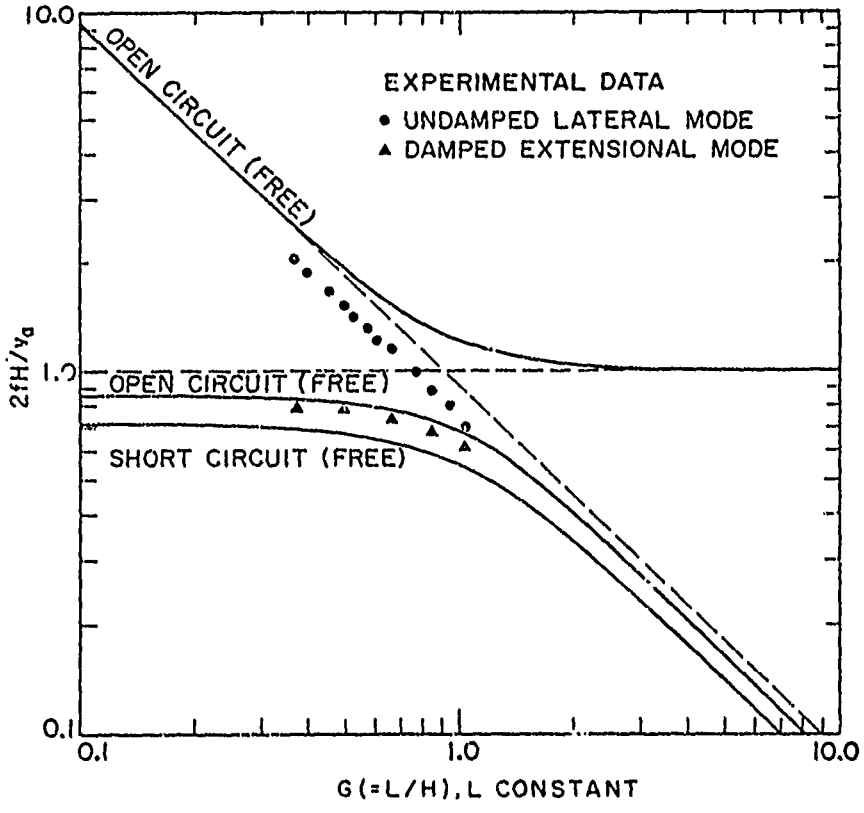

FIG. 3-5. Experimental and theoretical dispersion curves for slotted array elements.

of the transducer element. This mode is clearly seen in Fig. 3-6 where the measured real part of the electrical input impedance of lead-backed (Z = 22) PZT-5A transducer elements of varying configuration ratio is shown. As the configuration ratio approaches unity, this undamped lateral mode, characterized by the sharp peak in the curves, moves into the passband of the element and decreases the bandwidth. The experimentally measured frequencies for lead-backed elements with the G ratio between 0.37 and 1.03 are shown in Fig. 3-5. Note that the experimental data are for elements damped with a high impedance backing while the theory is for elements with free boundaries only. The lateral mode frequencies are about 23% lower than that of the lateral extensional mode defined in Eq. (3-36), probably due to coupling to higher order modes. The extensional mode frequencies are slightly less than the open-circuit frequencies calculated for an element with free boundaries. The downshift in these frequencies when one side of the element is heavily backed is expected from the one-dimensional transducer model.

These data show that the configuration ratio should be 0.5 or less so that the undamped lateral mode frequency is at least an octave higher than the center frequency of the passband. At this point, there is little coupling between the modes, and the undesired mode can be easily filtered out if desired. Near G = 0.65 , coupling between the modes begins to limit the bandwidth of the transducer element as seen in Fig. 3-6.

D. EFFECTIVE ACOUSTIC LOAD IMPEDANCE OF A NARROW ELEMENT

A transducer array element radiating into a semi-infinite loading or backing medium excites waves in all directions in these media. If the element is narrow enough, the power radiated into waves propagating

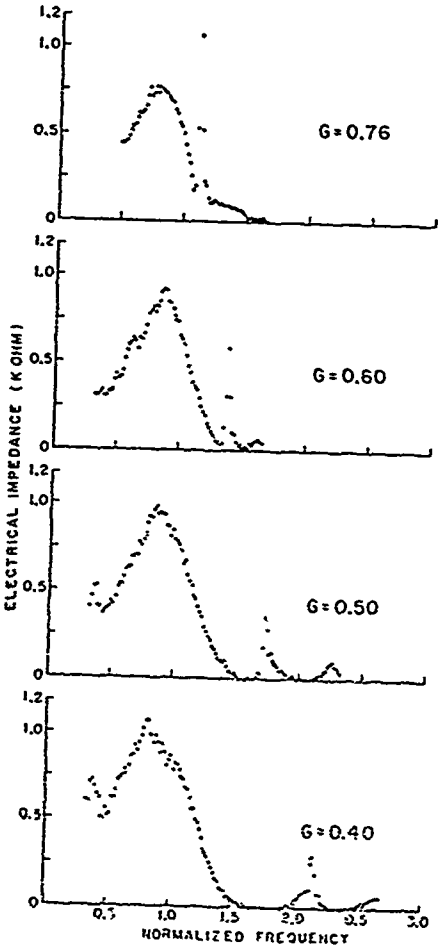

FIG. 3-6. Real part of experimental electrical impedance of lead-backed PZT-5A elements 0.0635 cm thick × 1.27 cm long for varying values of configuration ratio. Data taken with computer-controlled HP 4865 Vector Impedance meter.

at an angle to the normal becomes large enough so that the plane wave longitudinal mode impedance no longer adequately describes the load impedance seen by the element. A variational theory is developed in this section to calculate the effective load impedance of the element at the interface taking into account the longitudinal, shear, and Rayleigh waves excited, as illustrated in Fig. 3-7.

This problem is analogous to the evaluation of the radiation impedance of an electromagnetic waveguide radiating into a semi-infinite half-space. A treatment of this problem is presented in Harrington[39] for a two-dimensional parallel-plate waveguide for the two cases where the incident wave is either the TEM mode or the dominant TE mode. Harrington does not try to generate a variational expression for this radiation impedance, but the final form of his impedance integral is achieved in a similar manner to the one presented here, that is, from the complex power flow at the interface between the waveguide and load medium. The difference in the two expressions lies in the normalization of the integral. Harrington uses a heuristic approach to force the dimensionality of the impedance expression to be correct. The normalization shown in this paper is a natural result of the variational theory. Nevertheless, it is interesting to note that the aperture admittance calculated in reference 39 is capacitive in the case where the assumed field is taken to be uniform over the aperture and inductive when the assumed field has a cosine dependence. As will be shown later, the effective load impedance of a transducer element is capacitive when the load is a solid and is inductive when the load is a liquid. This occurs since a liquid cannot support shear waves and the assumed normal stress field at the element-liquid interface

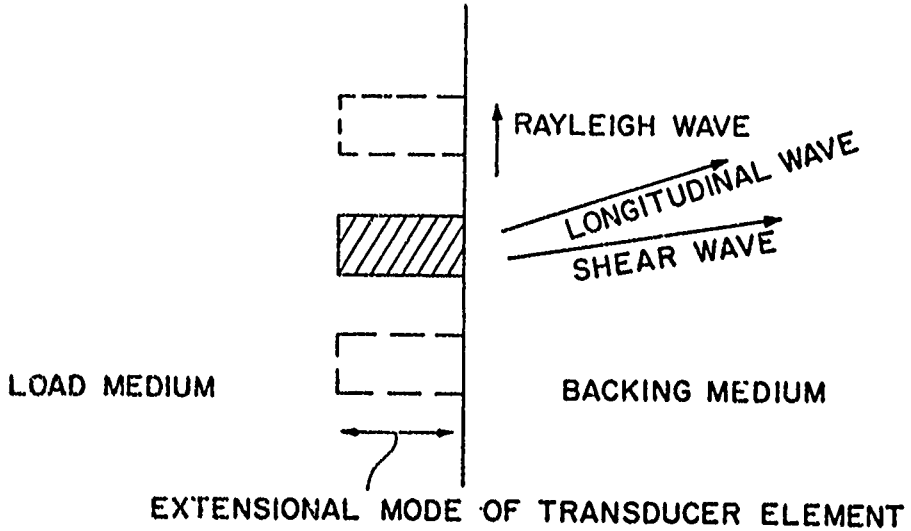

FIG. 3-7. Schematic drawing of model used to calculate effective backing impedance of finite width transducer element.

must be zero at the edges of the element to prevent the integral expression for the admittance from going to a logarithmic infinity. As the Poisson's ratio for a solid approached 0.5 (that is, a liquid), the effective admittance becomes more inductive and approaches the liquid case, as will be shown.

A similar but also nonvariational calculation for acoustic radiators of varying configuration ratio was carried out by Miller and Pursey[40] for the case when the radiator is terminated by a semi-infinite solid. The approach used in reference 40 is identical to that found in reference 39, and the expression calculated is very close to the variational expression derived in this paper for solids. Again, the difference is in the normalization integral. Points of divergence between the two theories will be shown as the variational theory is presented. The Green's function in the load medium is calculated in all the derivations, and the resulting integrals numerically evaluated. Due to the lack of digital computers when the Miller-Pursey paper was written, only a few values of the effective impedance were calculated as a function of βL where β is the wavenumber and L the width of the radiator. A variational expression for the effective admittance is derived below.

If the element is regarded as a section of waveguide, the acoustic fields in the guide can be described by a normal mode expansion. Following Auld's development for reflection-symmetric waveguides[41] and neglecting piezoelectricity, vector functions can be introduced analogous to the equivalent "voltage" and "current" parts of the fields for the m^{th} mode. For guides infinite in length in the y-direction (Fig. 3-8),

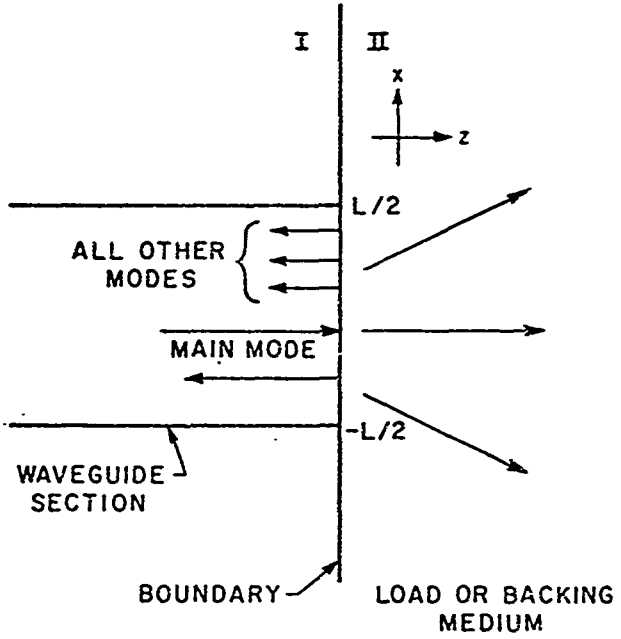

FIG. 3-8. Schematic drawing of waveguide model of transducer element used to calculate variational form of effective load impedance.

the "voltage part of the field is described by the vectors

$$\bar{G}_M(x,z) = \begin{bmatrix} V_{Mx}(x,z) \\ 0 \\ T_{M3}(x,z) \end{bmatrix} \tag{3-45}$$

and the "curre. " part by

$$\bar{Q}_M(x,z) = \begin{bmatrix} T_{M5}(x,z) \\ 0 \\ V_{Mz}(x,z) \end{bmatrix} \tag{3-46}$$

These fields can be separated into a product of the "voltage" or "current" amplitude with a vector mode function, that is,

$$\begin{aligned} \bar{G}_M &= V_M(z)\ \bar{e}_M(x) \\ \bar{Q}_M &= I_M(z)\ \bar{q}_M(x) \end{aligned} \tag{3-47}$$

where the $\bar{e}_M$'s and $\bar{q}_M$'s are orthogonal and satisfy

$$\int \bar{q}_M \cdot \bar{e}_M^* \, dS = -1 \tag{3-48}$$

The impedance of a given mode is defined to be

$$\frac{V_M}{I_M} = Z_{M0} = \frac{\omega}{\beta_M}$$

for waves propagating in the forward direction.

In considering the transducer element as a section of waveguide, it is assumed that primarily a single mode is excited and is incident from the left upon the boundary between regions I and II in Fig. 3-8. The reflected wave from this boundary is assumed to be composed of all allowable modes in the waveguide. The symmetry of the structure limits the allowable modes to the symmetric Lamb wave family. It is desired to calculate the impedance of the lowest order mode, Z_1, at the boundary plane in Fig. 3-7. Since the other modes excited in the guide are all reflected waves, their impedances are taken to be $Z_{M\neq 1} = -Z_{M0}$, the modal impedances for backward traveling waves. Therefore the total "current" can be written

$$\bar{Q} = \sum_M \bar{Q}_M = \frac{V_1}{Z_1}\bar{q}_1 - \sum_2^{\infty} \frac{V_M}{Z_{M0}}\bar{q} \quad . \tag{3-49}$$

The voltage amplitudes can be determined using Eqs. (3-47) and (3-48),

$$V_M = -\int \bar{G} \cdot \bar{q}_M^* \, dS \quad . \tag{3-50}$$

Combining (3-50) and (3-49) we find that

$$\bar{Q} = -\frac{\bar{q}_1}{Z_1}\int \bar{G} \cdot \bar{q}_1^* \, dS + \sum_2 \frac{\bar{q}_M}{Z_{M0}} \int \bar{G} \cdot \bar{q}_M^* \, dS \tag{3-51}$$

Now the complex power flow in region I is

$$P = -\frac{1}{2}\int (\bar{G} \cdot \bar{Q}^*) \, dS \Big|_I$$

$$= \frac{1}{2Z_1^*}\int \bar{G} \cdot \bar{q}_1^* \, dS \int \bar{G}^* \cdot \bar{q}_1 \, dS - \sum_2 \frac{1}{2Z_{M0}^*} \int \bar{G} \cdot \bar{q}_M^* \, dS \int \bar{G}^* \cdot q_M \, dS \quad . \tag{3-52}$$

From the continuity of power flow through the boundary,

$$-\frac{1}{2}\int \bar{G} \cdot \bar{Q}^* \, dS\Big|_I = -\frac{1}{2}\int \bar{G} \cdot \bar{Q}^* \, dS\Big|_{II} \quad . \tag{3-53}$$

If we now assume in region I that the mode excited is the extensional mode previously described which is similar in form to the L_1 Lamb wave mode in an isotropic plate, one can assume that

$$\bar{G}_1 = \begin{bmatrix} 0 \\ 0 \\ T_{13} \end{bmatrix} \quad , \quad \bar{Q}_1 = \begin{bmatrix} 0 \\ 0 \\ v_{1z} \end{bmatrix} \tag{3-54}$$

where the assumption is most accurate near $\beta = 0$. Therefore, $(\bar{G} \cdot \bar{q}_1^*)_I = (T_3 q_1^*)_I$.

If we now assume that $T_5 = 0$ at the boundary, $(\bar{G} \cdot \bar{Q}^*) = T_3 v_z^*$. This assumption is based on the grounds that the element is narrow and vibrating with a simple piston-like motion with very small shear stresses. Therefore, (3-52) and (3-53) can be written

$$\int T_3 \, v_z^* \, dx\Big|_{II} = -\frac{1}{Z_1^*}\int T_3 q_1^* dx \int T_3^* q_1 dx + \sum_2 \frac{1}{Z_{M0}^*}\int \bar{G} \cdot \bar{q}_M^* \, dx \int \bar{G}^* \cdot \bar{q}_M dx \quad . \tag{3-55}$$

where we assume unit length along the y direction.

The electromagnetic equivalent of the left-hand side of Eq. (3-55) is used as the starting point for the impedance calculation of Harrington. However, the differences arise in the right-hand side. Harrington takes the RHS simply as $|V|^2/Z$. For the TEM mode, he chooses $V = 1$ and for

the TE mode $V = L$, where L is the width of the transducer. The functional form of radiation impedance, determined from the LHS, will be correct, but the normalization is arbitrary. Miller and Pursey, on the other hand, express the particle displacement fields $u_z(\beta)$ in region II in terms of the stress field as a function of β, the x-component of the longitudinal wavenumber. Assuming a form of the stress field at the boundary, $u_z(x)$ is then obtained by inverse transforming $u_z(\beta)$. The average displacement field $\bar{u}_z$ is obtained by integrating along the boundary. The radiation impedance is then expressed as $Z = -1/i\omega\bar{u}_z$ where $T_3(x) = 1$ for $|x| < L/2$. This impedance expression reduces to the same result as the variational form shown below only for the case where the assumed field $T_3(x)$ is uniform across the transducer element. Otherwise, the normalization is different.

Expressing $v_z|_{II}$ in terms of a Green's function, one can write

$$v_z(x)|_{II} = \int T_3(x')\mathcal{G}(x,x')\,dx' \tag{3-56}$$

where $\mathcal{G}(x,x')$ is a Green's function to be determined. Combining (3-55) and (3-56), an expression for Z_1 is determined:

$$\frac{1}{Z_1} = \frac{-\iint T_3^*(x)\ \mathcal{G}(x,x')\ T_3(x')dxdx' + \sum_{\bar{2}} \frac{1}{Z_{M0}} \int \bar{G}\cdot\bar{q}_M^*\,dx \int \bar{G}^*\cdot\bar{q}_M\,dx}{\int T_3 q_1^*\,dx \int T_3^* q_1\,dx} \tag{3-57}$$

If the higher order modes are ignored, Eq. (3-57) is reduced to the following expression for the admittance:

$$Y_1 = \frac{-\iint T_3^*(x)\ \mathcal{G}(x,x')\ T_3(x')dxdx'}{\int T_3 q_1^*dx \int T_3^* q_1 dx} \tag{3-58}$$

It is shown in Appendix A that Eq. (3-58) is variational in form with respect to the form of the assumed normal stress T_3.

Equation (3-58) can also be written in the form

$$Y_1 = \frac{-\iint T_3^*(x)\, v_z(x)\, dx}{\int T_3 q_1^*\, dx \int T_3^* q_1\, dx} \quad . \tag{3-59}$$

The Green's function can be determined then by Fourier transforming the numerator of (3-59) so that Y_1 is now written

$$Y_1 = \frac{-\iint T_3^*(\beta)\, v_z(\beta)\, d\beta}{2\pi \int T_3 q_1^* dx \int T_3^* q_1\, dx} \tag{3-60}$$

Now by assuming a functional form of $T_3(x)$ satisfying the field equations, an estimate of Y_1 can be found correct to second order.

The form of $v_z(\beta)$ in terms of $T_3(\beta)$ was derived by Miller and Pursey for four types of radiating sources: (a) an infinitely long strip of finite width vibrating normally to the medium surface; (b) the same long strip vibrating tangentially to the medium surface and normally to the strip axis; (c) a circular disc of finite radius vibrating normally to the surface medium; (d) a torsional radiator in the form of a circular disc of finite radius performing rotational oscillations about its center. Case (a) is identical to the one evaluated in this paper. The integrals in reference 40 were evaluated by hand for six values of βd. The form of $v_z(\beta)$ is derived in Appendix B for isotropic solids [Eq. (B-15)] and for liquids [Eq. (B-17)]. Substituting (B-15) into (3-60), one

obtains the result

$$Y_1 = \frac{\int_{-\infty}^{\infty} \left(\frac{\omega\beta_l}{\mu}\right) \frac{\beta^2 + \beta_s^2}{\left[(\beta_s^2 - \beta^2)^2 + 4\beta_s\beta_l\beta^2\right]} |T_3(\beta)|^2 d\beta}{2\pi \int T_3 q_1^* \, dx \int T_3^* q_1 \, dx} \tag{3-61}$$

where the parameters are defined in the appendix.

A simple form of the trial field $T_3(x)$ is assumed which is uniform with x across the transducer so that

$$T_3(x) = \begin{cases} T_0 & , \quad |x| < L/2 \\ 0 & , \quad |x| \geq L/2 \end{cases} \tag{3-62}$$

where L is the width of the element. The modal field $q_1(x)$ is also uniform so that the normalized form is

$$q_1(x) = \begin{cases} 1/\sqrt{d} & , \quad |x| < L/2 \\ 0 & , \quad |x| \geq L/2 \end{cases} \tag{3-63}$$

Fourier transforming (3-62), one obtains the result

$$T_3(\beta) = T_0 d \frac{\sin(\beta L/2)}{(\beta L/2)} \tag{3-64}$$

and

$$Y_1 = \frac{\omega d}{2\pi\mu} \int_{-\infty}^{\infty} \frac{\beta_l k_s^2}{\left[(\beta_s^2 - \beta^2)^2 + 4\beta_s\beta_l\beta^2\right]} \left(\frac{\sin(\beta L/2)}{(\beta L/2)}\right)^2 d\beta \; .$$

Equation (3-64) is evaluated in Appendix C. The method of integrating the expression follows that of Miller and Pursey and involves integrating along the real axis of the complex β plane and taking into account branch cuts at the longitudinal and shear wave cutoffs and the Rayleigh pole.

The normalized load impedance for a slotted element calculated in Appendix C is shown in Fig. 3-9 as a function of $(k_1 L)$ for various values of Poisson's ratio. For $(k_1 L) > 1$, the impedance is essentially real and oscillates slowly about the longitudinal plane wave impedance. Below $(k_1 L) = 1$, the reactive part increases in value rapidly so that the impedance becomes mainly capacitive. Since the assumed stress field $T_3(x)$ was taken to be uniform, the impedance calculated here is identical to that of Miller and Pursey at the six values of $k_1 L$ they evaluated. This complex-valued impedance was used as the backing impedance in the standard program which computes the electrical impedance and insertion loss of transducers, using the modified transducer constants for the extensional mode. As shown in the next section, the change in this impedance, due to finite width, has little effect on the transducer elements of the widths used in the arrays reported in this thesis, but must be accounted for in narrower elements where $k_1 L \ll 1$.

For the case where the load medium is water, a similar calculation can be carried out by taking into account that there are no radiated shear or Rayleigh waves in a liquid. Substituting Eq. (B-17) from Appendix B into (3-60), one obtains the following expression for the

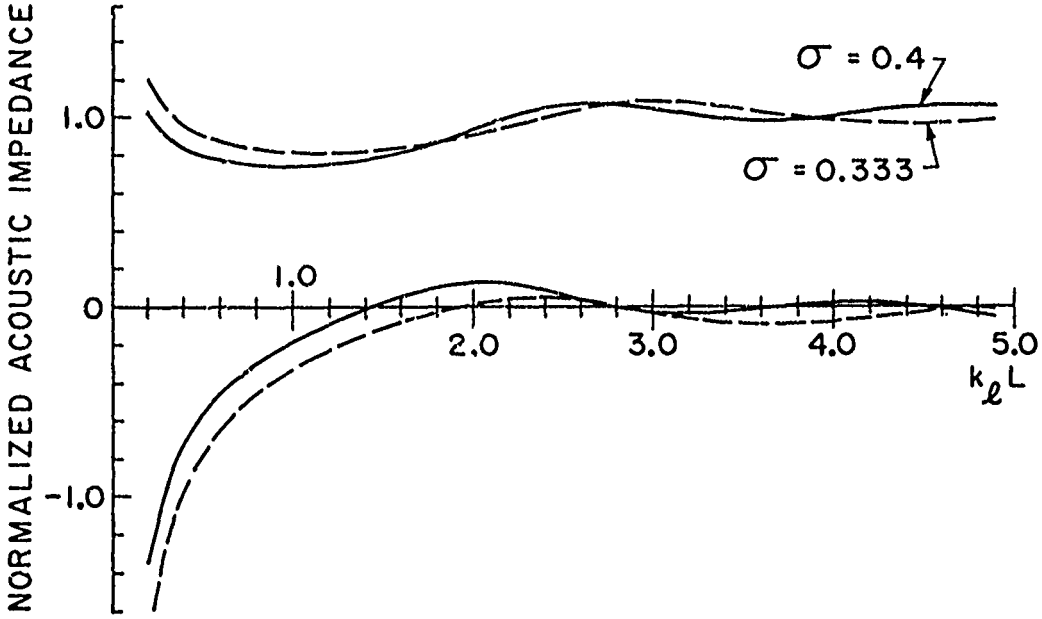

FIG. 3-9. Normalized effective acoustic impedance seen by finite width radiator for two values of backing Poisson's ratio.

admittance:

$$Y_1 = \frac{\int_{-\infty}^{\infty} \left(\frac{\omega\beta_1}{2k_1^2}\right) |T_3(\beta)|^2 d\beta}{2\pi \int T_3^* q_1 dx \int T_3 q_1^* dx} \qquad (3\text{-}65)$$

If one now assumes that T_3 is uniform across the element as before and q_1 is the same uniform mode with $\xi = \beta/k_1$, the integrand in the numerator of (3-65) varies as

$$\sqrt{1 - \xi^2} \left(\frac{\sin(k_1 L/2)\xi}{(k_1 L/2)}\right)^2$$

which has a $1/\xi$ dependence as ξ gets large. This is a logarithmic infinity causing the integral to diverge. This divergence is a result of the discontinuity in stress at $|x| = L/2$ in the assumed field. Physically, since the liquid cannot support shear waves, there can be no discontinuity in stress at the boundary. Removing the discontinuities removes the divergence problem. A series of assumed fields that does this is:

$$T_3(x) = \begin{cases} T_0(1 - (2x/L)^n) & , \quad |x| < L/2 \\ 0 & , \quad |x| \geq L/2 \end{cases} \qquad (3\text{-}66)$$

where n is an even integer. Where n is large, T_3 is nearly uniform except at the endpoints. This field is then very much like the dilatational mode in the transducer element. The impedances calculated

with these various assumed fields are nearly identical, attesting to the variational nature of (3-65).

Fourier transforming (3-66) yields the result

$$T_3(\beta) = T_0 d \sum_{j=2}^{n,2} \frac{n!(-1)^{j/2}}{(n-j+1)!} \frac{\cos(\beta L/2)}{(\beta L/2)^j} + \frac{n!}{(n-j)!} (-1)^{j/2+1} \frac{\sin(\beta L/2)}{(\beta L/2)^{j+1}}$$

(3-67)

Substituting (3-66) and (3-67) into (3-65) and noting $\omega/\lambda = k_\ell/Z_\ell$, an expression for the admittance is obtained as before. For the case where $n = 2$, this expression is

$$Y_1 = \frac{9}{8\pi} \frac{k_\ell L}{Z_\ell} \int \sqrt{1-\xi^2} \left(\frac{16 \sin(k_\ell L \xi/2)}{(k_\ell L \xi)^3} - \frac{8 \cos(k_\ell L \xi/2)}{(k_\ell L \xi)^2} \right)^2 d\xi$$

(3-68)

where $\xi = \beta/k_\ell$.

As before, there is a branch point at $\xi = 1$ corresponding to the cutoff of longitudinal waves. For $\xi < 1$, the admittance is entirely real. For $\xi > 1$, the admittance is entirely imaginary corresponding to evanescent longitudinal waves. As shown in Appendix C, the proper sign on the square root is negative $(-i\sqrt{\xi^2 - 1})$ in order to yield evanescent waves. The integral was numerically integrated with a standard Newton-Cotes technique and the calculated impedance is shown in Fig. 3-10. For $(k_\ell L) > 5$, the impedance is mainly real and equal to the plane wave

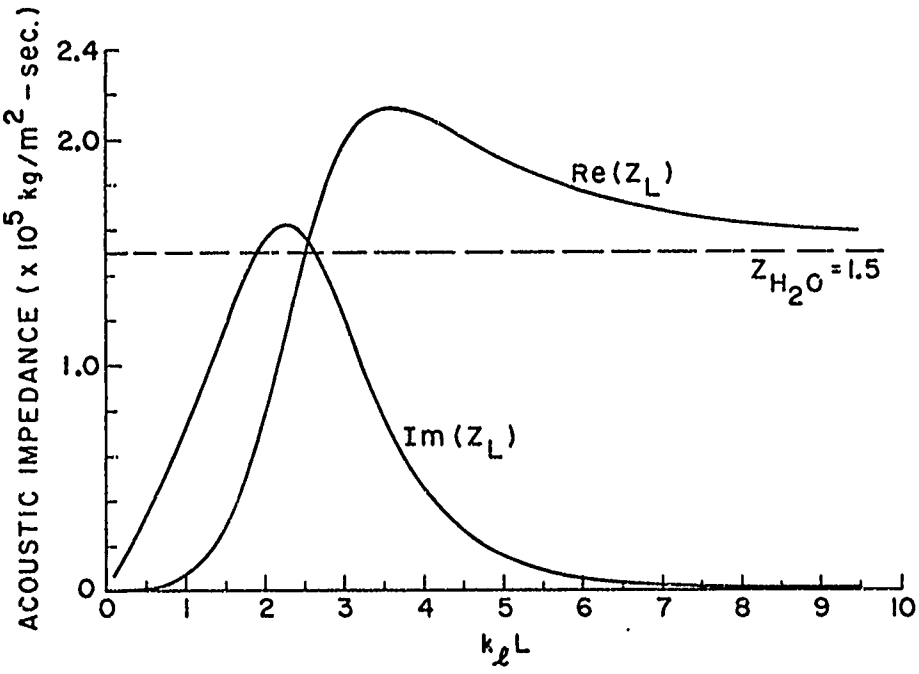

FIG. 3-10. Effective acoustic impedance of water load seen by finite width radiator.

impedance. Below $(k_z L) = 5$, the real part of the impedance rises, then drops rapidly to zero. The reactive part, which is inductive, rises to a peak at $(k_z L) = 2.5$, and then falls to zero as $(k_z L) \to 0$.

As described earlier, the capacitive nature of the load impedance of a solid and the inductive nature of the load impedance of a liquid is similar to the cases of the electromagnetic waveguides in reference 39 since the cases depend on the functional form of the assumed field. In the acoustic case, the difference arises from the inability of a liquid to support a discontinuity in the stress field at the endpoints of the transducer. To show that this difference is real, a case was calculated where the load was a solid with $\sigma = 0.49$, that is, almost a liquid. This case is shown in Fig. 3-11 compared to a water load and a solid with $\sigma = 0.4$. As can be seen in the figure, the $\sigma = 0.49$ solid exhibits a more inductive nature than the $\sigma=0.4$ solid, and the impedance characteristic is intermediate between the two extremes. The effect of this variation in load impedance on the transducer characteristics is shown in the next section. However, for the width of elements used in the experimental arrays, this has little effect on the bandshape of the transducer elements.

E. EXPERIMENTAL RESULTS WITH SIMPLE BACKED ARRAYS

In the previous sections, the theory of tall, thin transducer array elements was described. A simple model to predict the characteristics of the element was developed, and the acoustic load impedance seen by a

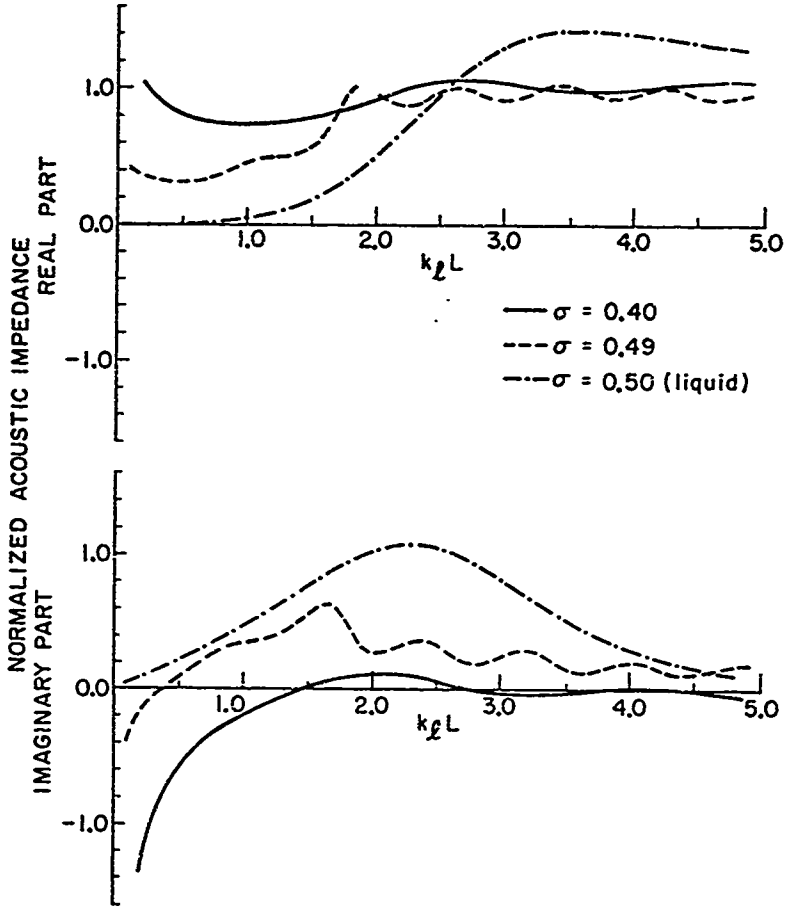

FIG. 3-11. Comparison of effective load impedances of finite width radiatior for Poisson's ratios of 0.4, 0.49, and 0.50.

narrow radiator was described. The construction of broad bandwidth linear arrays of these elements mounted on a high impedance, lossy backing will be discussed in this section including the manufacture of high loss, high impedance tungsten-loaded epoxy. The experimental electrical impedance and insertion loss of these elements will be compared to the theory. The radiation pattern of the elements will also be briefly described.

The easiest technique for achieving broad bandwidth in a water-loaded transducer is to mount the transducer onto a matched backing. Although most of the power generated is radiated uselessly into the backing in this case, bandwidths of 80 - 100% are achievable with ferroelectric ceramics. The bandshape is nearly Gaussian shaped so that an excellent impulse response can be achieved as well. Our first arrays were built using PZT-5A ceramic ($Z_1 = 34(10)^6$) soldered to a lead ($Z_1 = 22(10)^6$) backing. The PZT-5A was lapped to the correct thickness, surface finished with a 5 µm grit and slightly polished. Chrome-nickel electrodes of 2000 Å thickness were rf sputtered on and the ceramic was repoled at 150°C with a voltage of 50 volts per one-thousandth inch to compensate for any depoling which occurred during the sputtering process. A low temperature solder was used to bond the nickel electrode to the lead backing, typically 4 cm thick. Excellent and reproducible transducer characteristics from element to element were achieved with this process. Problems with the bond thickness were eliminated since the solder and lead have nearly the same impedance. Thus, this technique provided an excellent vehicle with which to check the theoretical predictions on transducer response.

Lead-backed arrays are not useful in imaging systems, however. The loss mechanism in lead, which yields about 4 dB/cm loss at 2.5 MHz, is primarily by scattering and not by absorption. The scattered sound in lead backings decays very slowly, requiring several hundred microseconds to decay down to the thermal noise level.[42] This background scattered sound is picked up by the transducer elements and severely limits the dynamic range of a receiver element since the received echo from the water is typically not much greater than the backing noise. However, one lead-backed array with 120 elements 0.635 mm high × 0.381 mm wide × 1.27 cm long on 0.635 mm center-to-center spacing was built and successfully used as a transmitter array in a transmission mode imaging system. A comparison of theoretical versus experimental electrical impedance of one such element is shown in Fig. 3-12. The agreement is excellent and shows the usefulness of the modified one-dimensional model parameters developed in Section B. The load and backing impedances were taken as the simple longitudinal wave mode impedances in this theory. The effect of using the semi-infinite backing impedance calculated in Section D on the electrical impedance is slight as will be shown in the description of tungsten-epoxy backed arrays.

Because of the background noise associated with lead backings and other metals like soft iron and brass, tungsten-loaded epoxy backings were manufactured which yielded not only the high impedance desired, but also the high loss and fast background decay rates. Tungsten is the obvious choice as the filler material because its impedance ($Z_t = 101(10)^6$) is as large as can be found. Composites made of tungsten and epoxy[43] and tungsten and vinyl powder[44] are described in the literature. The first

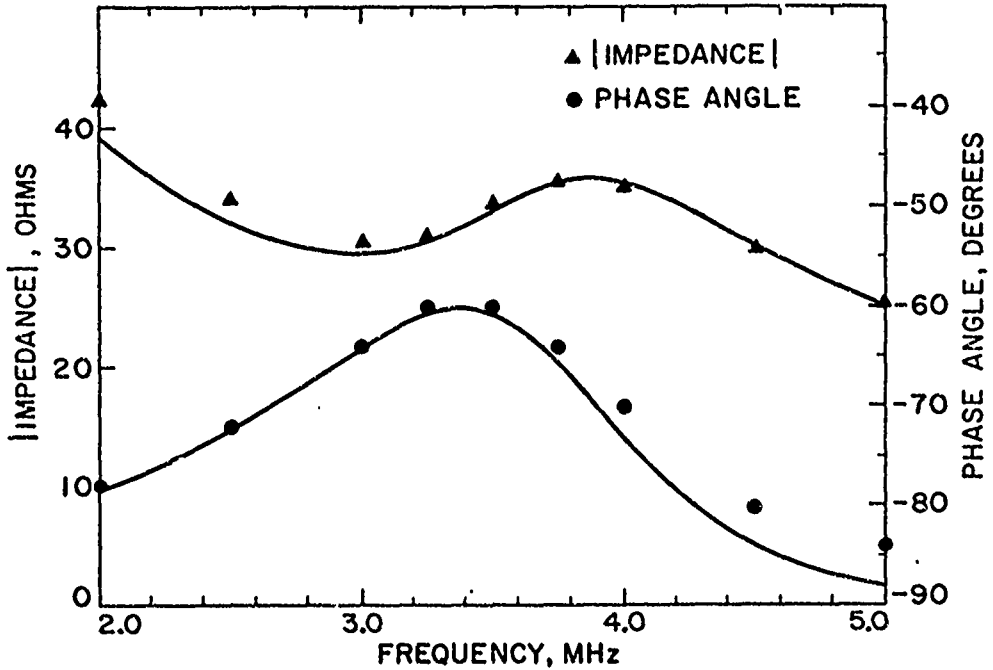

FIG. 3-12. Comparison of theoretical and experimental electrical impedance of lead-backed PZT-5A transducer element 0.635 mm high × 0.381 mm wide × 1.27 cm long.

technique uses tungsten powder mixed with excess epoxy. The excess epoxy is then squeezed out in a press. Backings were readily made using this technique, but the highest impedance achieved was only $Z_\ell = 14(10)^6$. In addition, the material contained many voids which would be disastrous mechanically and acoustically if occurring at the surface where the ceramic is bonded. The second method is carried out by mixing tungsten and vinyl powders in known ratios and combining the matrix with standard hot-pressing techniques. Lack of facilities precluded using this technique. A third method, suggested by L. Zitelli,[45] utilized vacuum impregnation of epoxy into a matrix of tungsten powder. This method was easily implemented. By compressing the powder in a mold to a given density and then vacuum impregnating, backing impedance could be easily varied from $Z_\ell = 12(10)^6$ to $Z_\ell = 40(10)^6$. However, as the impedance rose, the loss dropped. A compromise choice was used for the arays with $Z_\ell = 25-28(10)^6$ with a loss of approximately 8 dB/cm.

All the epoxy backed arrays reported in this thesis were built using a cast-in-place process developed jointly with J. Fraser. In this method, the ceramic was bonded to the backing in the same step where the epoxy was impregnated into the tungsten. This whole process was carried out in a mold. The mold was made in two parts, a bottom plate containing a vacuum tight "O-ring" groove which is then bolted onto the mold itself. The mold is open top and bottom and conformed to the shape of the backing. The ceramic is placed in the bottom of the mold with the bottom plate in position and held flat against the bottom with spring-loaded rods to prevent particles from getting underneath the ceramic. Tungsten powder is poured into the desired thickness and compressed with a ram to the desired

density. Epoxy, Dow Chemical resin DER 332 cured with 14% metaphenylene diamine by weight in this case, is poured on top of the tungsten. The whole mold is then placed into a vacuum station and pumped down to 100 - 300 μ. This process evacuates all of the air from the mold. When the vacuum is released, air pressure simply forces the epoxy into the evacuated tungsten powder. A bar is clamped onto the back of the tungsten-epoxy matrix until the epoxy cures to keep the tungsten particles in intimate contact with the ceramic. This last step is vitally important as a fairly thick epoxy bonding layer develops if omitted. This process eliminates the need for a separate, elaborate bonding process to attach the ceramic to the backing and yields consistent, uniform results. The "equivalent" epoxy bond thickness is less than 1 μm as measured in angle-cut samples and in comparison to theoretical results generated from the computer program.

The impedance of composite backing materials depends strongly on the size, size mixture, and shape of the particles used. A powder containing a range of particles of spherical shape will pack more densely than single-sized or jagged particles. Backings made with Cerac flame spray tungsten powder sieved to -325 mesh (less than 44 microns) with no pressure packing came out with an impedance of $23(10)^6$ when simply vacuum impregnated. However, with shape and size variability between powders, the impedance prediction remains an empirical one.

The loss in these high impedance tungsten epoxy backings is high, but reflections from the back of the backing still limit the dynamic range of the array. The backing may be made as long as desired with consequent size and weight penalties or cut into a wedge-shape as one with another array

reported later. A more rubbery material, whether a vinyl powder, a more flexible epoxy, or urethane, should greatly enhance the loss in the backing. These materials are polymers in general and thus viscoelastic materials; also, rubbery materials tend to be more viscous than elastic.[57] The greater loss in these materials is a result of the higher internal friction in the material and to complicated polymer relaxation phenomena. The Dow resin yields a very low viscosity, low shrinkage, and hard and highly cross-linked epoxy[46] which is excellent for vacuum impregnating but is not as lossy as other binder materials since it behaves more like an elastic material.

Several arrays with 100 to 128 individual elements were built using the cas -in-place, tungsten-epoxy backings just described. The PZT-5A ceramic plate with chrome nickel electrodes was first cut into 10 cm × 1.27 cm × 0.0635 cm slabs so that the free boundary half-wave resonance of narrow slotted elements was 2.97 MHz. The backing impedance was $25(10)^6$ so that the center frequency was downshifted to about 2.5 MHz. Ground connection to the elements was made by laying a 0.001 inch thick brass strip next to the ceramic before pouring the tungsten powder into the mold. Direct soldering of the brass to the nickel electrode was unsuccessful as the high pressure (4000 lb/in^2) necessary to get the impedance desired also tended to crack the ceramic in this case. As the backing was only slightly conductive, the brass was capacitively coupled to the nickel. The individual elements were cut one at a time on 0.020" or 0.025" centers using a 0.006" diamond saw. The kerf of such saws varied from 0.008" to 0.010". This left elements 0.010" to 0.015" wide although each array had element widths varying only by at most 0.001". A gold wire 0.002" in diameter was spot-welded onto the top of

each element to make the hot connections to circuit boards glued to the sides of the backing. Impedance transformers were used to match the high impedance of elements, typically 800 ohms, down to the 50 ohms of coaxial cable.

The arrays were glued into an aluminum housing, and a protective material placed on top of the array. The design of this protective layer is important. Ideally, the spaces between the elements should be air filled to prevent accustic coupling between elements. Epoxy and epoxy filled with glass microballoons were unsuccessfully tried as filler materials. As described later, silicon carbide loaded urethane was successfully used in a quarter wave matched array. The ideal material would be "hard air" which might be made from various hard-setting foams. To protect the top of the array from water and mechanical damage, "hard water" would be the ideal material so as not to disturb the characteristics of the transducers. In the reported arrays, a plastic tape was used which was vacuum suctioned onto the array. This tape was 0.005" thick, but had an acoustic impedance of less than $2.0(10)^6$ and was very pliable. This pliability was important so as to reduce the acoustic coupling through shear waves in the tape. This tape worked adequately for these arrays.

A comparison of the experimental and theoretical electrical impedance of an array element is shown in Fig. 3-13. This 128 element array was used in a reflection mode imaging system[47] where two individual elements were connected in parallel to form one transmitter or receiver element. The individual elements are 0.292 cm wide × 0.0635 cm high × 1.27 cm long backed with $Z = 28(10)^6$ tungsten epoxy. Excellent agreement between theory and experiment is seen in Fig. 3-13. The theory

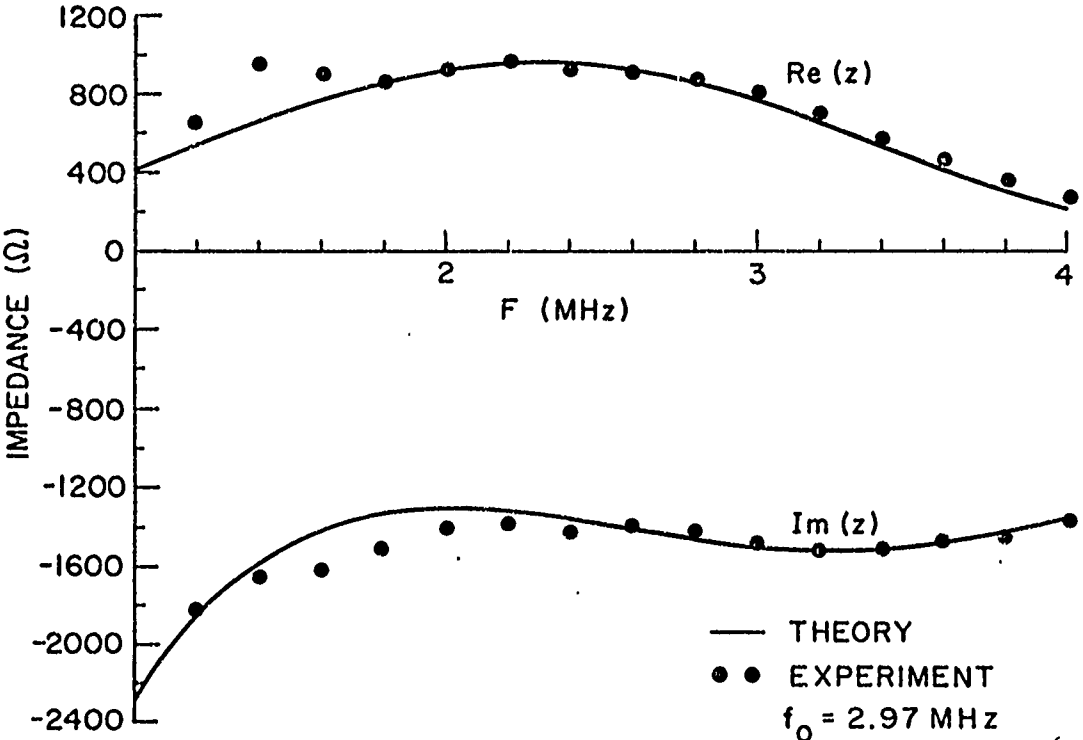

FIG. 3-13. Comparison of theoretical and experimental electrical impedance of $Z = 28(10)^6$ tungsten-epoxy backed PZT-5A transducer element 0.0292 cm wide × 0.0635 cm high × 1.27 cm long.

does include 200 pf series capacitance arising from ground lead coupling through the backing material. The theory does not include the complex load or backing impedance. A comparison of the theoretical electrical impedances of a slotted array element (G = 0.46) is shown in Fig. 3-14 where in one case the plane wave load impedances are used and in the other, the complex effective load impedances are used. The difference between the two cases is small except at low frequencies where a small peak in the real part of the impedance is observed at $f/f_o = 0.25$. The measured electrical impedance, shown in Fig. 3-13, is shown in Fig. 3-14 as well and has a similar peak at $f/f_o = 0.47$. This is consistent with the measured electrical impedances of lead-backed elements shown in Fig. 3-6 with $G = 0.50$ and $G = 0.40$. In these cases there is a peak approximately at $f/f_o = 0.40$. It is very possible that these observed effects are in fact the effect of the complex load impedances. The discrepancy between the measured and predicted peaks could be accounted for by the approximations used in the variational theory. It is clear that for narrow radiators like that in Fig. 3-6 where $G = 0.40$, the peak in the impedance on the low edge of the passband could yield some undesirable resonances in the frequency response and concomitant ringing in the impulse response.

The insertion loss of ten array elements connected in parallel is shown in Fig. 3-15. This 100-element array was used as a receiver in a transmission mode phase contrast imaging system.[48,49] The elements, connected singly, are 0.0366 cm wide × 0.0635 cm high × 1.10 cm long. A 4:1 impedance transformer was used to bring the input impedance of the elements down to the reference 50 ohms; 3.5 dB was added to the measured data to compensate for the power reflected into the spaces between the

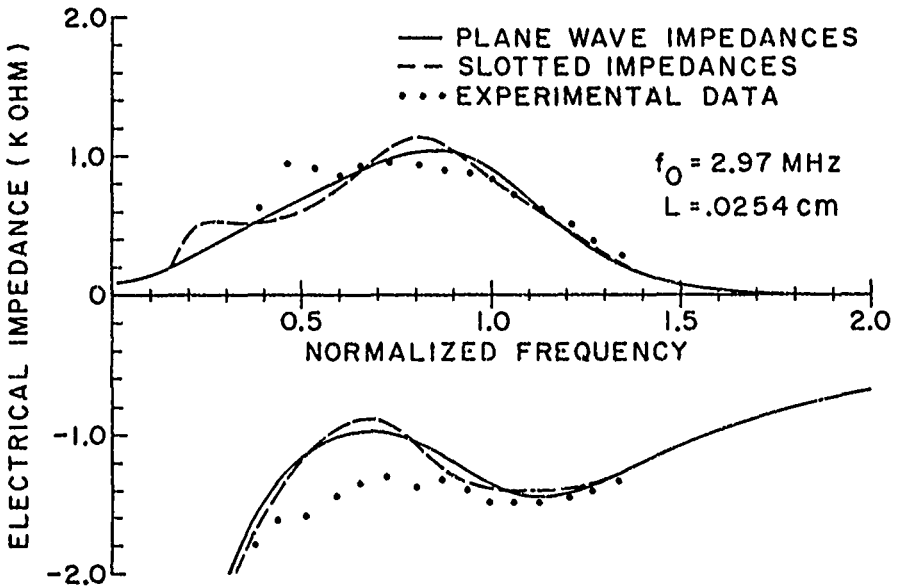

FIG. 3-14. Theoretical electrical impedance of $Z = 25(10)^6$ backed PZT-5A transducer element with $(k_{ot}L)_{backing} = 1.75$ and $(k_{ot})_{load} = 3.16$ showing effect of calculated effective backing and load impedance.

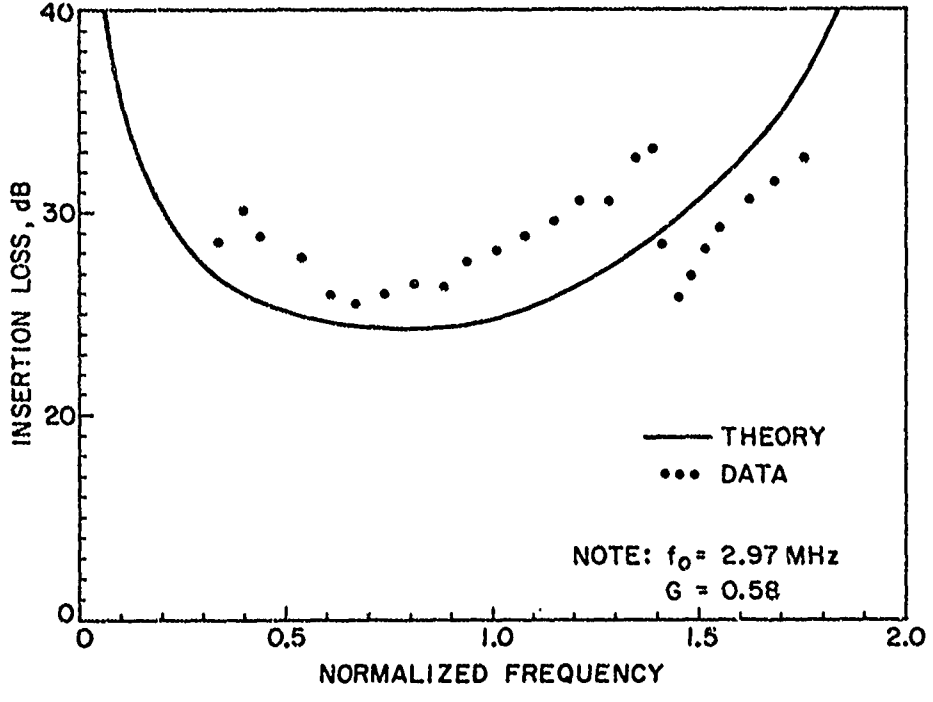

FIG. 3-15. Comparison of theoretical and experimental values of two-way insertion loss of ten G = 0.58 tungsten-epoxy backed transducer elements in parallel. Elements are 0.0366 cm wide × 0.0635 cm high × 1.10 cm long.

elements. Diffraction was neglected as the air-water interface was only 1.0 cm from the array. Good agreement between theory and experiment is seen; the measured bandwidth is 96% and the insertion loss is 25.5 dB. Because G is rather large (G = 0.58) in this case, a strong resonant peak is noted at 4.2 MHz corresponding to the undamped lateral resonance. This was of no concern in the cw imaging system for which the array was used, but in the case where the element is excited by a broadband pulse, this resonance would cause long decay-time ringing in the transducer response.

F. QUARTER-WAVE MATCHED ARRAYS

The efficiency of simple backed arrays can be increased using the acoustic matching techniques described in Chapter II. Quarter-wave matched arrays can be built with one or more full face matching layers or with fully slotted layers and a face plate.

Several quarter-wave matched arrays have been reported in the literature. One array was constructed with two full-face matching layers, one epoxy (Z = 2.7) and the other arsenic sulfide (Z = 8.3), and operating at 2.5 or 3.5 MHz.[50] The bandwidth was reported to be on the order of 70% with theoretical round-trip insertion loss of 0.5 dB. The elements were constructed with a width to height ratio (G) of 0.7 or less which is slightly greater than the narrow element range of $G \leq 0.5$ discussed in this paper. Although not reported in reference 50, the beam width of the elements is expected to be small since the quarter-wave plates are unslotted. This is the case since acoustic cross-coupling through the matching layers could make the effective width of the element much larger than the width of the transducer element. A

second array reported recently is constructed with a single slotted quarter-wave plate[51] on narrow elements with $G < 0.6$ and operating at 2.25 MHz. High efficiency and 30% bandwidth were reported for this configuration. No mention was made of the spatial frequency response. It is known, though not reported in the open literature, that several manufacturers of imaging systems also use single-quarter-wave matched arrays. No data is available on their characteristics.

The array design described here ideally uses two fully slotted layers as shown in Fig. 3-1, so that the angular acceptance is large. Since the matching layers are slotted, the acoustic properties of the sections cannot be treated with a simple plane longitudinal wave theory. A similar theory to that used for the narrow transducer element can be used, however.

If lead zirconate titanate is used as the active material, at least two matching layers would be desirable from the results of Chapter II. Since the slotted element has a large effective coupling constant ($k_{33}'^2 = 0.47$ for PZT-5A), three layers would be more optimal than two. An ideal triple matched element case was computed which had 110% 3 dB bandwidth when air-backed and 74% bandwidth with a backing impedance of $10(10)^6$. However, the increase in bandwidth over that of the double matching layer shown in Fig. 3-17 had only a marginal effect on the impulse response. Because a triple-quarter-wave matched transducer element would be a difficult structure to implement in a fully slotted array, no further development of this case appeared to be warranted. However, the high value of $k_{33}'^2$ for PZT-5A is very important in that no tuning is necessary to achieve high efficiency. A series inductively tuned slotted element only yields about another 2 dB less insertion loss.

From Table 3-2, the slotted ceramic (PZT-5A) has an impedance $30(10)^6$. From Table 2-1 the optimal matching layer impedances for a water load are $4.07(10)^5$ for one layer, $8.31(10)^6$ and $2.30(10)^6$ for two layers, and $13.4(10)^6$, $4.06(10)^6$, and $1.83(10)^6$ for three layers. The theoretical electrical impedance, insertion loss, and impulse response for one and two matching layer array elements are shown in Figs. 3-16 and 3-17, respectively. A backing impedance of $10(10)^6$ was assumed, and no electrical tuning was employed, but electrical impedance matching was. The insertion losses are then 6.5 dB and 6 dB, respectively, at band center, and Gaussian-shaped passbands are partially achieved. The single quarter-wave plate element would have 38%, 3 dB bandwidth and a very symmetric impulse response. The double matched element has 65% bandwidth and a more compact impulse response. The double matched element has a more square bandshape than the single matched case, however, and a less symmetric impulse response. The problem becomes trying to find materials that when slotted, have uniform field distributions and impedances close to the optimums as shown in Figs. 3-16 and 3-17. The design of an experimental double matched array is described which uses glass and epoxy matching sections.

The properties of the matching layers for narrow elements can be calculated using the simple coupled mode resonator theory shown in Section 3-C, assuming that the layers are isotropic. For materials with small values of Poisson's ratio (σ) , the phase velocity in the slotted section remains very close to the longitudinal velocity [Eq. (3-29)] for configuration ratios less than 0.7. Also since C_{13}

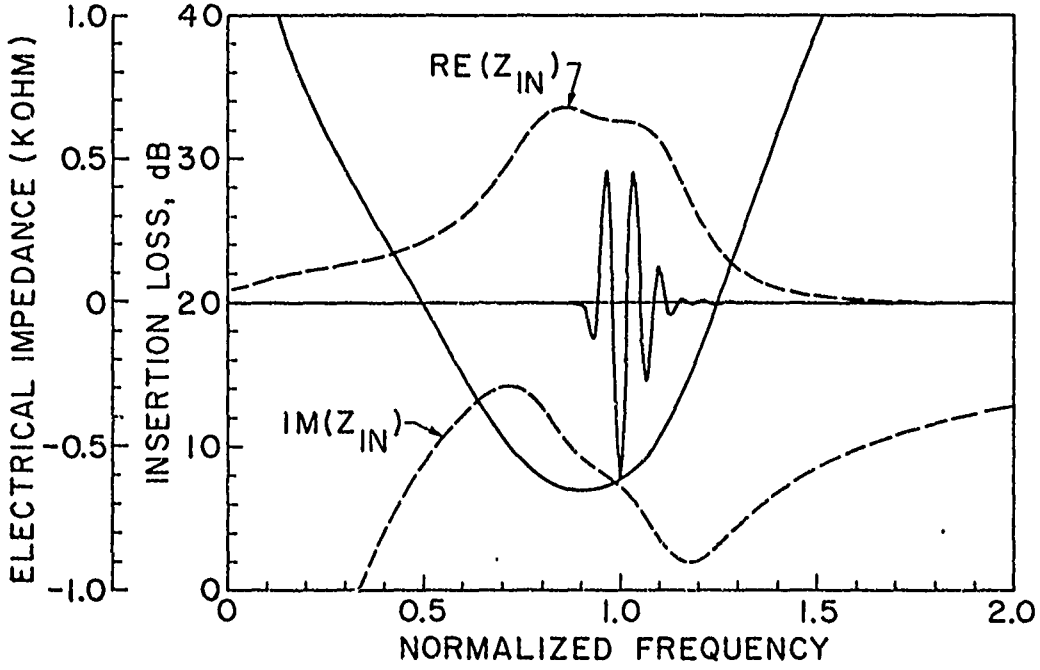

FIG. 3-16. Theoretical electrical impedance, insertion loss, and impulse response for single quarter-wave matched array element.

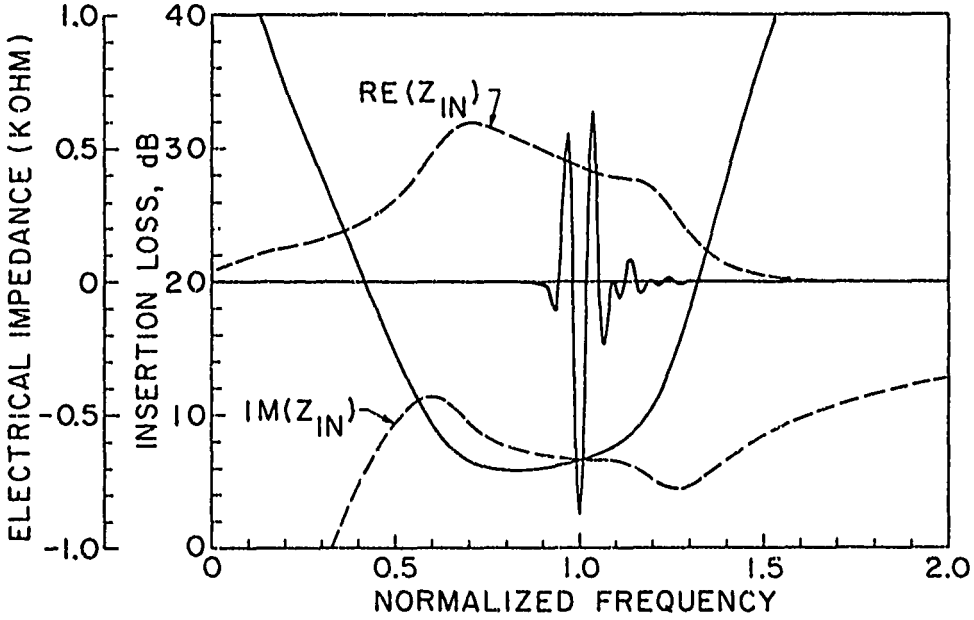

FIG. 3-17. Theoretical electrical impedance, insertion loss, and impulse response for double quarter-wave matched array element.

is small in this case, the extensional velocity is about 90% of the plane longitudinal velocity. The experimental arrays reported here were built with a layer of light borosilicate glass ($Z_\ell = 11.1(10)^6$, $v_\ell = 4.91(10)^6$, and $\sigma = 0.25$) with a configuration ratio (G) of 0.5. The section was considered as a half-wave resonator to determine the properties, and then the height divided in half to make a quarter-wave matching section. With this approach and using Fig. 3-4, the modified parameters for the slotted glass (G = 0.5) were $Z = 10.4(10)^6$ and $v = 4.64(10)^6$. This impedance is not close to the optimal value of $8.31(10)^6$, but there are very few other materials with properties in this range. Arsenic sulfide would be a good choice here, especially if its σ is small; but is not readily available and it is difficult to work with as it cracks easily and is poisonous. Another possibility is a powder-loaded epoxy, but this sort of material usually has a high Poisson's ratio which presents other problems to be discussed.

Another way to examine the properties of these sections is to consider them as short sections of acoustic waveguide. The modes of free boundary isotropic waveguides are the well-known Lamb waves and horizontally-polarized shear waves.[52] The mode of interest here is the lowest order symmetric Lamb wave (the dilatational mode labeled L_1 in most texts). Near the $\beta = 0$ limit, the fields of L_1 are uniform across the guide and are like the extensional mode discussed in the previous sections. In fact, the coupled modes examined in Section 3-C are like the dilatational modes L_1 and L_2 in the $\beta = 0$ limit. It will be assumed that the antisymmetric modes are not excited in the array structure described. The dispersion relation for the symmetric Lamb waves is the Rayleigh-Lamb frequency relation, or

$$\frac{\tan k_{ts} L/2}{\tan k_{tf} L/2} = -\frac{4\beta^2 k_{tf} k_{ts}}{(k_{ts}^2 - \beta^2)^2} \quad , \tag{3-79}$$

where

$$k_{tf}^2 = (\omega/V_t)^2 - \beta^2$$

$$k_{ts}^2 = (\omega/V_s)^2 - \beta^2 \quad . \tag{3-80}$$

Solution of (3-79) for L_1 for small βL shows, as expected, that the phase velocity is the extensional velocity previously calculated. This approach is intuitively more satisfying since the matching sections are treated in the KLM model as sections of waveguide. For small values of βL, the theories give identical results. For the glass matching section in the array to be described, $\beta L = 1.5$ which places it easily in the regime where the L_1 mode is an almost uniform dilatational motion with a phase velocity of $4.64(10)^6$.

However, materials with impedances in the range $2(10)^6$ to $7(10)^6$ are almost all plastics, epoxies, or powder-loaded epoxy composites. These materials are "soft" in the sense that they have small shear stiffnesses and hence large values of σ. The epoxy used in Section 3-E (Dow 332 hardened with metaphenylene diamine (MPDA)) has a σ of 0.37, but most of the others are closer to 0.40. Since C_{13} is relatively large for these materials, the extensional velocity is substantially downshifted from the plane longitudinal velocity as seen in

Fig. 3-4. For $\sigma = 0.37$, $V_e/V_l = 0.82$ and for $\sigma = 0.40$, $V_e/V_l = 0.74$. The impedance of a slotted element, operating in the pure extensional regime would also be downshifted. The Dow 332/MPDA epoxy would then have an impedance of $2.77(10)^6$. The strong coupling in this material, since the coupling constant is $(C_{13}/C_{11})^2$ from Eq. (3-31), starts to upset the extensional nature of the mode for values of G greater than about 1/3.

The two lowest order dilatational modes L_1 and L_2 for this material are plotted in Fig. 3-18. It is easily seen from the figure that to operate the section in the L_1 dilatational mode, $\beta L = (\omega/V_p)L$ must be on the order of one. To operate at a center frequency of 3.79 MHz, the width of the section must then be from the figure about 90 μm. The height of the element for quarter-wave operation at 3.79 MHz would be 149 μm. The total height of the element including the ceramic and two quarter-wave sections would be 911 μm. The element would be ten times higher than it was wide. This is an extremely hard configuration to fabricate for high frequency arrays, especially with many elements. The elements would be extremely fragile and difficult to cut with either diamond saws or wire saws.

An alternative solution would be to use a full face quarter-wave plate over the entire top of the array. As shown in Section 3-D, longitudinal, shear, and Rayleigh waves would be launched into this medium, but if the element were not too narrow, that is if βL were one or greater, the impedance of the layer would be very close to the simple longitudinal wave impedance. This full face quarter-wave plate would also act as a protective coating over the face of the array, not letting water penetrate between the elements and mechanically supporting the

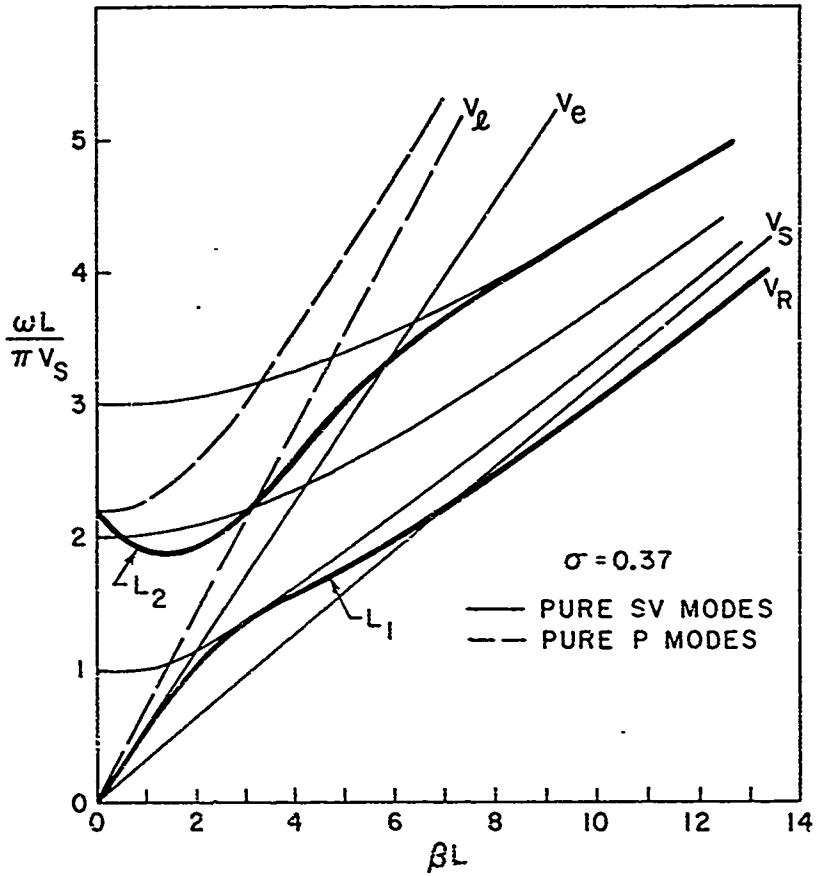

FIG. 3-18. Dispersion curves for the two lowest order dilatational Lamb waves of isotropic waveguide.

array structure. The penalty for using this approach is introducing acoustic cross-coupling between the elements from modes excited in the full face layer. As will be shown, it is desirable from angular beamwidth considerations to keep this cross-coupling below 25 dB. However, even in a fully-slotted array, a face plate is required and the same considerations apply. The face plate in this case should be made of an acoustically identical material to water. Some polyurethanes come close to this requirement. One is used in reference 51 as a protective face plate which has virtually identical acoustic properties to water.

A 180-element quarter-wave matched array was designed and built to operate with fully-slotted elements at a 3.8 MHz center frequency. The array was fabricated by epoxying a 0.018" thick × 4" × 0.490" wide slab of PZT-5A with 2000 Å thick chrome nickel electrodes to a 0.012" × 4" × 0.455" piece of borosilicate glass. The extra width of PZT-5A was included in order to make electrical connection. The thin-bonding technique of Papadakis[33] was used to insure a negligibly thin bond between the glass and ceramic. This slab was then epoxied, using the same technique, to a backing of silicon carbide loaded epoxy ($Z = 9.4(10)^6$) formed into a long wedge shape (2.5" × 0.5") with a lossy flexible epoxy coat around the wedge. The long wedge shape with an included angle of 11.4° enabled the acoustic waves to be reflected from the sides of the wedge 8 times before being re-reflected back towards the ceramic. The increased path length and many reflections served to attenuate the signal greatly by loss in the backing (8 dB/cm), mode conversion into shear waves, and refraction into the surrounding lossy flexible epoxy. A wedge with an included angle of 20° would have only three reflections

before being directed towards the ceramic. Experimentally, a commercial transducer (3.5 MHz) was used to launch a pulsed signal into the backing wedge. The resultant signal noise was 30 dB below that of a reflected signal from a flat surface in aluminum 1 cm thick. Electrical connection was made with 0.001" thick brass leads 0.010" wide on 0.020" centers soldered to both edges of the ceramic. A 0.004" thick piece of Dow 332 epoxy was then cast onto the front of the glass to make the outer quarter-wave plate. The electrical connections were brought down the sides of the backing by leads on printed circuit boards. The elements were then diamond sawed with a 0.006" blade. The kerf of the saw was 0.008" resulting in elements 0.012" wide on 0.020" centers. A photograph of this array is shown in Fig. 3-19.

In this configuration, $G = 1.5$ for the epoxy section and if operating in the extensional mode, an expected phase velocity of $1.35(10)^6$ and impedance of $1.66(10)^6$ from Fig. 3-18. Hence this section is virtually identical to water and has little effect on the characteristics of the element. The experimental impedance for this element is shown in Fig. 3-20. A pronounced peak at bandcenter is unexpected and appears to result from the epoxy section mode hopping to a higher order mode where the effective impedance and phase velocity are much higher. As the width of the epoxy quarter-wave matching layer is greater than the height by 50% in this case, it is difficult to predict the exact nature of the fields in the section. The electrical impedance of a transducer element is shown in Fig. 3-20 compared to a theoretical calculation where the modal velocity and impedance of the epoxy matching section is taken to be the simple plane longitudinal ones ($v_L = 2.75(10)^3$, $Z_L = 3.38(10)^6$). In this case, the thickness of the epoxy matching

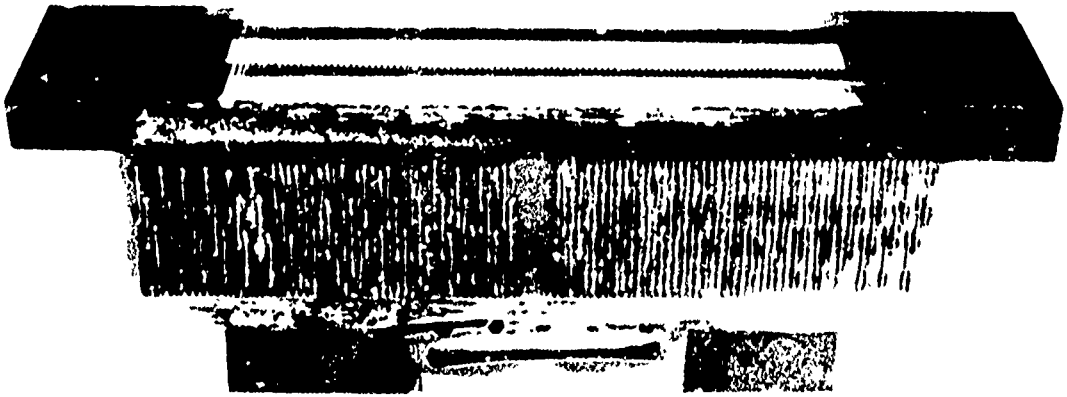

FIG. 3-19. Photograph of 180-element double quarter-wave matched array.

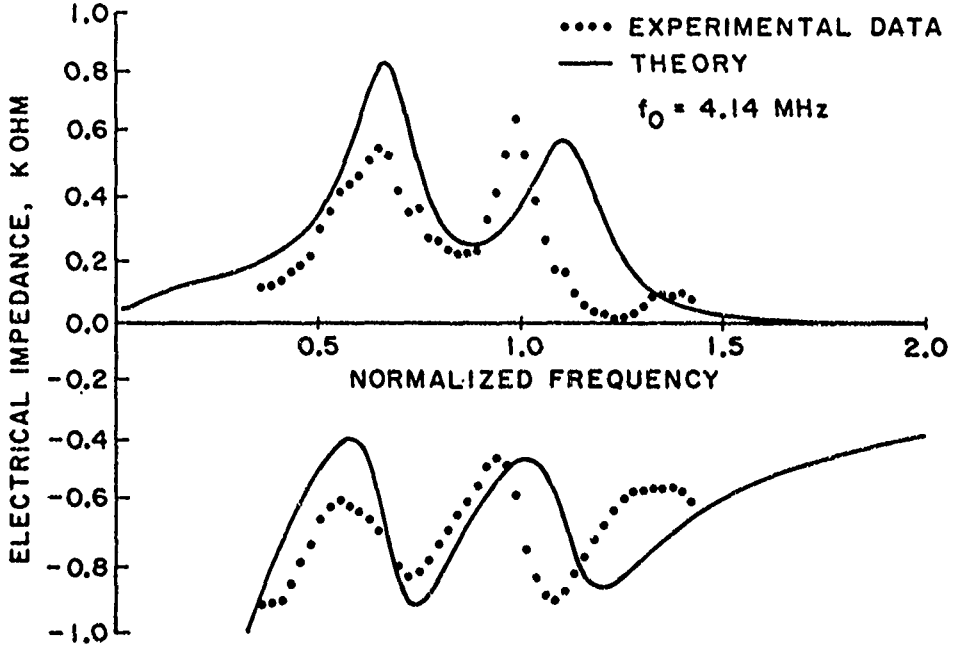

FIG. 3-20. Experimental electrical impedance of one element of array in Fig. 3-19.

section is 0.153 λ_o where λ_o is the wavelength corresponding to the resonant frequency f_o of the ceramic. This is not close to the optimal quarter wavelength thickness and gives a very peaky frequency response. The match between theory and experiment is not very good, but this calculation does predict the strong peak near f_o shown in the experimental data.

In order to smooth out the frequency response of the array elements, an additional 0.004" thick layer of epoxy was glued onto the face of the array so that the total thickness of the epoxy was 0.008". In addition, before this layer was attached, a mixture of highly absorptive silicon carbide loaded polyurethane was vacuum impregnated into the grooves between the array elements. This measure served to damp out the lateral resonance of the transducer elements which had been evident in the impulse response. It also gave greater structural rigidity to the array itself. The addition of the extra layer of epoxy had the desired result in that the frequency response of the elements was smoothed out as shown in a plot of the electrical input impedance in Fig. 3-21. A theoretical curve is shown in Fig. 3-21 which assumes that the modal velocity and impedance of the epoxy, including the slotted section and the extra full face layer, are the simple longitudinal ones. The match is not good, especially at the high frequency end where the theory does not predict the low radiation resistance seen in the experimental data. The complicated nature of the modes excited in the slotted epoxy matching section appear to preclude a better prediction of the transducer characteristics. However, the smooth frequency response of the element yields a compact impulse response as will be shown. The insertion loss is quite low as well.

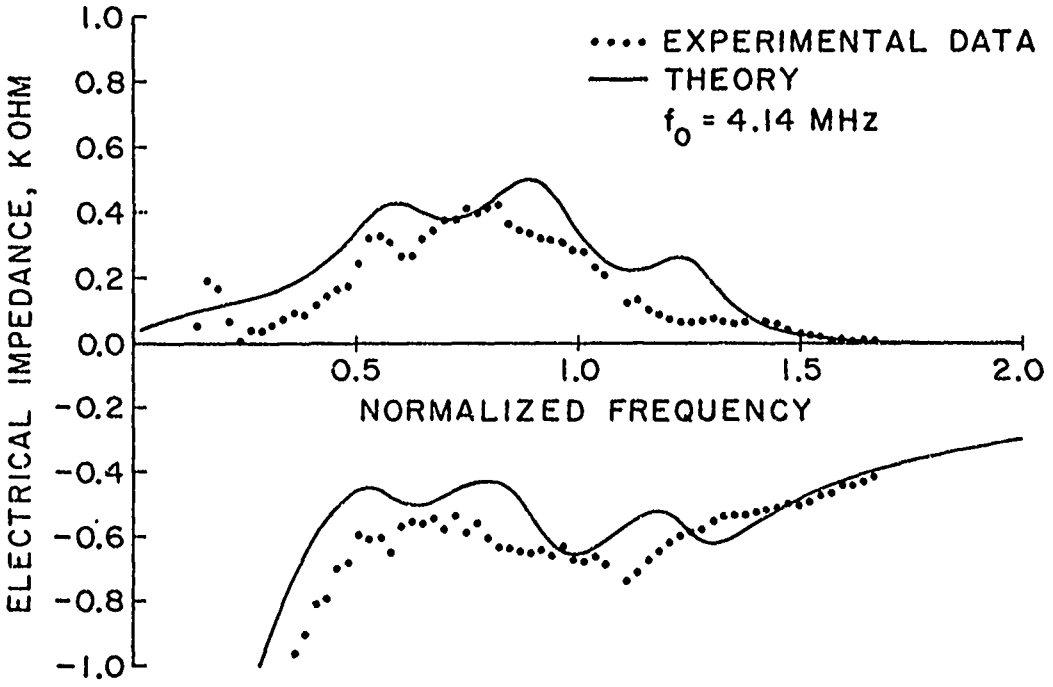

FIG. 3-21. Effect of adding epoxy face plate on experimental electrical impedance of array in Fig. 3-19.

The insertion loss of the transducer array elements was determined by first connecting 14 elements in parallel so that the effects of diffraction loss would be largely eliminated in the reflection mode experiment to be described. This procedure gave an input impedance of 52 ohms at -45° at 3.5 MHz so that the elements could be matched to a 50 ohm generator. The transmitted signal was reflected off an air-water interface approximately 0.5 cm away, and the received signal measured with a high impedance probe so that the transducer elements were loaded by the 50 ohm generator. The total 14-element length was 0.7 cm so that the path length in water was well within the Rayleigh range (approximately 10 cm in this case). An additional 2.2 dB was added to the experimental data shown in Fig. 3-22 to account for the reflected signal which was incident upon the gaps between the elements (0.008" gaps to 0.012" wide elements). This assumes that the signals produced from the individual elements would diffraction spread and upon reflection produce a uniform beam incident back upon the face of the transducer array.

As seen in Fig. 3-22, the minimum round-trip insertion loss is 11 dB at 3.85 MHz, and the 3 dB fractional bandwidth is 45%. The 3 dB cutoff frequencies are 2.73 MHz and 4.26 MHz. The 6 dB cutoff frequencies are 2.57 MHz and 4.43 MHz. The bandshape is flat over the passband with a 1.5 dB bump at 3.85 MHz. For comparison, the theoretical insertion loss of an element with the same parameters as in Fig. 3-21 is also shown in Fig. 3-22. The theoretical case shows 6 dB round-trip insertion loss and an 82% 3 dB bandwidth. The extra 5 dB loss in the experimental data is difficult to explain but is consistent with practically every transducer the author has made. Most of the loss in bandwidth occurs at the high frequency end as was noted

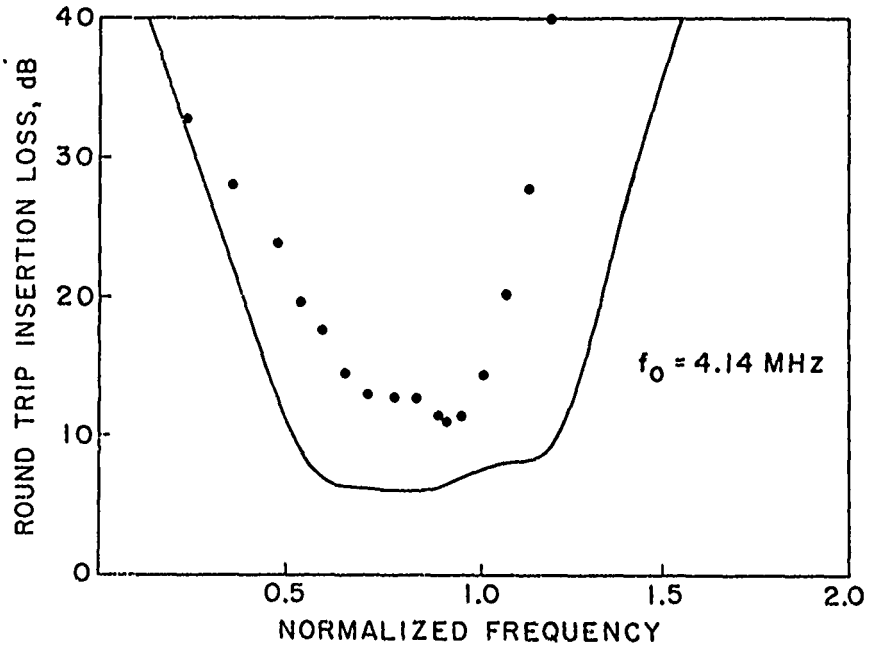

FIG. 3-22. Comparison of theoretical and experimental two-way insertion loss of array in Fig. 3-19.

earlier. The decrease in bandwidth is responsible for the extra cycle in the experimental impulse response shown in Fig. 3-23, over that expected of a 70 - 80% bandwidth transducer.

The experimental impulse response was also measured using the 14 elements connected in parallel and observing the reflection off an air-water interface. The excitation was a single 3.0 MHz cosine pulse generated from an Exact 7271 generator and is shown in Fig. 3-23(a) as loaded by the transducer elements. The impulse response is shown in Fig. 3-23(b) and consists basically of a 5 half-cycle response at 3 MHz.

Since each transducer element has a very high impedance, on the order of 750 ohms, it is necessary to transform this impedance down to 50 ohms for optimal impedance matching into a 50 ohm cable. Transformers were wound with an 8:31 turns ratio on high permeability ferrite cores (Indiana General 7704) so that the impedance of an element was 50 ohms at 3.5 MHz. The large number of turns was necessary to increase the parasitic parallel inductance and resistance in the transformer to large enough values so that they had minimal effect on the bandshape and insertion loss of the elements. The transformers take 50 V on the primary without saturation or 200 V on the element itself. The parallel inductance does not affect the real part of the element impedance above 1.6 MHz, but there is a slight tuning effect on the imaginary part. This would serve to lower the insertion loss by a small amount.

The impulse response of a single impedance matched element was measured by P. Grant by reflecting a signal off a 0.018 cm diameter wire target. The excitation and impulse response are shown in Fig. 3-24.

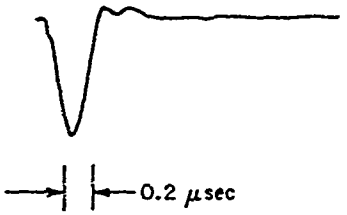

(a) EXCITATION

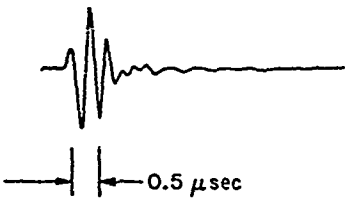

(b) IMPULSE RESPONSE

FIG. 3-23. Experimental impulse response of 14 elements of array in Fig. 3-19.

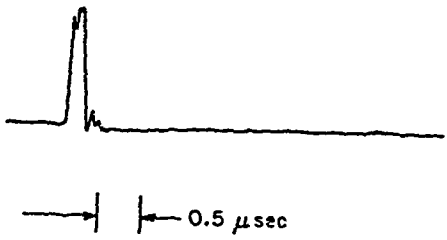

(a) EXCITATION

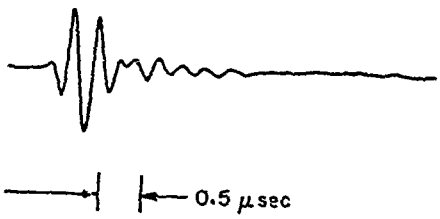

(b) IMPULSE RESPONSE

FIG. 3-24. Experimental impulse of one element of array in Fig. 3-19 reflected off wire target.

The excitation was a 0.25 μsec wide square pulse in this case. The impulse response shows a 3.5 MHz 5 half cycle response very similar to that shown in Fig. 3-23(b). Additional ringing 14 dB down from the main response is observed which extends 1.5 μsec beyong the main response before decaying away.

The angular acceptance of a single impedance matched element was measured by rotating the array about the long axis of the element while insonified by plane wave from a transmitting transducer. The measured angular acceptance is shown in Fig. 3-25 for four frequencies and is compared to the theoretical response predicted from Eq. (1-1). The measured 3 dB acceptance angles were ±24° at 2.5 MHz, ±23° at 3 MHz, ±16° at 3.5 MHz, and ±6.5° at 4 MHz. The values are much less than the ideal values of 61°, 47°, 38°, and 31°, respectively, obtained from Eq. (1-2). These low measured acceptance angles are attributed to strong cross-coupling between the array elements, mostly in the full face epoxy layer on the face of the array. However, the acceptance angles are adequate for most imaging systems.

G. CROSS-COUPLING BETWEEN ARRAY ELEMENTS

Acoustical and electrical cross-coupling between the elements of an array can produce undesireable artifacts in the spatial frequency response of an individual element. As shown in Eq. (1-1), the spatial frequency response of an element with no coupling is a simple sin x/x

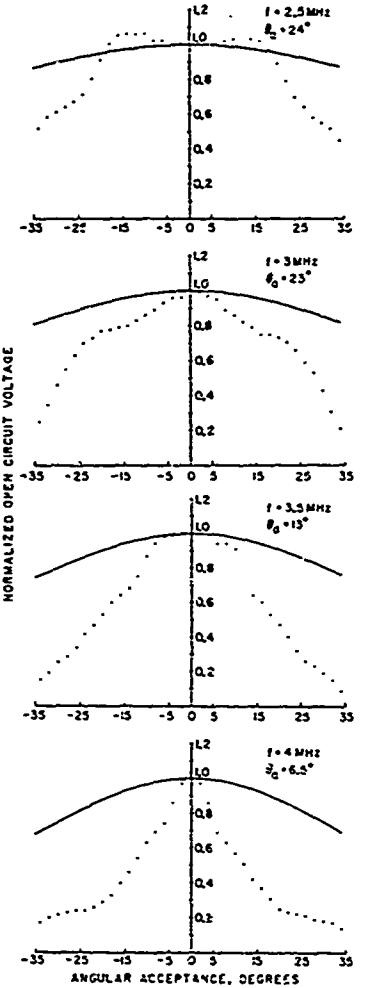

FIG. 3-25. Comparison of theoretical and experimental angular acceptance of a double quarter-wave matched transducer array as a function of frequency.

response:

$$F(\theta) = \sin(kL \sin \theta/2)/(kL \sin \theta/2) \qquad (1\text{-}1)$$

where k is the wavenumber in the load medium, L the width of the element, and θ is the angle away from the surface normal. If the cross-coupling is large, the spatial frequency response can be quite different than Eq. (1-1) and the angular beam width reduced significantly. One kind of cross-coupling would be distributed coupling in an array face plate. If the acoustic impedance of a face plate were different than that of the load medium, a transmitted signal from one element would be partially reflected from the face plate-load interface and be transmitted at points laterally down the face plate away from the transmitting element. The net effect would be an effective radiating surface wider than the transmitting element. The spatial frequency response would be somewhat like that of Eq. (1-1) except that the width, L, of the element would have to be replaced by an effective width, $\bar{L}$, where $\bar{L} > L$. Therefore, the acceptance angle would be smaller than that predicted by Eq. (1-1). Radiation from excited filler material between slotted elements could also have this effect.

Adjacent elements to the transmitting element can be excited acoustically or electrically. A simple theory can be constructed to account for this sort of coupling by assuming the coupling amplitude to be of the form $\alpha e^{i\beta}$ where α is a coupling coefficient and β is a phase shift. The coupling to the n^{th} nearest neighbor then will be $\alpha^n e^{in\beta}$. The spatial frequency response is easily shown to be

$$F(\theta) = A \operatorname{sinc}(kL \sin \theta/2) \left[1 - 2 \sum_{0}^{N} \alpha^n e^{in\beta} \cos(nkd \sin \theta)\right] \qquad (3\text{-}81)$$

where L is the center-to-center spacing and N is the number of neighboring element pairs. As can be seen in Eq. (3-81), the first term is just the uncoupled $\sin x/x$ response of a single element. The term in brackets is the modulation due to excitation of neighboring elements.

Some of the effects of cross-coupling can be demonstrated by examining plots of the spatial frequency response shown in Eq. (3-81). In Fig. 3-26, $|F(\theta)|$ is shown for several values of coupling coefficient including only nearest neighbor coupling and assuming 2π phase shift, a center-to-center spacing to width ratio (L/l) of 2, and $k = 168$. It can be seen that coupling of -20 dB introduces fairly significant modulation of the beam pattern and a reduction in the 3 dB half beam width from 40° to 15°. Similar results show that cross-coupling should be kept to below 25 to 30 dB in order to achieve broad acceptance angle transducers. The effect of phase shift can alter drastically the form of the spatial frequency response as seen in Fig. 3-27. In this figure, $|F(\theta)|$ is plotted for 0° and 90° phase shifts for -3 dB element-to-element coupling including 10 pairs of neighboring elements. The same parameters are assumed as in Fig. 3-26. In this case, when a 90° phase shift is introduced, there is a minimum in the response at $\theta = 0^{\circ}$ instead of a maximum. As can be seen, interpretation of the spatial frequency response can be complicated when the coupling is strong.

Most of the arrays built by the author had elements connected in parallel in pairs in order to introduce zeroes in the spatial frequency response where the first imaging system grating sidelobes occurred. Therefore, the angle of acceptance of one double element was dominated

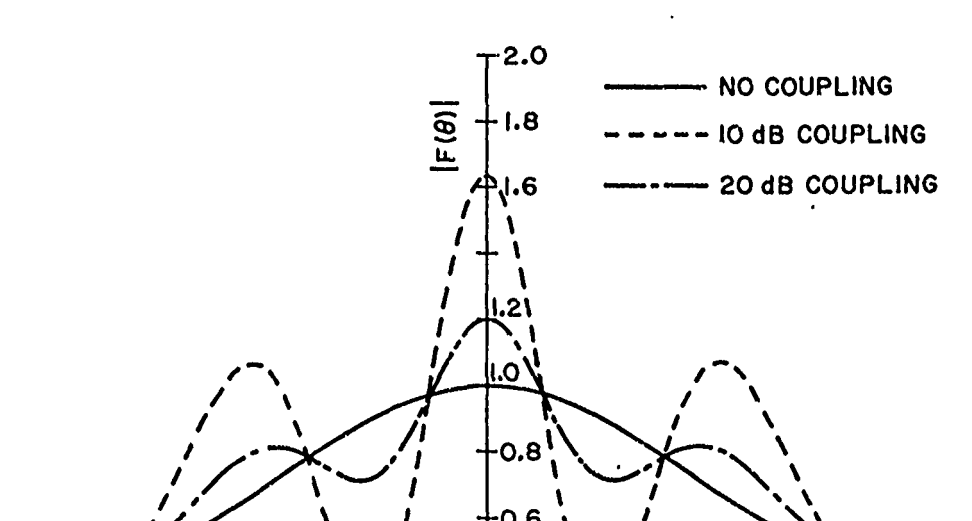

FIG. 3-26. Effect of cross-coupling on angular response of an array element.

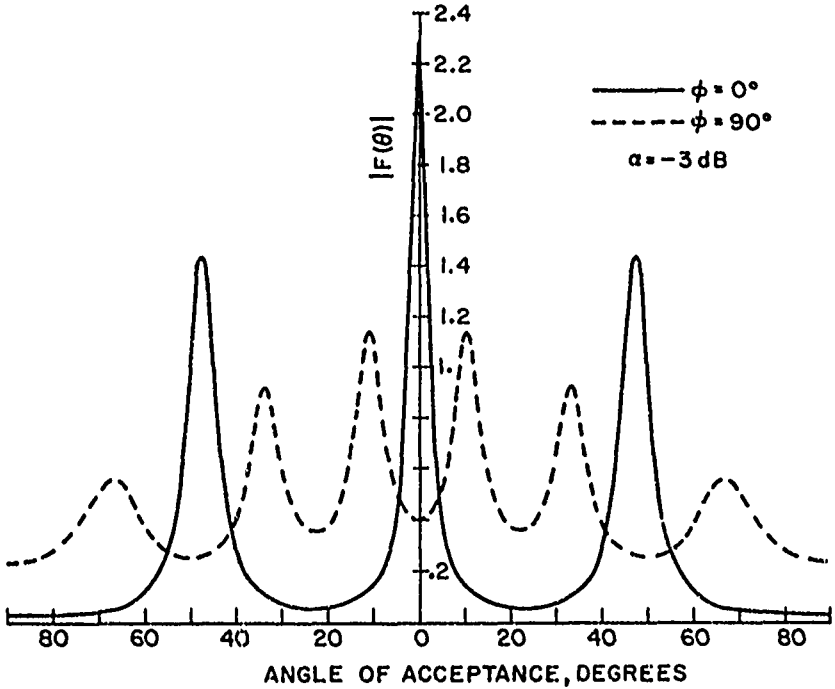

FIG. 3-27. Effect of phase shift in the cross-coupling on the angular response of an array element.

by a term like $\cos(kl \sin \theta/2)$. However, one tungsten-epoxy backed array was built in which a 0.004" thick epoxy face plate was cast onto the front of the array and in between the individual elements. The array has 0.0147" wide double elements with 0.025" center-to-center spacing between the elements. The epoxy face plate and filler introduced strong cross-coupling in the array which is evident in the angular acceptance curves shown in Fig. 3-28. Since the curves in Fig. 3-28 are only shown for $|\theta| \leq 20^{\circ}$, the peaks at $\theta = 40^{\circ}$ to 60° from the double element are not seen. However, the changes in the spatial frequency response due to the cross-coupling are evident and are strongly frequency dependent. A frequency varying phase shift could yield the response seen in Fig. 3-28. It is clear that filling in the spaces between elements with material like epoxy and using a face plate acoustically different than water unacceptably degrades the spatial frequency response of the array.

A plot of acceptance angle for a lead-backed array with a thin Mylar face plate is shown in Fig. 3-29. Good agreement between experiment and theory is shown in this plot with small cross-coupling introducing small peaks at $\pm 23^{\circ}$. In later arrays, a commercial brand (3m) plastic self adhesive clear plastic tape was also found to be acceptable as a face plate and had the advantage of being very easy to apply. This tape is 0.005" thick, is very flexible, and stretches easily. The tape was applied by vacuum suctioning the tape down to the face of the array. The angular acceptance of the tungsten-epoxy backed array described in Fig. 3-15 which uses this tape as a face plate, is shown in Fig. 3-30 at frequencies of 2.5 MHz, 3 MHz, and 4 MHz, respectively.

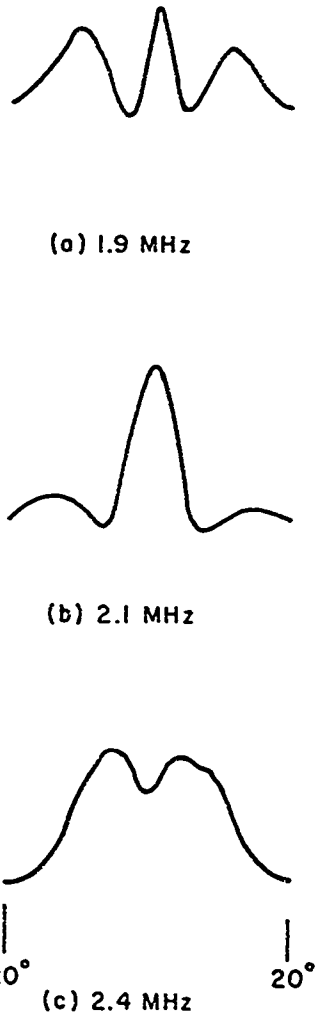

FIG. 3-2b. Experimental angular response of an array with a large amount of cross-coupling.

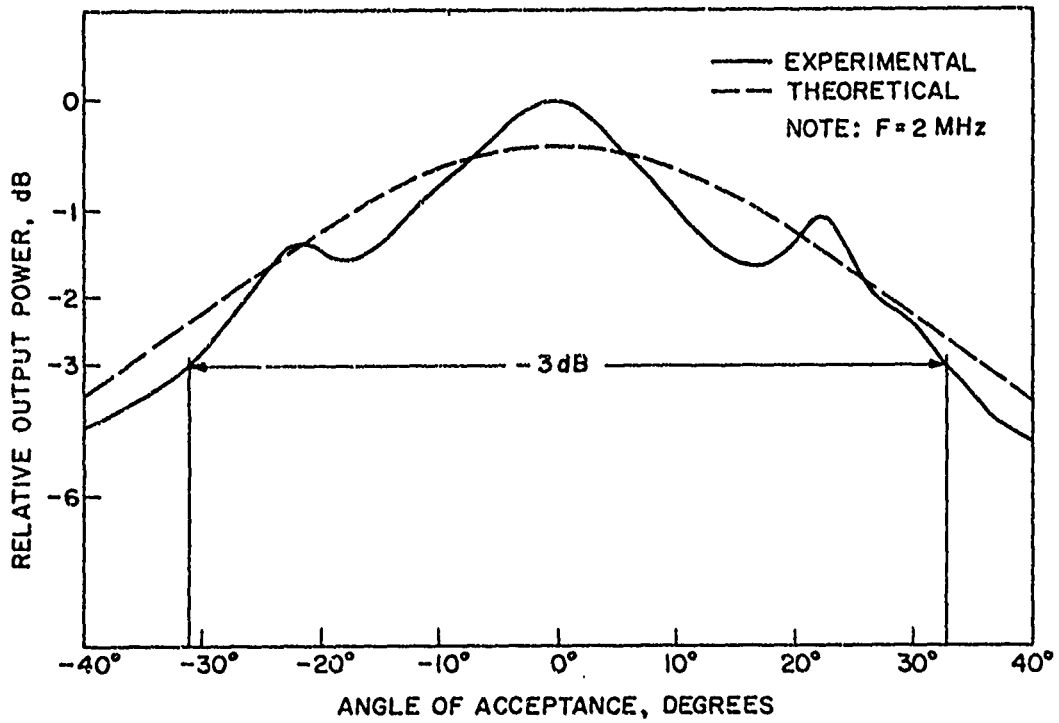

FIG. 3-29. Comparison of theoretical and experimental angular response of tungsten-epoxy backed array element.

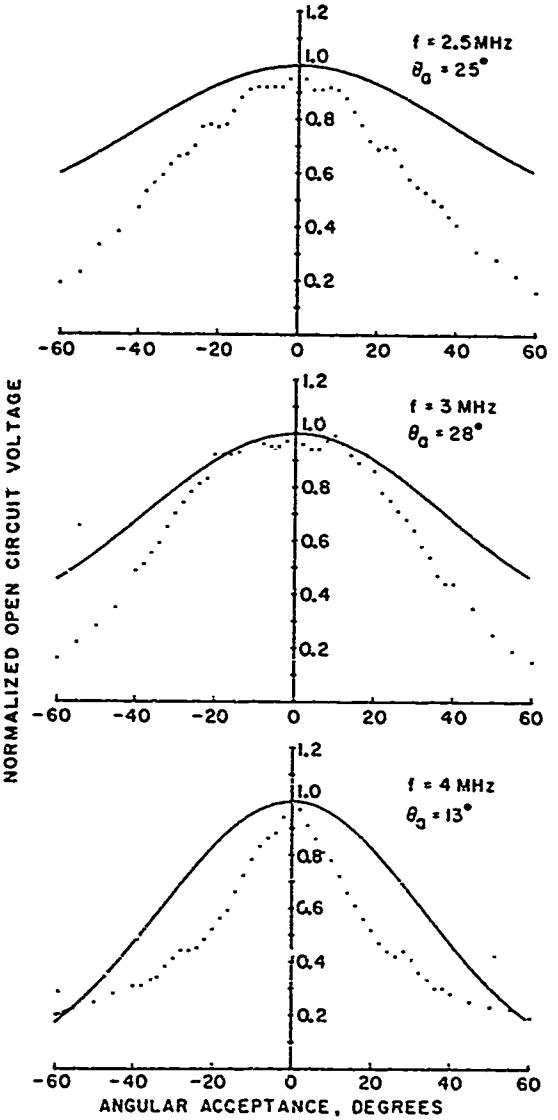

FIG. 3-30. Comparison of theoretical and experimental angle of acceptance of tungsten-epoxy backed array element. Same array as shown in Fig. 3-15.

The measured acceptance angles of 25°, 28°, and 13°, respectively, are somewhat less than the theoretical angles of 48°, 38°, and 28° predicted from Eq. (1-2). However, there are no large peaks or valleys in the overall beam pattern. A best solution would be to use a material with acoustic properties similar to water for the face plate. As mentioned earlier, some polyurethane materials meet this requirement.

CHAPTER IV

MONOLITHIC TRANSDUCER ARRAYS

A. INTRODUCTION

A second type of transducer array suitable for acoustic imaging makes use of an acoustically matched monolithic slab of piezoelectric material onto which individual electrodes have been deposited to form the array elements.[18,19,42] Standard photolithographic techniques make the construction of this kind of array a relatively simple, flexible, and inexpensive process. By acoustically matching the ceramic with a matched backing or with quarter-wave plates into the load, not only would the bandwidth and efficiency be greatly increased as already discussed, but also the acceptance angle can be made to approach the critical angle of the load-ceramic interface.

In an unmatched transducer, waves entering the ceramic from water will be reflected and re-reflected within the ceramic because of the high impedance mismatch at each surface of the transducer. These reflections add to give a strong signal near normal incidence, but at angles other than normal, the signal level falls radically. This can be quantified by reasoning that the transducer response is maximum when $kl \cos\theta_o = \pi$, where k is the propagation constant of a wave in the transducer material, l is the thickness of the transducer, and θ_o is the angle of the wave propagating through the ceramic makes to the normal, as shown in Fig. 4-1.

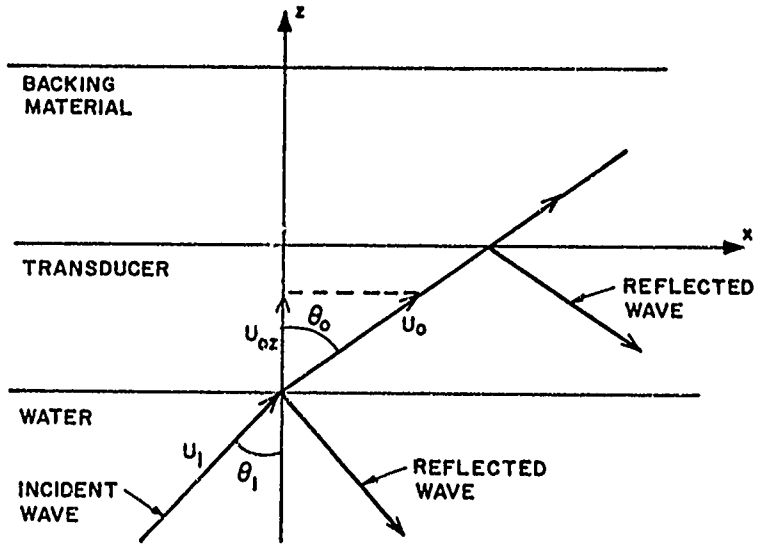

FIG. 4-1. Schematic drawing of a backed transducer showing parameters of interest.

An unbacked PZT-5A transducer with water on one side has a Q_a of 36 from Eq. (2-6), so the bandwidth would be only about 3%. From the above formula, the angle of acceptance in the ceramic would be where $\cos \theta_c = f_o/f_u = 0.985$ or $\theta_o = \pm 9.9^\circ$. From Snell's law then, the angle of acceptance is where the incident angle is $\theta_i = \pm 3.4^\circ$. In addition, the reflected waves bouncing back and forth down the monolithic slab would result in strong cross-coupling to adjacent electrodes. The slotted transducer is free from this defect since the only communication is acoustically through the backing or face plates or electrical pick-up.

These problems can be overcome by acoustically matching the piezoelectric material on either face.[18] In this case, the Q of the resonator will be small, and the plane wave entering the transducer will not be re-reflected from the matched face. Thus, there is no build-up of field at normal incidence, and the angle of acceptance and bandwidth will be large. An angle of acceptance approaching the critical angle of water to the active material can be obtained in a well-matched transducer array. For PZT-5A ($\bar{v}_a = 4.35(10)^6$), the longitudinal critical angle in water is 20.2°. For lead metaniobate, this critical angle is 32°.

An interesting case utilizes PVF_2 plastic film as the active material. Since the impedance of PVF_2 is $3.82(10)^6$,[32] a broadband transducer with good efficiency can be easily constructed[30] without the use of quarter-wave plates. Also since the velocity of PVF_2 is only $2.15(10)^3$, the longitudinal critical angle is 44° which is larger than any other piezoelectric material for this monolithic structure. Theoretical predictions of the spatial frequency response of such an array

is included in Section 4-E.

Monolithic arrays should also prove to be very useful in some nondestructive testing applications. In this case, the monolithic slab could be affixed directly to a glass or metal block which would be in direct contact with the test sample. Alternatively, the piezoelectric slab could be in direct contact with the test sample. Longitudinal or shear waves could be directly coupled into the sample; or by using mode conversion at a free boundary in the block, shear waves could be launched into the test specimen from a longitudinal wave array. With the ideal impedance match available in this case, excellent efficiency, bandwidth, and broad beamwidth operation can easily be achieved without the necessity of slotting. One such array was built and is described in Section 4-F. This array, using PZT-5A on aluminum, showed the excellent broad, uniform beam pattern predicted by theory. Monolithic arrays should find wide application in nondestructive testing applications.

B. THEORY OF ANGULAR DEPENDENCE OF MONOLITHIC TRANSDUCER

A simple physical picture of the angular dependence of a monolithic transducer element can be obtained by considering the simplest possible case, that of a transducer with perfectly matched backing, as illustrated in Fig. 4-1. A plane wave with displacement amplitude u_i is assumed to be incident on the transducer from the water load at an angle θ_i. The longitudinal component of the refracted wave travels in the transducer at an angle θ_3 determined by Snell's law. Assuming that u_z and T_3 are continuous at the interface, the transmission

coefficient can be obtained and the induced voltage V expressed in terms of the acoustic velocity amplitude of a plane wave entering the array at incident angle θ_i. Shear terms are ignored for simplicity, and u_o is taken as the displacement corresponding to a plane wave propagating in the ceramic at an angle θ_o to the z-axis. The magnitude of the propagation constant $\bar{k}_o$ of the wave is determined from the stiffened velocity and is in the direction θ_o. In this case, strains associated with the wave are

$$S_3 = -ik_o u_o \cos^2\theta_o = -ik_o u_{oz} \cos\theta_o \quad , \tag{4-1}$$

$$S_1 = -ik_o u_o \sin^2\theta_o = -ik_o u_{oz} \sin\theta_o \tan\theta_o \quad , \tag{4-2}$$

and the exponential dependence has been suppressed. Assuming open circuit conditions ($D_z = 0$) one then obtains the results

$$T_3 = -ik_o u_{oz}\left(\cos\theta_o\, \bar{c}_{13} + \bar{c}_{31} \tan^2\theta_o\right) \quad , \tag{4-3}$$

and $\bar{c}_{33} = c_{33}(1 + e_{z3}^2/\epsilon_{zz}^S c_{33})$ and $\bar{c}_{31} = c_{31}(1 + e_{z3}e_{z1}/c_{31}\epsilon_{zz}^S)$, and

$$E_z = \frac{ik_o u_{oz} \cos\theta_o\, e^{-ik_o z\cos\theta_o}}{\epsilon_{zz}^S}(e_{z3} + e_{z1}\tan^2\theta_o) \tag{4-4}$$

where it is assumed that e_{x3} is zero as in the case of ferroelectric ceramics. Integration of Eq. (4-4) across the transducer gives the

voltage in terms of u_{oz}, or

$$V = \int_0^{\ell} E_z dz = \frac{i2u_{oz} e^{-i(k_o \ell/2)\cos\theta_o}}{\epsilon_{zz}^S} \sin\left(\frac{k_o \ell}{2}\cos\theta_o\right) \times (e_{z3} + e_{z1}\tan^2\theta_o) \qquad (4\text{-}5)$$

Taking u_z and T_3 continuous at the interface, the transmission coefficient can be obtained and the induced voltage V expressed in terms of the particle velocity amplitude of a plane wave entering the array at incident angle θ_i. Equation (4-5) then becomes

$$V = \frac{2\pi e_{z3} v_i}{\omega_o \epsilon_{zz}^S} \left[\frac{\cos\theta_i[\cos^2\theta_o + (e_{z1}/e_{z3})\sin^2\theta_o]}{\cos\theta_o + (Z_T/Z_W)\cos\theta_i[\cos^2\theta_o + (\bar{c}_{13}/\bar{c}_{33})\sin^2\theta_o]}\right] \times \frac{\sin[(\pi/2)(\omega/\omega_o)\cos\theta_o]}{(\pi/2)(\omega/\omega_0)\cos\theta_o} \exp\left[-i\left(\frac{\pi}{2}\frac{\omega}{\omega_o}\cos\theta_o\right)\right] \qquad (4\text{-}6)$$

where Z_T is the transducer impedance, Z_W the impedance of water, and θ_i and θ_o are related by Snell's Law.

Inspection of Eq. (4-6) shows that $|V|$ is zero where $\tan^2\theta_o = e_{z3}/e_{z1}$ since e_{z1} is negative in piezoelectric ceramics. If e_{z1} were zero, the zero in $|V|$ would occur at $\theta_c = 90^\circ$ which is the longitudinal critical angle. For nonzero e_{z1}, the zero in $|V|$ occurs for values of θ_c less than 90° or equivalently for angles of incidence less than the longitudinal critical angle. In PZT-5A, the zero occurs at $\theta_i = 17.3^\circ$, about 3° less than the critical angle of 20.2°. The voltage

is a maximum near $k_o \ell \cos \theta_o = \pi$ or $\cos \theta_o = \omega_o/\omega$. Thus, for $\omega > \omega_o$, the response rises to a maximum as θ_i increases from zero and then falls to zero near the critical angle.

A more complete theory taking into account shear waves has been developed,[18,53] and the results programmed for calculation on a digital computer. The program can take a large number of layers of isotropic materials of various acoustic properties so that multiple quarter wave matched and backed arrays can be evaluated. The general results in Eq. (4-6) are borne out by this more complicated theory as seen in Fig. 4-2. The theoretical angular and frequency dependence for a monolithic array element is shown in Fig. 4-3. This transducer is assumed to be backed with tungsten-loaded epoxy of impedance $22(10)^6$ and longitudinal velocity $1.46(10)^6$, where the ceramic is PZT-5A (see Table 3-2), and radiating directly into water. From the figure one can see that broad angle operation up to $\pm 15^o$ acceptance angle can be obtained over a 50% bandwidth.

C. EXPERIMENTAL RESULTS WITH BACKED MONOLITHIC ARRAYS

A five-element test array was constructed by soldering 1.092 mm (2 MHz) thick PZT-5A onto a thick lead backing. The array elements were constructed by depositing 38 mm long, 0.279 mm wide Cr-Au electrodes on 1.524 mm centers onto the face of the ceramic slab. The angular dependence of each element was measured, and the relative output power is compared to the theoretical result at one frequency in Fig. 4-4. The width of the element electrode is chosen to be small compared to a wavelength at 2.7 MHz ($1.35\ f_o$) so that the angular response is unaffected by the phase variation across the width of the electrode. Good agreement

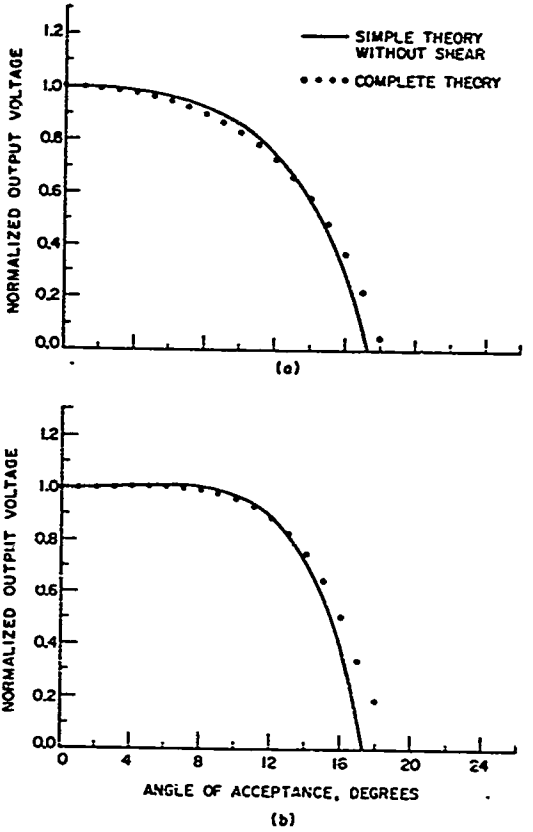

FIG. 4-2. Comparison of theoretical angular responses of a monolithic array element.

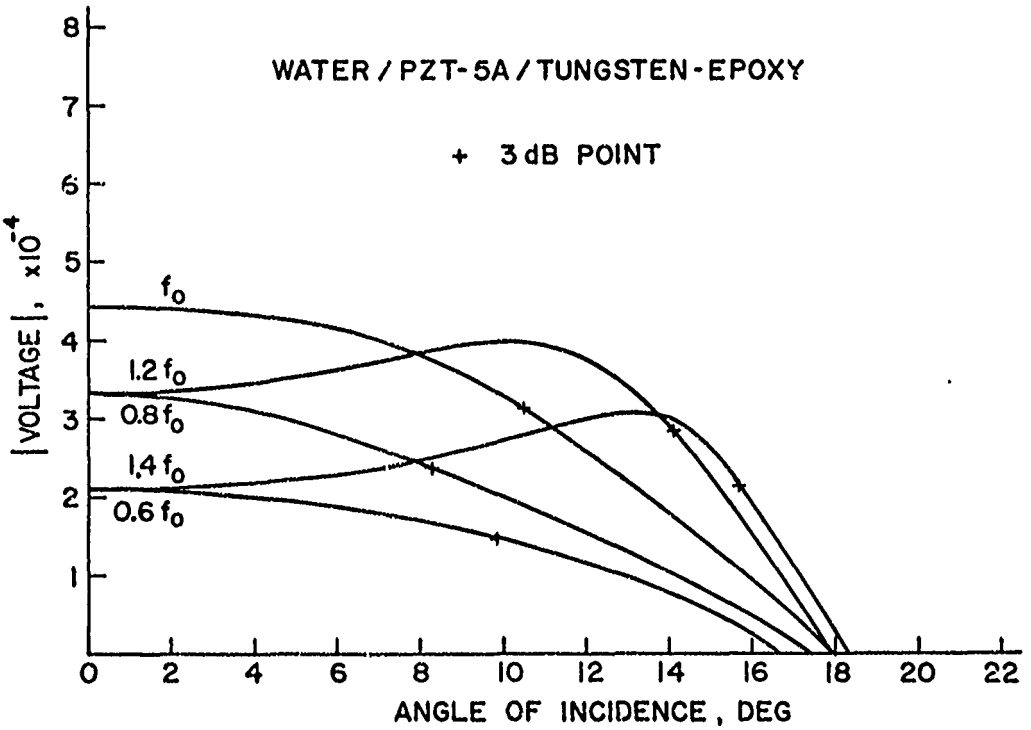

FIG. 4-3. Theoretical angular dependence of a water/PZT-5A/tungsten-epoxy assembly.

between theory and experiment can be seen in Fig. 4-4. The measured response, however, has a pronounced peak at 0° incidence which is caused by coupling to the adjacent unelectroded ceramic. The peaks at $\pm 26^{\circ}$ are the result of coupling to shear waves beyond the longitudinal critical angle. This effect occurs in all monolithic arrays and yields a beam pattern that is unacceptable in most imaging systems where the load is water. In the next section, a method for eliminating these large peaks beyond θ_c^l for water-loaded ceramic arrays will be discussed.

In Fig. 4-5 the effect of grounding the adjacent elements can be seen for the test array element in Fig. 4-4. It can be seen that the angular response of the transducer is greatly affected by this simple procedure and that it more closely approximates the point response theory discussed in the previous section. The small size of the peaks in the angular response beyond θ_c^l in Fig. 4-5 is attributed to the coupling to the adjacent ungrounded ceramic. Spacing of grounded areas around a monolithic element appears to change the angular response of these peaks in a complicated manner. Grounding the entire region around the element results in a dramatic change in the angular response, as can be seen in Fig. 4-6. In this figure, the angular response of an element from a 60-element tungsten-epoxy backed 2 MHz monolithic array is shown for normalized frequencies $f/f_o = 1$ and $f/f_o = 1.25$. The adjacent area is grounded. The large peaks beyond θ_c^l are due to excitation of shear and Rayleigh waves and is predicted by the complete numerical theory. The dip between the peaks corresponds to the shear-longitudinal critical angle θ_c^s. The small peak at 0° is due to some capacitive pickup not affected by the adjacent grounded area. The large peaks in the angular response make this sort of array useless in most imaging systems. A

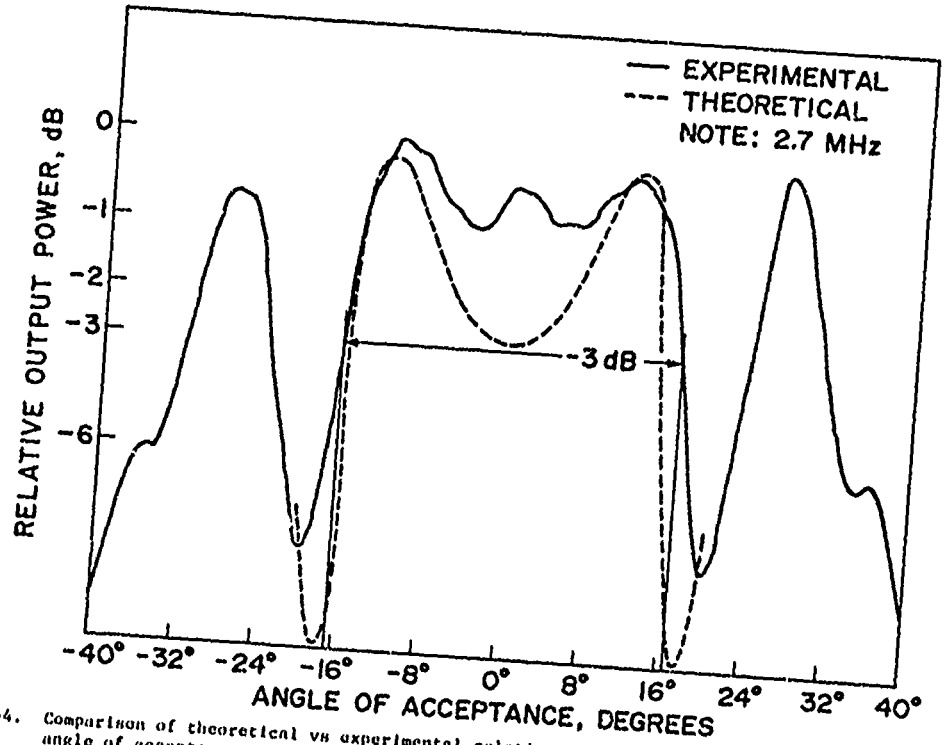

FIG. 4-4. Comparison of theoretical vs experimental relative output power P(0) as a function of angle of acceptance. Element size is 0.279 mm wide x 3.81 cm long. Test array is built of 1.092 mm thick lead-backed PZT-5A with 1.524 mm element spacing.

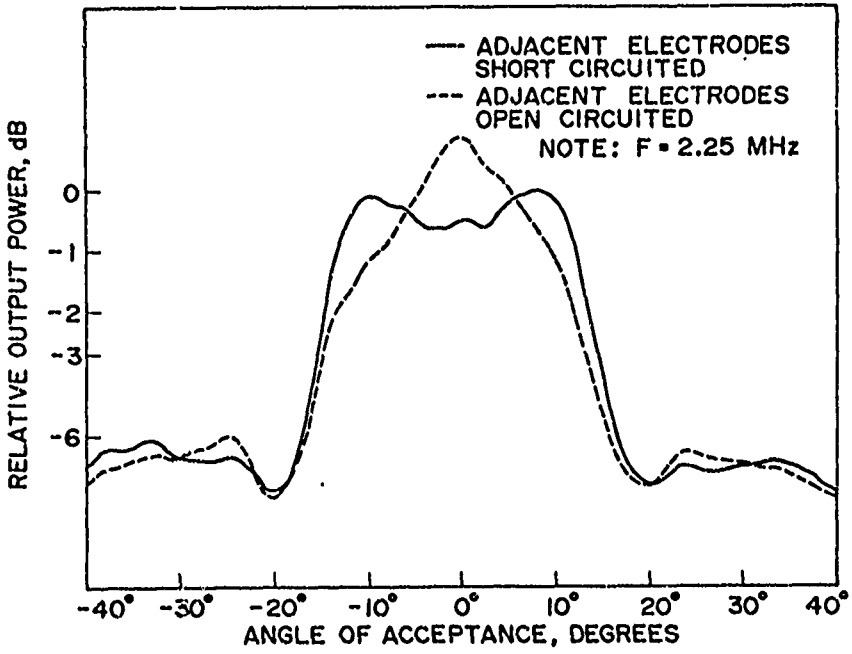

FIG. 4-5. Effect of grounding out adjacent elements on the relative output power P(θ) as a function of angle of acceptance of monolithic test array element. Same dimensions as Fig. 4-3.

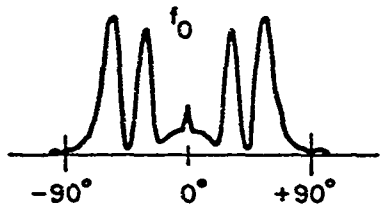

(a)

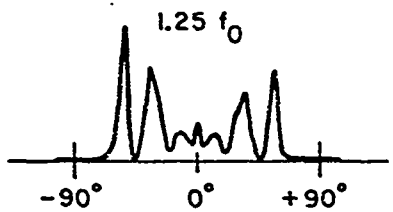

(b)

ANGLE OF ACCEPTANCE, DEGREES

FIG. 4-6. Angular response of tungsten-epoxy backed 2 MHz monolithic array elements with adjacent ceramic grounded:
(a) $f/f_o = 1$,
(b) $f/f_o = 1.25$.

solution to this problem is to introduce an angular filter into the transducer design to cut off the response beyond θ_c^L or use a lower velocity piezoelectric material. These approaches will be discussed in the next sections.

The bandwidths of the monolithic test array elements reported here are 50% as expected from the simple impedance matched transducer theory. However, a good match between theory and experimental results for the electrical impedance was not obtained from the simple point response. The electrical impedance of a test array element is shown in Fig. 4-7. The flatness of the impedance characteristics is excellent and is much flatter than expected from the simple transducer theory.

D. ELIMINATION OF ANGULAR RESPONSE BEYOND LONGITUDINAL CRITICAL ANGLE

As seen in the last section, monolithic transducer arrays made from high velocity piezoelectric ceramics radiating into a low velocity load such as water have large peaks in the angular response beyond the longitudinal critical angle. These peaks are the result of excitation of shear and Rayleigh waves in the ceramic and they are undesirable in most imaging systems. One method of eliminating these peaks is suggested here which employs another material acting as an angular filter located between the load and the ceramic whose properties are chosen so that the response beyond the longitudinal critical angle is cut off. Such an angular filter might also be used to eliminate system grating lobes as well. Ideally, this material would have nearly the same impedance as the ceramic so as not to greatly affect the overall transducer response, or the impedance could

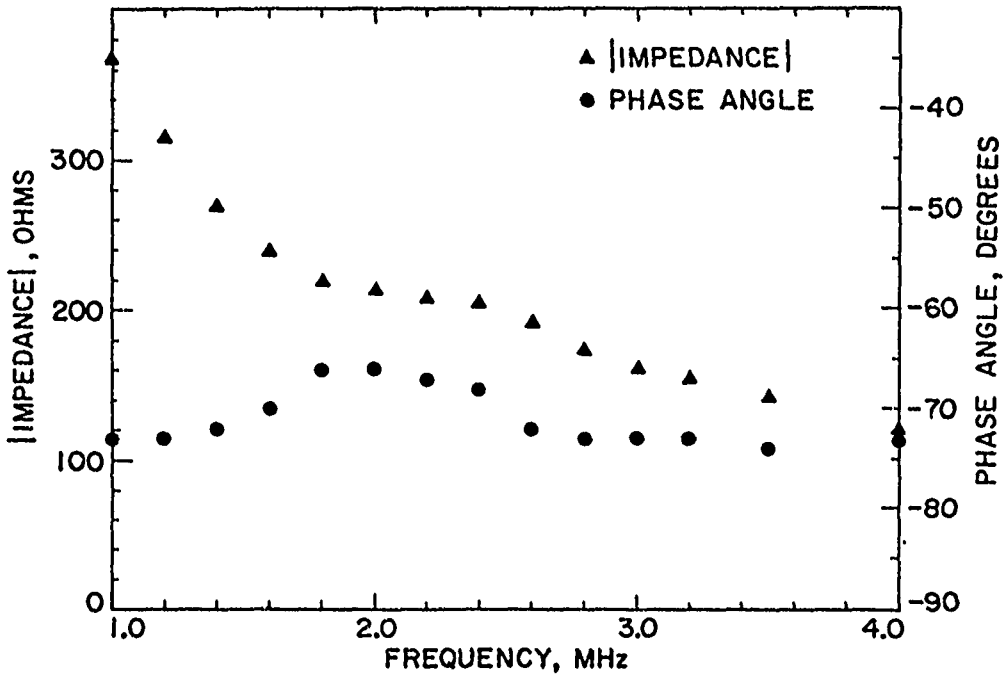

FIG. 4-7. Experimental electrical impedance of monolithic test array element. Same dimensions as Fig. 4-3.

be chosen to be the first layer of a set of quarter-wave matching layers. The angular filtering property would be achieved by choosing the material which has wave velocity much greater than the load longitudinal velocity. The angular filter would then have small longitudinal and shear critical angles, and very little response would be induced in the ceramic beyond the ceramic to load longitudinal critical angle. Ideally, V_ℓ and V_s of the angular filter would be nearly equal so that the response would fall off for both waves at about the same angle. In the angular filter beyond the cutoff angles, the field amplitude will fall-off across the filter as $\exp(-|k_x^{\ell,s} y|)$ where

$$k_z^\ell = \omega\left[\left(\frac{\sin\theta_i}{V_w}\right)^2 - \frac{1}{V_\ell^2}\right]^{1/2}$$

and

$$k_z^s = \omega\left[\left(\frac{\sin\theta_i}{V_w}\right)^2 - \frac{1}{V_s^2}\right]^{1/2} . \qquad (4\text{-}8)$$

The thickness of the plate should be chosen so that these amplitudes are small at the filter/ceramic boundary.

A simple case is a PZT-5A monolithic array with a matched backing. The theoretical angular response of an element is shown in Fig. 4-8 for several frequencies. The large nonuniform response beyond $\theta = 18^\circ$ is evident. An excellent choice for an angular filter in this case is magnesium oxide (MgO, $Z_\ell = 34(10)^6$, $V_\ell = 8.85(10)^6$, $V_s = 6.37(10)^6$). The impedance of MgO is almost identical to that of PZT-5A, and the velocities are very high and close to each other. The critical angles are $\theta_c^\ell = 9.6^\circ$ and $\theta_c^s = 13.4^\circ$. The angular point response of the

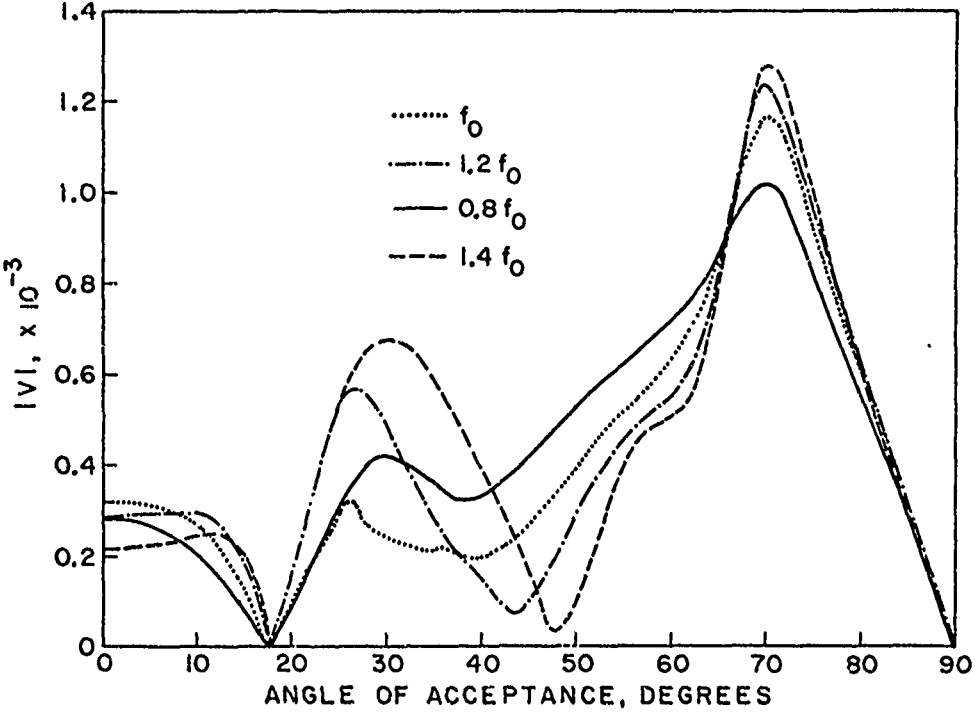

FIG. 4-8. Theoretical angular response of PZT-5A monolithic array element with a $Z = 25(10)^6$ backing.

filtered monolithic transducer is shown in Fig. 4-9 for several values of MgO thickness at the half-wave resonant frequency. The exponential decay from the angular filter is evident in all cases. The best choice of thickness appears to be about one-third the resonant frequency wavelength. Below this, the decay is not rapid enough to eliminate some of the peakiness beyond the critical angle; and above this, the decay from the longitudinal cutoff is too rapid which introduces new peaks for $\theta < \theta_c^l$. A major problem, of course, with this kind of transducer is that if a layer as thick as $\lambda/3$ is applied on top the ceramic, the transducer will tend to resonate at 0.50 f_o and 1.10 f_o, yielding a double humped bandshape and concomitant non-ideal impuse response. The application of this type of transducer would be extremely limited.

Another possibility for a monolithic array is the use of quarter-wave matching layers where one of the matching layers with a high longitudinal velocity acts as an angular filter. One such design was pursued theoretically using silicon ($Z_l = 19.7(10)^6$, $V_l = 8.43(10)^6$, $V_s = 5.84(10)^6$) as the first of three quarter-wave plates. The other layer materials were a tungsten-epoxy composite ($Z_i = 7(10)^6$) and polystyrene ($Z_i = 2.4(10)^6$). The theoretical angular acceptance of this arrangement is shown in Fig. 4-10 for several frequencies. Angular cutoff is achieved, but the $\lambda/4$ thickness of the silicon necessary for optimal transducer response does not allow the fields to die off fast enough when $\theta > \theta_c^l$ to prevent some peakiness. In addition, V_l and V_s for silicon are far enough apart so that the decays from the two shear and longitudinal filter cutoffs are not coincident enough to prevent peakiness inside θ_c^l. Finding a suitable material to act

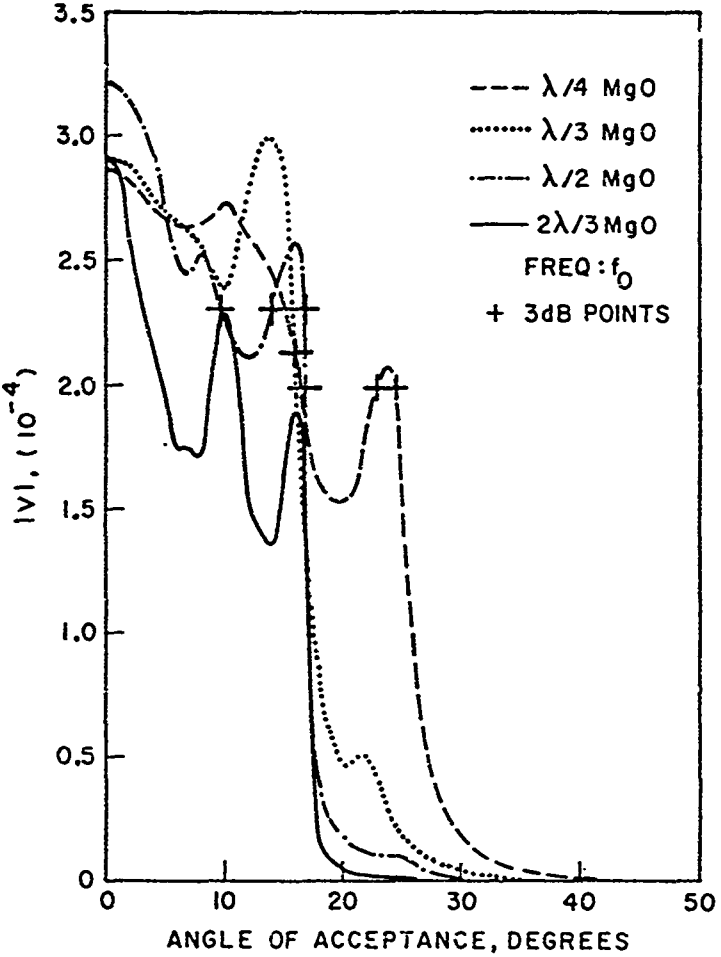

FIG. 4-9. Theoretical angular response of PZT-5A monolithic array element with MgO angular filter with a Z = 25(10)^6 backing.

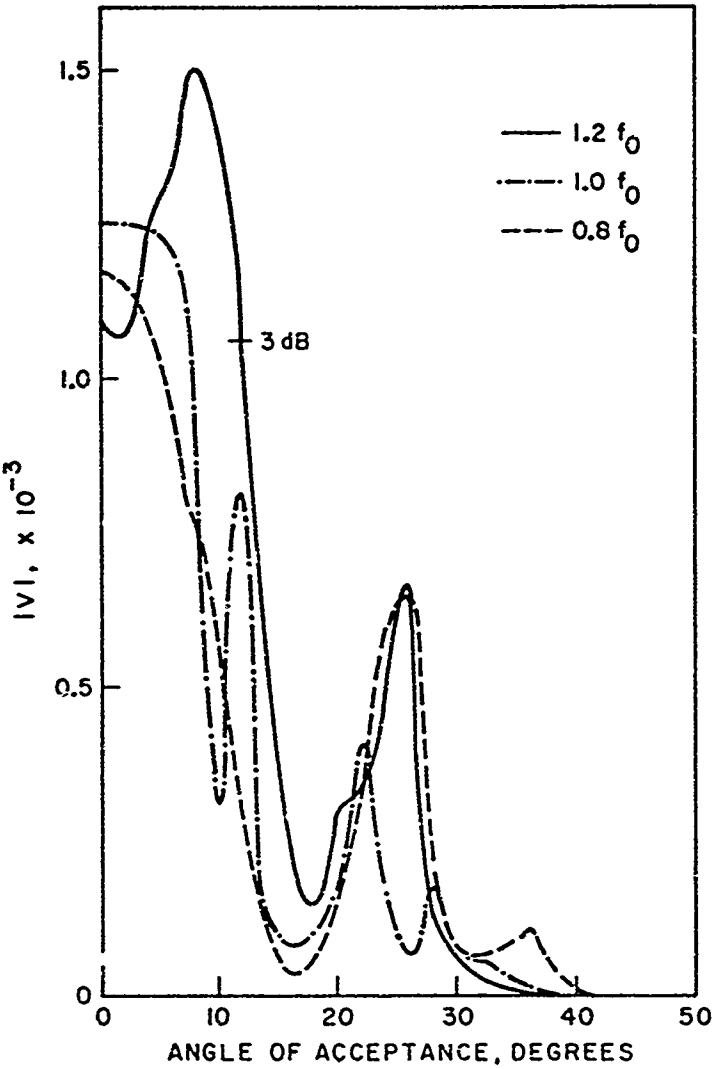

FIG. 4-10. Theoretical angular response of three-layer quarter-wave matched PZT-5A monolithic array element using silicon as an angular filter and first matching layer.

as both matching layer and angular filter is a formidable, if not impossible, task. An array of this nature would be difficult then to implement in practice.

E. PVF_2 MONOLITHIC ARRAYS

As mentioned in previous sections, large differences in longitudinal velocities between the piezoelectric section of the transducer and the load medium will cause a zero in the angular response at the longitudinal critical angle at angles like 15° for PZT-5A and water. In addition, large peaks in the angular response beyond this point result from coupling to shear waves in the transducer. These effects can be reduced by using a piezoelectric/load configuration where the longitudinal velocities are similar and where the shear wave impedances of the two media are fairly close.

One structure of interest uses PVF_2 as the piezoelectric, backed with a high impedance material like brass, radiating into water.[32] The longitudinal wave cutoff is 44° as mentioned earlier. The transducer would operate near a quarter-wave resonance in this case, however, since the PVF_2 is terminated at the back essentially by an infinite backing impedance. As shown in Fig. 4-11, the theoretical angular response of this transducer is plotted for thicknesses of 0.2 and 0.3 of the acoustic wavelength in PVF_2. The coupling constant e_{13} was taken to be zero in these computations, although in fact it is quite large. Later computations including e_{13} and shear wave loss have been made by Shaw, Weinstein, and Drake.[56] As can be seen, the angular response is broader than the case of ceramic and

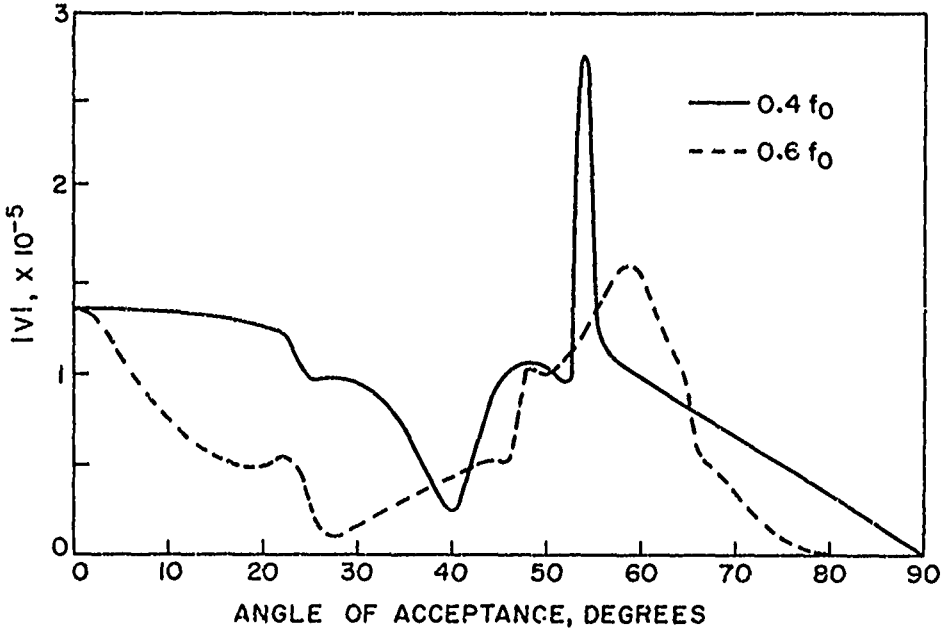

FIG. 4-11. Theoretical angular response of monolithic PV^2_2 array element backed with brass radiating into water. Note that transducer operates at quarter-wave resonance in this case.

water, but not as broad as expected. In addition, there are large peaks in the angular response beyond θ_c^2 due to the mismatch of the shear wave in PVF_2. This effect may be largely reduced in practice since PVF_2 is probably very lossy to shear waves. The theoretical point response program does not include any loss. If these peaks are reduced in practice, then one would expect an acceptance angle of 30° for $f = 0.4\ f_o$ and only 7° for $f = 0.6\ f_c$. This low angular acceptance was not expected and may result from operation of the transducer near the quarter-wave resonance with a reflecting backing instead of at a half-wave resonance. The calculations in Reference 56 show that the large negative value of e_{13} does reduce the angular acceptance by reducing the received signal in the regime beyond the small peak at 22°. The very strong peak in the beam pattern at 54° is considerably reduced by introducing high shear wave loss, however. It is evident that much more work is needed to build [illegible]nolithic transducer arrays with large angular acceptance.

F. CERAMIC ON METAL MONOLITHIC ARRAYS

An important application of monolithic transducer arrays lies in the area of nondestructive testing. In this case, images of flaws can be produced by directly coupling the acoustic energy generated by the transducers into the sample to be imaged instead of using an intervening low impedance coupling medium like water. A longitudinal or shear wave array of high velocity ceramic like lead zirconate titanate can be directly coupled into a sample or attached to a buffer material which is then directly coupled to the sample. The advantage of this technique is twofold. First, since many of the typical materials of

interest in nondestructive testing, such as steel, aluminum, and ceramics, have high impedances like that of piezoelectric ceramics, a high efficiency, broad bandwidth array can be easily produced without the use of quarter-wave matching layers. Also, since the acoustic velocities of these materials are as large or larger than those of the transducer material, there are no longitudinal-longitudinal or shear-shear critical angles, thus allowing broad, uniform spatial frequency responses for monolithic array elements.

To demonstrate the use of monolithic arrays for this purpose, a longitudinal monolithic array was constructed by epoxying a slab of PZT-5A ceramic onto an aluminum buffer block.

In the case where the load medium velocity is greater than that of the piezoelectric material, there is no longitudinal wave critical angle. Theoretical curves were computed for PZT-5A ceramic ($\bar{V}_l = 4.35(10)^6$) radiating into aluminum ($V_l = 6.3(10)^6$) and compared to experimental values for the same configuration. The experimental data were taken by epoxying a 0.500" × 0.031" slab of PZT-5A ceramic onto the edge of an aluminum plate 2" thick by the usual thin bonding technique. Sixty array elements were defined on the ceramic by etching away a 1 μm thick Cr-Au film on the top surface of the ceramic. The elements were 0.020" wide × 0.450" long and the area around the elements was left covered with gold and grounded to form a shield. The radiation pattern of the center element was determined by machining the plate in a cylindrical surface of 3" radius around the center of the array. A 3/4" diameter, 2 MHz thin disc transducer was bonded to a block of aluminum with a front surface matching that of the plate. The angular response was easily checked by moving the transmitting plane wave transducer around the surface and receiving the signal with the center monolithic

array element as a function of angle. The angular responses for $f = f_o$ and $f = 0.8\ f_o$ are shown in Figs. 4-12 and 4-13 and compared to theory. Excellent agreement between theory and experiment are demonstrated in these figures, and acceptance angles of 37^o and 33^o, respectively, are shown. Little evidence of excitation of shear waves is seen, although the small peaks in Figs. 4-12 and 4-13 at 40^o could be caused by this effect.

As can be seen from Figs. 4-12 and 4-13, excellent monolithic transducer arrays can be constructed for this important area of application in nondestructive testing. The excellent impedance match between metals and piezoelectric ceramics allows the simple construction of extremely efficient transducer arrays with 50 to 100% bandwidths depending on the exact properties of the metal and ceramic used. In addition, broad and uniform spatial frequency responses are automatically obtained since critical angle phenomena are eliminated. Monolithic arrays should become an important part of future nondestructive testing imaging systems.

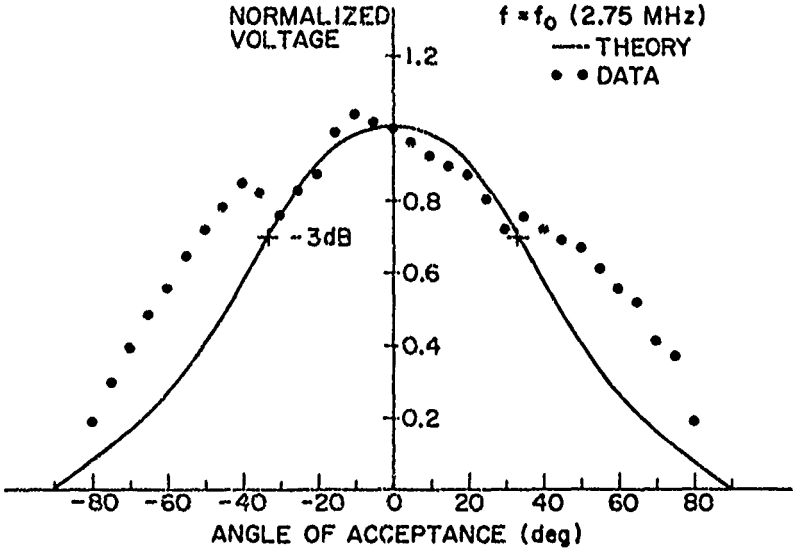

FIG. 4-12. Comparison of theoretical versus experimental angular response of air-backed PZT-5A array element radiating into aluminum at $f = f_o$.

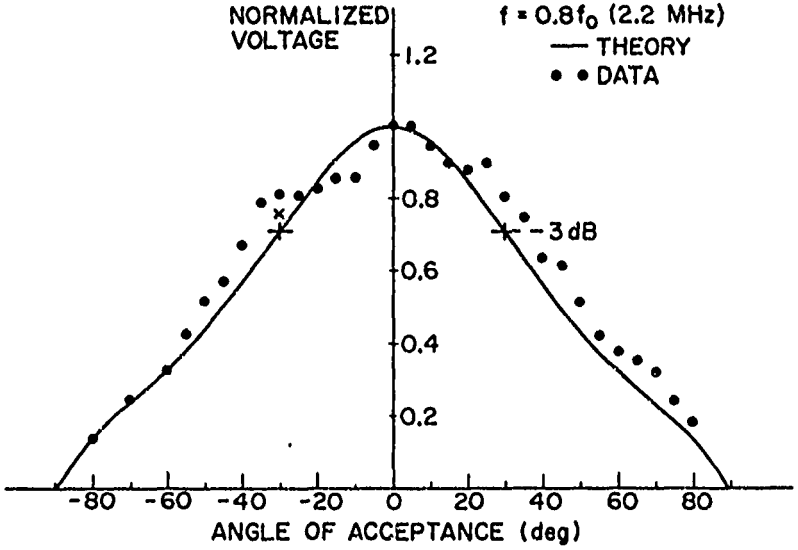

FIG. 4-13. Comparison of theoretical versus experimental angular response of air-backed PZT-5A array element radiating into aluminum at $f = 0.8\ f_o$.

APPENDIX A

PROOF OF THE VARIATIONAL FORM OF LOAD ADMITTANCE OF A NARROW SLOTTED TRANSDUCER ELEMENT

An expression for the effective admittance of a narrow slotted element radiating into an infinite half-space was derived in Section 3-D. In this appendix, it is shown that this expression, Eq. (3-58), is variational in form with respect to the assumed stress field $T_3(x)$. The expression for the admittance is

$$Y_1 = -\frac{\iint T_3^*(x)\, \mathcal{G}(x,x')\, T_3(x')\, dxdx'}{\int T_3 q_1^* dx \int T_3^* q_1 dx} \qquad (3\text{-}58)$$

By definition, (3-58) is variational in form if $\delta Y_1 = 0$ when $T_3(x)$ is changed only to first order. Taking the first order variation in Y_1, one obtains

$$\delta Y_1 = \left\{ \frac{-\iint (\delta T_3^*)\mathcal{G} T_3\, dxdx' - \iint T_3^* \mathcal{G}(\delta T_3)\, dxdx'}{\int T_3 q_1^* dx \int T_3^* q_1 dx} \right\}$$
$$- Y_1^o \left\{ \frac{\left[\int (\delta T_3) q_1^* dx \int T_3^* q_1 dx + \int T_3 q_1^* dx \int (\delta T_3^*) q_1\, dx \right]}{\int T_3 q_1^* dx \int T_3^* q_1 dx} \right\}$$

or

$$\left(\int T_3 q_1^* dx \int T_3^* g_1 dx \right) \delta Y_1 = -\left\{ \iint (\delta T_3^*)\, \mathcal{G} T_3 dxdx' + Y_1^o \int T_3 q_1^* dx \int (\delta T_3^*) q_1 dx \right\}$$
$$+ \left\{ \iint T_3^* \mathcal{G}(\delta T_3) dxdx' + Y_1^o \int (\delta T_3) q_1^* dx \int T_3^* q_1 dx \right\} \qquad (A\text{-}1)$$

From (3-51) and (3-56), it follows that if higher order modes are neglected, one obtains

$$\int T_3(x')\,\mathcal{G}(x,x')dx' = -\frac{\bar{q}_1}{Z_1}\int \bar{G}\cdot\vec{q}_1 dS = -\frac{q_1}{Z_1}\int T_3 q_1^* \, dx \quad \text{(A-2)}$$

and

$$\int\left(\delta T_3(x')\right)\mathcal{G}(x,x')dx' = -\frac{q_1}{Z_1}\int(\delta T_3)\, q_1^* dx \quad \text{(A-3)}$$

Substituting (A-2) and (A-3) into (A-1), one obtains for the right hand side of (A-1):

$$\text{RHS} = -\left\{\int\left(\delta T_3^*(x)\right)\left[-\frac{q_1}{Z_1}\int T_3 q_1^* dx\right]dx + Y_1^o\int T_3 q_1^* dx\int(\delta T_3^*)q_1 dx\right\}$$
$$+\left\{\int T_3^*(x)\left[-\frac{q_1}{Z_1}\int(\delta T_3)q_1^* dx\right]dx + Y_1^o\int(\delta T_3)q_1^* dx\int T_3^* q_1 dx\right\}$$

Since $(1/Z_1) \equiv Y_1^o$, all the terms in the above expression cancel out. Therefore $\delta Y_1 = 0$ and Eq. (3-58) is a variational expression for the load impedance of a narrow slotted element.

APPENDIX B

GREEN'S FUNCTIONAL FORM OF $V_z(\beta)$ FOR ISOTROPIC SOLIDS AND LIQUIDS

To evaluate the effective radiation admittance of a slotted transducer element, it is necessary to determine the Green's function expressed in Eq. (3-58). This is done as shown in Section 3-D by applying Parseval's theorem to the numerator of Eq. (3-59). The problem then is reduced to determining the functional form of $v_z(\beta)$ in terms of $T_3(\beta)$ for the cases where the load media are isotropic solids or liquids. These forms are determined in this appendix.

The loading or backing medium is taken to be isotropic which is the case for the backings employed in the transducer arrays. For an isotropic material, the acoustic fields can be derived from a scalar potential ϕ and a vector potential $\bar{\psi}$ as shown in Auld.[54] The velocity field is

$$\bar{v} = \nabla\phi + \nabla \times \bar{\psi} \quad , \tag{B-1}$$

where ϕ and $\bar{\psi}$ obey the wave equations

$$\begin{aligned} \nabla^2\bar{\psi} - (1/v_s^2)(\partial^2\bar{\psi}/\partial t^2) &= 0 \\ \nabla^2\phi - (1/v_l^2)(\partial^2\phi/\partial t^2) &= 0 \end{aligned} \tag{B-2}$$

Since it has been assumed that there is no y-dependence, Eqs. (B-1) become

$$\begin{aligned} v_x &= \partial\phi/\partial x - \partial\psi/\partial z \\ v_z &= \partial\phi/\partial z + \partial\psi/\partial x \end{aligned} \tag{B-3}$$

where $\psi \equiv \psi_y$.

Taking solutions of (B-2) of the form

$$\phi = A\, e^{-i\beta x}\, e^{-i\beta_\ell z}\, e^{i\omega t}$$

$$\psi = B\, e^{-i\beta x}\, e^{-i\beta_s z}\, e^{i\omega t} \qquad \text{(B-4)}$$

dispersion relations are easily found to be

$$\beta^2 + \beta_\ell^2 = k_\ell^2 = (\omega/V_\ell)^2$$

$$\beta^2 + \beta_s^2 = k_s^2 = (\omega/V_s)^2 \qquad \text{(B-5)}$$

Now,

$$T_3 = \lambda S_1 + (\lambda + 2\mu) S_3$$

$$T_5 = \mu S_5 \qquad \text{(B-6)}$$

where λ and μ are the Lamé constants, and

$$i\omega S_1 = \partial v_x/\partial x$$

$$i\omega S_3 = \partial v_z/\partial z \qquad \text{(B-7)}$$

$$i\omega S_5 = \partial v_x/\partial z + \partial v_z/\partial x \quad .$$

Substituting (B-3) and (B-7) into (B-6), one gets for the stresses at the boundary ($z = 0$) :

$$T_3 = -\frac{1}{i\omega}\left\{\left[\lambda(\beta^2+\beta_l^2)+2\mu\beta_l^2\right]A + (2\mu\beta_s\beta)B\right\}e^{i(\omega t-\beta x)} \qquad \text{(B-8)}$$

$$T_5 = -\frac{\mu}{i\omega}\left[(2\beta\beta_l)A + (\beta^2-\beta_s^2)B\right]e^{i(\omega t-\beta x)} \qquad \text{(B-9)}$$

Since we have taken $T_5 = 0$ at the boundary, the ratio of B/A is found from (B-9) and substituted into (B-8). The result is

$$T_3 = -\frac{1}{i\omega}\left\{\lambda(\beta^2+\beta_l^2)+2\mu\left[\beta_l^2+\frac{\beta_l\beta^2}{\beta_s^2-\beta^2}\right]\right\}A \qquad \text{(B-10)}$$

where the harmonic dependence has been suppressed. Now it is easily shown that

$$\mu = \frac{k_l^2}{k_s^2-2k_l^2}\lambda \quad . \qquad \text{(B-11)}$$

Substituting Eqs. (B-5) into (B-11) yields

$$\mu = \frac{\beta^2+\beta_l^2}{\beta_s^2-\beta^2-2\beta_l^2}\lambda \quad . \qquad \text{(B-12)}$$

Substituting (B-12) into (B-10) then yields

$$T_3 = -\frac{\mu A}{i\omega}\left(\frac{1}{\beta_s^2-\beta^2}\right)\left\{(\beta_s^2-\beta^2)^2+4\beta_s\beta_l\beta^2\right\} \qquad \text{(B-13)}$$

where the quantity in brackets is recognized as the Rayleigh wave dispersion relation.

From Eqs. (B-3) and (B-4), it is easily shown that

$$v_z = -i\beta_l \left[\frac{\beta^2 + \beta_s^2}{\beta_s^2 - \beta^2} \right] A \qquad (B\text{-}14)$$

From Eqs. (B-13) and (B-14), $v_z(\beta)$ can be expressed in terms of $T_3(\beta)$

$$v_z(\beta) = -\left(\frac{\omega \beta_l}{\mu}\right) \frac{\beta_l^2 + \beta_s^2}{\left[(\beta_s^2 - \beta^2)^2 + 4\beta_s \beta_l \beta^2\right]} T_3(\beta) \qquad (B\text{-}15)$$

In the case where the load medium is water, another relation is derived in a similar manner to (B-15). Since liquids can't support shear waves, the medium is simply described by a scalar porential. Thus

$$T_3 = \lambda(\epsilon_1 + \epsilon_3)$$

$$= \frac{\lambda}{i\omega}\left(\frac{\partial v_x}{\partial x} - \frac{\partial v_z}{\partial z}\right)$$

$$= \frac{\lambda}{i\omega}\left(\frac{\partial^2 \phi}{\partial x^2} + \frac{\partial^2 \phi}{\partial z^2}\right)$$

$$= -\frac{\lambda}{i\omega}(\beta^2 + \beta_l^2)A$$

$$T_3 = -\frac{\lambda k_l^2}{i\omega} A \quad . \qquad (B\text{-}16)$$

But

$$v_z = \frac{\partial \phi}{\partial z} = -i\beta_l A \ ,$$

or

$$v_z(\beta) = -\frac{\omega \beta_l}{k_l^2} T_3(\beta) \quad . \qquad (B\text{-}17)$$

APPENDIX C

INTEGRATION OF THE VARIATIONAL EXPRESSION FOR THE RADIATION IMPEDANCE OF A SLOTTED ELEMENT

The method of integrating Eq. (3-64) is shown in this appendix and is identical to that of Miller and Pursey.[40] Since the integrand of (3-64) is symmetric, the integral $\int_{-\infty}^{\infty} d\beta$ becomes $2\int_{C}^{\infty} d\beta$. Using a normalized variable $\xi = \beta/k_s$, making use of Eqs. (B-5), and noting $\omega/v = (k_\ell^2/k_t Z_\ell)$, (3-64) can be then written

$$Y_1 = \frac{k_s d}{\pi a Z_\ell}\int_0^{\infty} \frac{\sqrt{a^2-\xi^2}}{\left[(1-2\xi^2)^2 + 4\xi^2\sqrt{1-\xi^2}\sqrt{a^2-\xi^2}\right]} \left(\frac{\sin(k_s d/2)\xi}{(k_s d/2)\xi}\right)^2 d\xi \qquad (C\text{-}1)$$

where $a^2 = (V_s/V_\ell)^2 = \frac{2\sigma-1}{2(\sigma-1)}$ and σ is Poisson's ratio.

The contributions to Y_1 can be divided into three regimes as shown in Fig. (C-1). In the regime $0 \le \xi < a$, the contribution is entirely real and corresponds to power being carried away by both longitudinal and shear waves. From the branch cut at $\xi = a$ to the branch cut at $\xi = 1$, the contribution is both real, from shear waves, and imaginary, from evanescent longitudinal waves. From $\xi = 1$ to $\xi = \infty$, the contribution is entirely imaginary, arising from evanescent longitudinal and shear waves except at the pole ξ_R. The contribution from the pole at $\xi = \xi_R$ corresponds to power radiated into the Rayleigh wave.

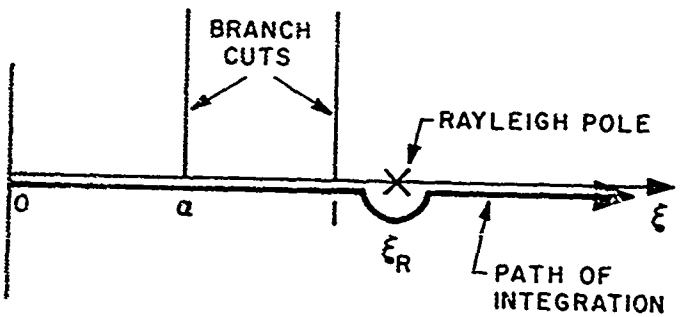

FIG. C-1. Schematic drawing of path of integration used to calculate the integral in Eq. (3-65).

The integral in (C-1) was directly integrated numerically on a mini-computer using an 8-point Newton-Cotes algorithm for various values of Poisson's ratio and element width. The path of integration was taken along the real axis taking the physically meaningful branches of the integrand at the branch cuts. The first branch cut occurs at $\xi = \alpha$ and the second at $\xi = 1$. These points are where $\beta_i = \sqrt{k_i^2 - \beta^2} = 0$ and $\beta_s = \sqrt{k_s^2 - \beta^2} = 0$. Since the physically meaningful solution for $\beta > k_i$ and $\beta > k_s$ occurs when the waves are evanescent, the proper signs on the square roots are negative, that is

$$e^{-i\beta_{i,s}z} = \exp\left(-i\left[-i\sqrt{\beta^2 - k_{i,s}^2}\right]z\right)$$

$$= \exp\left[-\sqrt{\beta^2 - k_{i,s}^2}\right]z \qquad \text{(C-2)}$$

$$\beta > k_{i,s}$$

Therefore Eq. (C-1) for $\alpha \leq \xi < 1$,

$$Y_1 = -\frac{ik_s d}{\pi \alpha Z_i} \int_\alpha^1 \frac{\sqrt{\xi^2 - \alpha^2}}{\left[(1-2\xi^2)\right]^2 - 4i\xi^2\sqrt{1-\xi^2}\sqrt{\xi^2-\alpha^2}} \left(\frac{\sin(k_s d/2)\xi}{(k_s d/2)\xi}\right)^2 d\xi$$

(C-3)

For the regime $1 \leq \xi < \infty$,

$$Y_1 = -\frac{ik_s d}{\pi \alpha Z_i} \int_\alpha^1 \frac{\sqrt{\xi^2 - \alpha^2}}{\left[(1-2\xi^2)\right]^2 - 4\xi^2\sqrt{\xi^2-1}\sqrt{\xi^2-\alpha^2}} \left(\frac{\sin(k_s d/2)\xi}{(k_s d/2)\xi}\right)^2 d\xi$$

(C-4)

The Rayleigh pole occurs at $\xi = \xi_R$ where

$$F(\xi_R) = \left[1 - 2\xi_R^2\right]^2 - 4\xi_R^2 \sqrt{\xi_R^2 - 1}\sqrt{\xi_R^2 - \alpha^2} = 0 \quad . \qquad \text{(C-5)}$$

Since the Rayleigh wave velocity V_R is always less than V_s, $\xi_R > 1$. The path of integration is taken around the top half of a circle of radius r centered at $\xi = \xi_R$ as shown in Fig. (C-1). The contribution at the pole is determined from the theorem

$$\text{If} \quad \lim_{z \to a} (z - a)\, G(z) = a_{-1} \quad ,$$

$$\int_{\substack{\lim \\ r \to 0}} G(z)dz = -\pi i\, a_{-1} \quad ,$$

where a_{-1} is the residue of the pole. $G(z)$ is the integrand of (C-4); therefore

$$a_{-1} = \sqrt{\xi_R^2 - \alpha^2} \left(\frac{\sin(k_s \xi_R d/2)}{(k_s \xi_R d/2)}\right)^2 \lim_{\xi \to \xi_R} \frac{(\xi - \xi_R)}{F(\xi)} \qquad \text{(C-6)}$$

The limit in (C-6) has been carried out by Viktorov[55] and can be directly calculated by evaluating $(dF/d\xi)^{-1}_{\xi_R}$. The contribution to the admittance from the Rayleigh pole is found to be

$$(Y_1)_R = \frac{k_s d}{4\alpha Z_1} \left\{ \frac{(\xi_R^2 - \alpha^2)\sqrt{\xi_R^2 - 1}}{2\xi_R(1 - 2\xi_R^2)\sqrt{\xi_R^2 - \alpha^2}\sqrt{\xi_R^2 - 1} + 4\xi_R^5 - 3\xi_R^3(1 + \alpha^2) + 2\xi_R\alpha^2} \right\}$$

$$\left(\frac{\sin(k_s d/2)\,\xi_R}{(k_s d/2)\,\xi_R}\right)^2 , \qquad \text{(C-7)}$$

and

$$\mathrm{Re}\{Y_1\} = \int_0^a + \mathrm{Re}\int_a^1 + (Y_1)_R \qquad \text{(C-8)}$$

The imaginary part is simply

$$\mathrm{Im}\{Y_1\} = \mathrm{Im}\int_a^i + \int_1^{R\to\infty} \qquad \text{(C-9)}$$

A little care must be exercised in evaluating the second integral in (C-9) to avoid numerical problems near the Rayleigh pole. For a simple pole, the Laurent series near the pole is

$$F(\xi) = \frac{a_{-1}}{\xi - \xi_R} + a_0 + a_1(\xi - \xi_R) + \ldots \qquad \text{(C-10)}$$

where a_{-1} is the residue. For $\delta = (\xi - \xi_R)$ small, the first-order and higher terms can be neglected. The integral is then taken in sections $1 \le \xi \le \xi_R - \delta$ and $\xi_R + \delta \le \xi \le R$ where R and δ are chosen to meet an arbitrary accuracy. In the regime $(\xi_R - \delta) \le \xi \le (\xi_R + \delta)$, the integral is simply $2\delta a_0$.

REFERENCES

1. Born, N., et al., "Multiscan Echocardiology," Circulation 48, pp. 1066-1074 (November 1973).
2. Somer, J. C., "Electronic Sector Scanning for Ultrasonic Diagnosis," Ultrasonics 6(3), pp. 153-159 (1968).
3. Thurstone, F. L., and von Ramm, O. T., "A New Ultrasound Imaging Technique Employing Two-Dimensional Beam Steering," Acoustic Holography, Vol. 5. Plenum Press, New York, 1972, pp. 249-259.
4. Green, P.S., et al., "A New High-Performance Ultrasonic Camera," Acoustic Holography, Vol. 5, op. cit., pp. 493-503.
5. Fenner, W. R., and Stewart, G. E., "An Ultrasonic Holographic Imaging System for Medical Applications," ibid., pp. 481-492.
6. Havlice, J. F., et al., "A New Acoustic Imaging Device," IEEE Ultrasonics Symp. Proc., November 1973, pp. 13-18.
7. Cook, R. L., "Experimental Investigation of Acoustic Imaging Sensors," IEEE Trans. on Sonics and Ultrasonics SU-19 (4) (October 1972).
8. Takagi, N., et al., "Solid-State Acoustic Image Sensor," Acoustic Holography, Vol. 4. op. cit., pp. 215-236.
9. Harrold, S. O., "A Solid-State Ultrasonic Image Converter," Dept. of Electrical Engineering, Portsmouth Polytechnic, Portsmouth, England, November 1972.
10. Magginess, M. G., Plummer, J. D., and Meindl, J. D., "An Acoustic Image Sensor Using a Transmit-Receive Array," Acoustic Holography, op. cit., pp 619-631.

11. Burckhardt, C. B., et al., "Focusing Ultrasound Over a Large Depth of Field with an Annular Transducer — An Alternative Method," IEEE Trans. on Sonics and Ultrasonics SU-22, (January 1975), pp. 11-15.

12. Vilkomerson, D., "Acoustic Imaging with Thin Annular Apertures," Acoustic Holography, Vol. 5, Plenum Press, New York, 1972, pp. 283-316.

13. Macovski, A., and Norton, S., "High Resolution B-scan Systems Using a Circular Array," Acoustic Holography, Vol. 6, Plenum Press, New York, 1975, pp. 121-143.

14. Fraser, J., et. al., "A Two-Dimensional Electronically Focused Imaging System," IEEE Ultrasonics Symp. Proc., November 1974, pp. 19-23.

15. Waugh, T. M., Kino, G. S., DeSilets, C. S., and Fraser, J. D., "Acoustic Imaging Techniques for Non-destructive Testing," IEEE Trans. on Sonics and Ultrasonics, SU-23 (5) (September 1976), pp. 313-317.

16. Kossoff, G., "The Effects of Backing and Matching on the Performance of Piezoelectric Ceramic Transducer," IEEE Trans. on Sonics and Ultrasonics SU-13 (March 1966), pp. 20-30.

17. Reeder, T. M., and Winslow, D. K., "Characteristics of Microwave Acoustic Transducers for Volume Wave Excitation," IEEE Trans. MTT-17, (1969), pp. 927-941.

18. Auld, B. A., Drake, M. E., Roberts, C. G., "Monolithic Acoustic Imaging Transducer Structures with High Spatial Resolution," Appl. Phys. Letters 25 (9) (1 November 1974), pp. 478-479.

19. Auld, B. A., DeSilets, C. S., and Kino, G. S., "A New Acoustic Array for Acoustic Imaging," IEEE Ultrasonics Symp. Proc., November 1974, pp. 24-27.

20. Mason, W. P., Electromechanical Transducers and Wave Filters, (Van Nostrand, Princeton, N.J., 1948).

21. Goll, J., and Auld, B. A., "Multilayer Impedance Matching Schemes for Broadbanding of Water Loaded Piezoelectric Transducers and High Q Resonators," IEEE Trans. on Sonics and Ultrasonics, SU-22 (January 1975), pp. 53-55.

22. Goll, J. (unpublished).

23. Krimholtz, R., Leedom, D., and Matthaei, G., "New Equivalent Circuits for Elementary Piezoelectric Transducers," Electronics Letters 6 (June 1970), pp. 398-399.

24. Leedom, D., Krimholtz, R., and Matthaei, G., "Equivalent Circuits for Transducers Having Arbitrary Even- or Odd-Symmetry Piezoelectric Excitation," IEEE Trans. on Sonics and Ultrasonics, SU-18 (July 1971), pp. 128-141.

25. DeSilets, C. S., Fraser, J. D., and Kino, G. S., "Design of Efficient, Broadband Transducers," to be published in IEEE Trans. on Sonics and Ultrasonics.

26. Ramo, Whinnery, Van Duzer, Fields and Waves in Communication Electronics, John Wiley and Sons, New York, 1965, pp. 613-619.

27. Collin, R. E., "Theory and Design of Wide-Band Multisection Quarter-Wave Transformers," Proc. IRE 43 (February 1955), pp. 179-185.

28. Riblet, H., "General Synthesis of Quarter-Wave Impedance Transformers," IRE Trans., MTT-5 (January 1957), pp. 36-43.

29. Young, L., "Tables for Cascaded Homogeneous Quarter-Wave Transformers," IRE Trans., MTT-7 (April 1959), pp. 233-237.

30. Bui, L., Shaw, H. J., and Zitelli, L. T., "Experimental Broadband Ultrasonic Transducers Using PVF_2 Piezoelectric Film," Electronics Letters 12 (5 August 1976), pp. 393-394.

31. Bracewell, R., The Fourier Transform and Its Applications, McGraw-Hill, San Francisco, 1965, pp. 179-181.

32. Bui, L., Shaw, H. J., and Zitelli, L. T., "Study of Acoustic Wave Resonance," submitted to IEEE Trans. on Sonics and Ultrasonics.

33. Papadakis, E. P., "Nonuniform Pressure Device for Bonding Thin Slabs to Substrates," J. of Adhesion, 3 (1971).

34. Onoe, M., and Tiersten, M. F., "Resonant Frequencies of Finite Piezoelectric Ceramic Vibrators with High Electromechanical Coupling," IEEE Trans. on Ultrasonics Engineering, 10 (1963), pp. 32-39.

35. Auld, B. A., Acoustic Fields and Waves in Solids, Vol. 1, John Wiley and Sons, New York, 1973.

36. Kino, G. S., Lecture notes, 1973.

37. Jaffe, H., and Berlincourt, D. A., "Piezoelectric Transducer Materials," Proc. IEEE 53 (1965), pp. 1372-1386.

38. Giebe, E., and Blechschmidt, E., "Experimental and Theoretische Untersuchungen über Dehnungs — Schwingungen von Stäben and Röhren, (I) and (II), Ann. Phys., Vol. 18, pp. 417-456 (I) and 457-485 (II), October and November 1933.

39. Harrington, R. F., Time-Harmonic Electromagnetic Fields, McGraw-Hill, New York, 1961, pp. 180-186.

40. Miller, G. F. and Pursey, H., "The Field and Radiation Impedance of Mechanical Radiators on the Free Surface of a Semi-Infinite Isotropic Solid," Proc. Royal Soc. of London, 223 (1954), pp. 521-541.

41. Auld, B. A., Acoustic Fields and Waves in Solids, Vol. 2, John Wiley and Sons, New York, 1973, pp. 177-190.

42. DeSilets, C. S., Fraser, J., and Kino, G. S., "Transducer Arrays Suitable for Acoustic Imaging," 1975 IEEE Ultrasonics Symposium Proceedings.

43. Patents No. 3,403,271 and 3,487,137.

44. Lees, S., Gilmore, R. S., and Kranz, P. R., "Acoustic Properties of Tungsten Vinyl Composites," IEEE Trans. on Sonics and Ultrasonics, SU-20 (January 1973), pp. 1-2.

45. Zitelli, L. T., private communication.

46. Dow Liquid Epoxy Resins, The Dow Chemical Company, Midland, Michigan, 1969.

47. Kino, G. S., DeSilets, C., Fraser, J., and Waugh, T. M., "New Acoustic Imaging Systems for Nondestructive Testing," IEEE Ultrasonics Symp. Proc., 1975, pp. 94-101.

48. Leung, W., Shaw, H. J., Kino, G. S., Winslow, D. K., and Zitelli, L. T., "Acoustic Phase Contrast Imaging with Electronic Scanning," IEEE Ultrasonics Symp. Proc., 1976, p. 151.

49. Leung, W. P., Shaw, H. J., Kino, G. S., and Zitelli, L. T., "A New Technique for High Speed Stress Detection and Imaging Using a 100-Element Acoustic Phased Array," IEEE Ultrasonics Symp. Proc., 1977, pp. 255-258.

50. Fukumoto, A., Hawabuchi, M., Hayami, H., "Portable Ultrasonic Diagnostic System Using Scanned Linear Array Transducers," Proc. AAMI Twelfth Annual Meeting, 1977, p. 390.

51. Defranould, Ph., and Souquet, J., "Design of a Two Dimensional Array for B and C Ultrasonic Imaging System," IEEE Ultrasonics Symp. Proc., 1977, pp. 259-263.

52. Auld, B. A., Acoustic Fields and Waves in Solids, Vol. 2, John Wiley and Sons, New York, 1973, pp. 76-88.

53. Roberts, C. G., "Optically Scanned Acoustic Imaging," Microwave Laboratory Report No. 2361, Stanford University, October 1974.

54. Auld, B. A., Vol. 2, op. cit., pp. 66-69.

55. Viktorov, I. A., Rayleigh and Lamb Waves, Plenum Press, New York, 1967, Chapter I.

56. Shaw, H. J., Weinstein, D., and Drake, M., to be published.

57. Mason, Warren, P., "Properties of Polymers and Nonlinear Acoustics," in Physical Acoustics, Vol. II, Part B, Academic Press, New York, 1965, Chapters 8-9.